Doctoral Dissertation (Censored)

博士論文 (要約)

Development of Tin-Based Transparent Conductive Oxides with High Carrier Mobility

（高キャリア移動度スズ系透明導電性酸化物の開発）

A Dissertation Submitted for the Degree of Doctor of Philosophy

December 2020

令和 2 年 12 月博士（理学）申請

Department of Chemistry, Graduate School of Science

The University of Tokyo

東京大学大学院理学系研究科

化学専攻

Michitaka Fukumoto

福本　通孝

Abstract

Transparent conductive oxides (TCOs), exhibiting excellent transparency and conductivity simultaneously, are of increasing importance for optoelectronic applications such as electrodes in solar cells and flat-panel displays. Generally, conductivity increases as carrier Hall mobility (μ_H) and carrier density (n_e) increase, whereas too high n_e results in the loss of transparency due to plasma absorption. Thus, a key to practical TCOs is to achieve high Hall mobility in degenerately-doped regime ($n_e \sim 10^{20}$ cm^{-3}), which can increase electrical conductivity without sacrificing optical transparency. A main strategy to attain high μ_H is to design a carrier conduction pathway consisting of spatially-extended *s*-orbital of cation, such as Sn^{4+}, In^{3+}, and Zn^{2+} for electron-transporting (*n*-type) TCO and Sn^{2+}, Pb^{2+}, and Bi^{3+} for hole-transporting (*p*-type) TCO. Sn-based TCOs are a unique class of materials exhibiting both high electron mobility and high hole mobility, depending on the valence of Sn. In this study, I aimed to develop Sn-based TCOs with high-μ_H.

I first investigated the electron transport properties of doped SnO_2. Although doped SnO_2 is one of the practically important TCOs, the highest μ_H value reported for

SnO_2 films is significantly lower than those in bulk single crystals. Therefore, it is highly desirable to determine the upper limit of experimentally accessible μ_H in SnO_2 films and develop guiding principles to achieve such high μ_H. From this point of view, I investigated electron transport properties of Ta-doped SnO_2 (TTO) epitaxial films, focusing on the growth orientation and n_e dependence of μ_H. As a result, I found that (001)-oriented growth is essentially favorable for achieving high-μ_H because of the suppressed propagation of {101} CSPs. The (001)-oriented TTO films exhibited maximum μ_H of 130 $cm^2V^{-1}s^{-1}$ at $n_e \sim 1\times10^{20}$ cm^{-3}, which almost reached the intrinsic limit of μ_H determined by phonon and ionized impurity scatterings. Subsequently, the transport properties for (001)-oriented W-doped SnO_2 (WTO) epitaxial films were investigated. Although the WTO films have been known to be a high-μ_H TCO, the detailed carrier generation mechanism remains to be known. I eventually found that the doped W in WTO films behaved as a single donor by fabricating the films with excellent μ_H comparable to those of TTO films. X-ray fluorescent holography revealed substitution of W atoms for Sn atoms.

Then I explored another dopant for SnO_2, P, which has recently been suggested as a promising dopant for SnO_2 by first-principles calculation. The synthesized P-doped

SnO_2 (PTO) films exhibited high-μ_H and high carrier activation rate, agreeing well with the theoretical calculation.

Next, I tried to develop practical SnO_2 films toward an application to solar cells. I proposed a technique to fabricate textured surfaces on transparent conductive SnO_2 films by processing substrates with a bottom-up technique. I used self-assembled nanospheres of SnO_2 as nanostructured templates. This template approach is potentially more productive and scalable than alternative methods because the template can be fabricated in the same sputtering chamber used to deposit TCO layers.

I also examined the potential of $Sn_5O_2(PO_4)_2$ as a *p*-type TCO. A recent theoretical calculation predicted that $Sn_5O_2(PO_4)_2$ can be a host material for *p*-type TCO with high μ_H. I successfully fabricated phase-pure $Sn_5O_2(PO_4)_2$ thin films with (001)-orientation by using Y_2O_3 buffered glass. The obtained $Sn_5O_2(PO_4)_2$ film showed high transparency in the visible and near-infrared spectral regions with a large bandgap of 3.87 eV. In addition, the film was an intrinsic semiconductor without intentional doping, which is suitable for studying the fundamental physics of the material.

Abbreviations and Symbols

BHD	Brooks-Herring-Dingle
CBM	conduction band minimum
CSP	crystallographic shear plane
CVD	chemical vapor deposition
DC	direct current
DOS	density of states
EDS, EDX	energy dispersive X-ray spectroscopy
FTO	F-doped SnO_2
FWHM	full-width at half-maximum
ITO	Sn-doped In_2O_3
IMO	Mo-doped In_2O_3
MBE	molecular beam epitaxy
NIR	near infrared
PDOS	partial density of states
PLD	pulsed laser deposition
PTO	P-doped SnO_2
PVD	physical vapor deposition
PVs	photovoltaics
RF	radio frequency
RSM	reciprocal space mapping
SEM	scanning electron microscope
SNS	self-assembled nanospheres
TEM	transmission electron microscope
TCO	transparent conductive oxide
TTO	Ta-doped SnO_2
UV-vis	ultraviolet-visible
VBM	valence band maximum
WTO	W-doped SnO_2
XAFS	X-ray absorption fine structure
XFH	X-ray fluorescence holography

XRD	X-ray diffraction
XPS	X-ray photoemission spectroscopy
YSZ	Y-stabilized ZrO_2
α	absorption coefficient
ε_r	the relative static dielectric constant
ε_0	the permittivity of vacuum
λ	laser wavelength
λ_p	plasma wavelength
μ_H	Hall mobility
μ_{disl}	μ_H considering limited by dislocation scattering
μ_{iis}	Hall mobility limited by ionized impurity scattering
μ_{lat}	Hall mobility limited by phonon scattering
ρ	electrical resistivity
σ	electrical conductivity
τ	average carrier scattering time
ω_p	plasma frequency
d	distance between each lattice plane, d-spacing
e	elementary charge
$\mathbf{E}$	electric field
E	energy
E_F	Fermi energy
$\mathbf{H}$	magnetic field
m^*	carrier effective mass
m_h	hole effective mass
n_e	carrier density
P_{O_2}	oxygen partial pressure
t	film thickness
T	transmittance
T_{dif}	total transmittance
T_{tot}	diffuse transmittance
T_s	substrate temperature

Contents

Chapter 1

General introduction

Transparent conductive oxide (TCO) is a class of materials which uniquely possess both high transparency and low electrical resistivity. The discovery of the first transparent conductive oxide dates back to the early 1900s, when Karl Bädeker (Universität Leipzig, Germany) fabricated CdO thin films by annealing sputtered Cd metal in the air [1]. Subsequent efforts have been devoted to exploring and improving TCOs because of their usefulness in optoelectronic device applications. A hundred years on, TCOs have still been essential for many applications such as multi-functional windows, flat-panel displays, solar cells, and flexible electronics. Nowadays, the need for sustainable energy resources and adequate information infrastructure in our world has spurred an unprecedented effort to develop high-performance thin films of TCOs. Moreover, contemplating the current global situation suffering from resource depletion and mass consumption, the parent materials for TCOs need to be composed of environment-friendly elements. Stimulated by such a situation, I aimed to develop high-performance thin films of TCOs based on Sn, which is a non-toxic, earth-abundant element. In particular, the critical requirement is to develop thin films with high carrier mobility to enhance electrical conductivity without sacrificing optical transparency. In this study, I successfully fabricated thin films of impurity-doped Sn-based TCOs with extremely high electron mobility and undoped Sn-based TCO with promising high hole

mobility.

1.1 Transparent conductive oxides

TCOs, exhibiting excellent optical transparency and electrical conductivity, are counterintuitive [2,3]. In general, transparent materials such as plastics or glass are insulative, while conductive materials, exemplified by metals, commonly reflect visible light. The coexistence of these two incompatible properties in TCOs, as typified by SnO_2, ZnO, and In_2O_3, can be rationalized as follows. Figure 1.1 shows the band dispersion of SnO_2 calculated by an augmented plane wave method [4]. As seen in this figure, transparent materials generally exhibit a bandgap over 3 eV, which is higher than the energy for visible light (1.5 eV−3 eV), inhibiting interband transition of carriers by light across the bandgap. In other words, carriers cannot be introduced intrinsically inside the transparent materials, which results in the highly resistive behavior of the materials. The

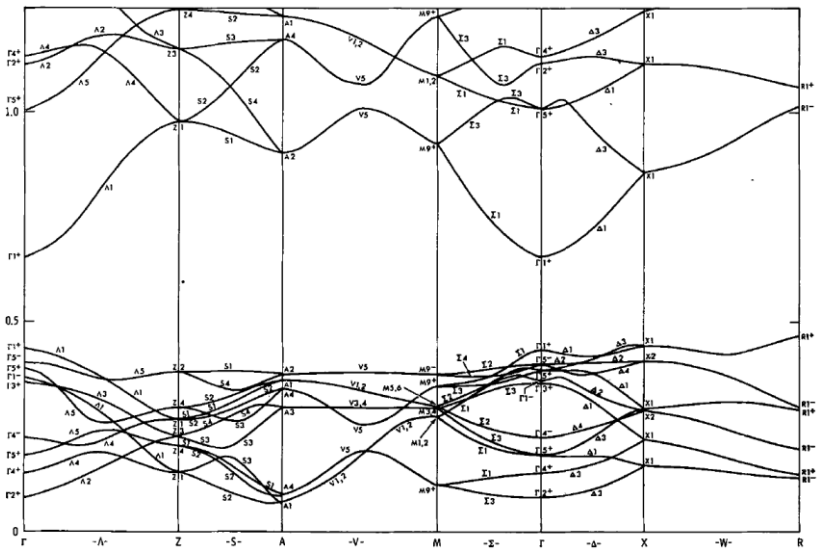

Fig. 1.1. Band structure of SnO_2. Reprinted from Ref [4] with permission from Elsevier, Copyright 1974. Unit for left axis is Ry (1 Ry = 13.606 eV).

resistivity, ρ, is formulated as

$$\rho = \frac{1}{\sigma} = \frac{1}{n_e \mu_H e} \tag{1-1}$$

where σ is the conductivity, n_e is the charge carrier density, μ_H is the carrier mobility, and e is the elementary charge given by 1.602×10^{-19} C. As seen from eq. (1-1), low ρ is achieved by increasing n_e or μ_H. In practical TCOs, low ρ is obtained by increasing n_e, which is controlled by substitutional impurity doping, e.g., Sn-doped In_2O_3 and Sb-doped SnO_2, as will be discussed in Section 1.2.1 (c). In these compounds, the impurity species generate carriers in the host material, leading to the improved ρ. It should be noted that nominally undoped TCOs can be conductive, possibly due to nonstoichiometry in the TCOs, i.e., the existence of interstitial cation or oxygen vacancies [5]. For example, the conductivity of SnO_2 films can be tuned by controlling the oxygen partial pressure during

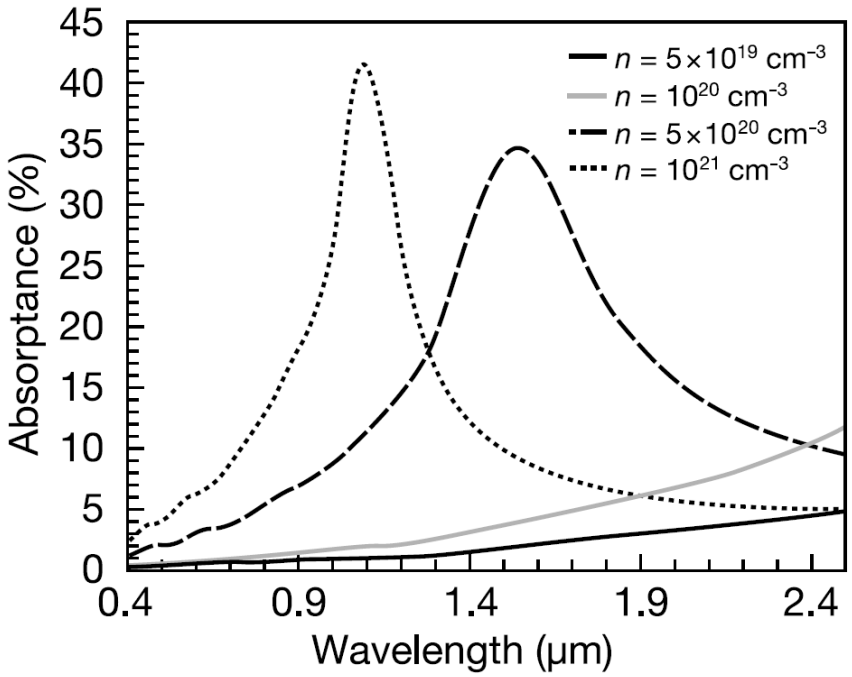

Fig. 1.2. Calculated free-carrier absorptance of the films with n_e ranging from 5×10^{19} cm^{-3} to 10^{21} cm^{-3} assuming μ_H of 100 cm^{2}V^{-1}s^{-1} and thickness of 0.5 μm [7]. Reprinted from Ref [7] with permission from Cambridge University Press, Copyright 2000.

thin film growth [5,6]. The carrier generation mechanism in intrinsically doped TCOs is still unclear. Nevertheless, even in the extrinsically doped TCOs, it is important to distinguish the carriers introduced by impurities from those by native defects such as oxygen vacancies.

As mentioned above, low ρ is achieved in TCOs by impurity doping. However, too much n_e results in the loss of transparency by plasma absorption, as demonstrated in Figure 1.2. [7]. The maximum plasma absorption occurs at the plasma wavelength, λ_p, formulated as

$$\lambda_p = 2\pi c \left(\frac{m^* \varepsilon_0 \varepsilon_\infty}{n_e e^2} \right)^{\frac{1}{2}} \tag{1-2}$$

where c is the speed of light in vacuum, m^* is the carrier effective mass, ε_0 is the permittivity of free space, and ε_∞ is the high-frequency permittivity. As can be understood from this formula, λ_p shifts to low wavelength when n_e increases, which eventually results in the visible-light absorption.

1.2 High-performance transparent conductive oxides

A basic and critical requirement for TCOs is the optimization of the electrical conductivity and the optical transmittance. Although both parameters should be ideally as large as possible, their correlation inhibits the coexistence of maximum transmission and conduction. The incompatibility of these two properties can be summarized as

$$\sigma = n_e \mu_H e = \frac{n_e e^2 \tau}{m^*} \tag{1-3}$$

$$\omega_p = \frac{2\pi c}{\lambda_p} \propto \left(\frac{n_e}{m^*} \right)^{\frac{1}{2}} \tag{1-4}$$

where σ is the conductivity, n_e is the carrier density, m^* is the effective carrier mass, λ_p is the plasma wavelength, and ω_p is the plasma frequency. Here, the relation between μ_H and m^* is written as

$$\mu_H = \frac{e\tau}{m^*} \tag{1-5}$$

where τ is the average carrier scattering time. From eq. (1-3) and eq. (1-4), two criteria can be established toward high-performance TCOs as summarized in Fig. 1.3: The first one adopts low-m^* host materials (ex. In_2O_3, ZnO, and SnO_2) in lightly doped regime ($n_e \sim 10^{20}$ cm^{-3}). Lower m^* leads to higher μ_H and ω_p, which requires moderate n_e to keep high conductivity and transmittance simultaneously. Another one, which is a newly emerging concept, is increasing m^* of the materials in heavily doped regime ($n_e \sim 10^{22}$ cm^{-3}) [8–13]. Contrary to the case of host materials with low-m^*, ω_p of high-m^* materials shifts to lower range, allowing heavy carrier doping. The high m^* of this class of TCOs is achieved by electron correlations between each carrier (ex. $SrVO_3$, $CaVO_3$, and $SrNbO_3$) [9,10] or interaction between carrier and phonon (Cr-based oxides) [11–13]. In this study, I focus on high-μ_H TCOs.

1.2.1 Key factors to attain high mobility in transparent conductive oxides

Carrier conduction in materials involves various physical phenomena which

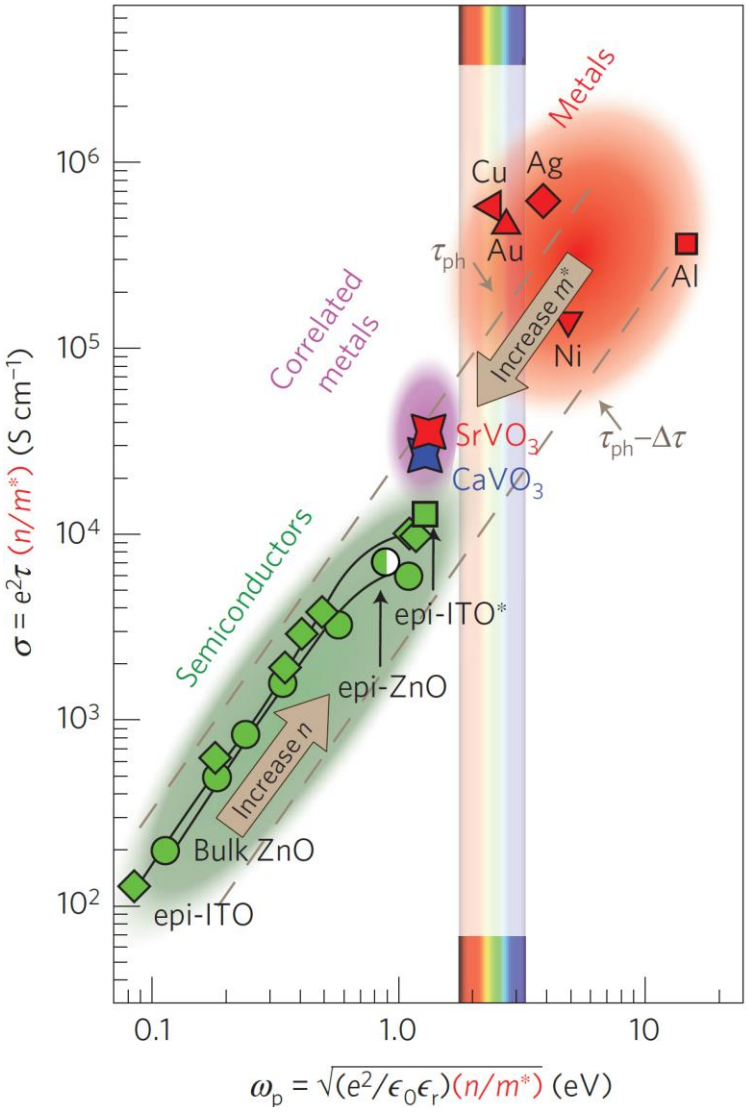

Fig. 1.3. Optimization of electrical conductivity under the constraint to keep free carrier reflection edge, represented by ω_p, below the visible spectrum. ITO denotes Sn-doped In_2O_3. Rainbow band represents the visible light range. Reprinted by permission from Macmillan Publishers Ltd: Nature Materials [9], Copyright 2015.

inevitably affect their electrical properties such as μ_H and n_e. Here I pick up some of them with considering m^* and τ, which are typical factors affecting μ_H as can clearly be seen in eq. (1-5).

(a) Carrier conduction pathway

For achieving fast carrier conduction in crystalline solid-state materials, it is essential to design an appropriate conduction pathway, which is determined by the crystal

structure and the constituent elements. Kawazoe *et al*. proposed the elemental and structural requirements for achieving high-μ_H, especially in *n*-type compounds, as follows [14]:

1) The constituent metal cations are preferably selected from *p*-block heavy cations with ns^0 electronic configuration, where *n* is the principal quantum number, such as Zn^{2+}, Cd^{2+}, Hg^{2+}, Ga^{3+}, In^{3+}, Tl^{3+}, Ge^{4+}, Sn^{4+}, Pb^{4+}, Sb^{5+}, Bi^{5+}, and Te^{6+}. In this case, the conduction band minimum (CBM) mainly comprises spatially-extended *ns* orbitals of metal cations.
2) Crystal structure should comprise linear chain of edge-sharing octahedra centered by metal cations, as is the case for rutile SnO_2 and bixbyite In_2O_3, rather than corner-sharing octahedra. In edge-sharing structures, the two neighboring metal cations are not interfered with by oxygen atoms, resulting in shortened distance between them.

The combination of spatially-extended *s*-orbitals and edge-sharing structure enhances direct overlap of vacant *s* orbitals between the neighboring cations. The large overlap between cations results in high-μ_H, rationalized as below [15]. Considering a 1D crystal with a lattice constant of *a*, the energy band of the crystal is formed by periodically aligned atomic orbitals. The periodicity of the wave function can be expressed as the following equation on the assumption of periodic boundary condition:

$$\psi(x+Na)=\psi(x) \tag{1-6}$$

where *N* is the number of the atoms in one period. The distance between each atom along the 1D chain is equal to *a*, which means that the electron density should be invariant even after the chain is moved by *a*. Electron density is described by the product of a wave function and its complex conjugate:

$$\rho(x)=\psi^*(x)\psi(x). \tag{1-7}$$

The periodicity of the electron density can be expressed as

$$\rho(x+a)=\rho(x). \tag{1-8}$$

Eq. (1-8) holds only when the following conditions are satisfied:

$$\psi(x)=\kappa\psi(x+a) \tag{1-9}$$

$$\kappa^N=1. \tag{1-10}$$

Here κ is a complex number satisfying

$$\kappa^*\kappa=1. \tag{1-11}$$

Thus, κ must be an imaginary number that is the Nth root of 1. κ can be written as

$$\kappa=\exp\left(\frac{i2\pi p}{N}\right)=\exp(ika) \tag{1-12}$$

where i is $\sqrt{-1}$, p is an integer regarded as a quantum number, k is a number which is defined as

$$k=\frac{2\pi p}{Na}. \tag{1-13}$$

Using k instead of p, one can write an equation that does not depend on N. In a real crystal, N is so large that k can be regarded as a continuous number. Eq. (1-9) can be rewritten as

$$\psi(x+a)=\exp(ika)\psi(x). \tag{1-14}$$

The wave function satisfying eq. (1-14) can be expressed as

$$\psi(x)=\exp(ika)u(x) \tag{1-15}$$

$$u(x+a)=u(x) \tag{1-16}$$

where $u(x)$ can be selected from any periodic function. The function written by eq. (1-15) is known as the Bloch function.

A band structure formed by the overlap of each atomic orbital can be calculated by a linear combination of atomic orbitals (LCAO) approximation. By applying LCAO

approximation, crystalline orbital can be described by a linear combination of each atomic orbital:

$$\psi(x)=\sum_n c_n \chi_n(x) \tag{1-17}$$

$$c_n=\exp(ikan) \tag{1-18}$$

where $\chi_n(x)$ is the wave function corresponding to nth atomic orbital. The coefficient cn also possesses periodicity. When an integer p and a wavenumber k are substituted by $p+N$ and k', the orbital coefficient c_n' is derived as

$$\begin{aligned} c_n' &= \exp\left\{ i\left(k+\frac{2\pi}{a} \right) na \right\} \\ &= \exp(ikan)\exp(2\pi in) \\ &= c_n . \end{aligned} \tag{1-19}$$

Thus, k and k' give coefficients belonging to the same crystalline orbital. Any integer value is allowed for p. However, only N of them can create different crystalline orbitals. k ranges from $-\pi/a$ to π/a, and the k value out of this range is just a repetition of existed k value. The energy of the crystalline orbital can be evaluated by the following equation:

$$E_k=\frac{\int \psi_k^* H \psi_k}{\int \psi_k^* \psi_k} \tag{1-20}$$

where H is a Hamiltonian possessing the periodicity of the lattice. The numerator and the denominator are expressed as the following equations:

$$\int \psi_k^* H \psi_k = \sum_{m=1}^{N}\left[\sum_{m=1}^{N} \exp\{ika(n-m)\} \int \chi_m^* H \chi_n \right] \tag{1-21}$$

$$\int \psi_k^* \psi_k = \sum_{m=1}^{N}\left[\sum_{m=1}^{N} \exp\{ika(n-m)\} \int \chi_m^* \chi_n \right]. \tag{1-22}$$

The LCAO approximation assumes two conditions:

$$\int \chi_m^* \chi_n = \begin{cases} 1(n=m) \\ 0(n \neq m) \end{cases}. \tag{1-23}$$

The first one is the normalization condition. The second one claims that the orbital overlap between different centers can be ignored. *N* terms, which are equal to 1, are involved in eq. (1-22). Thus, eq. (1-23) simplifies to

$$\int \psi_k^* \psi_k = N. \tag{1-24}$$

Among the elements of the Hamiltonian matrix in eq. (1-21), the elements with $n=m$ simply give the energy for an electron in one atomic orbital, which can be defined as α. The elements with $n \neq m$ provide the energy of the interaction between different atomic orbitals. It is reasonable to ignore the interactions between atomic orbitals other than those adjacent to each other in the chain. The interaction between neighboring atoms can be defined as β. Consequently, the following equations are derived:

$$\int \chi_n^* H \chi_n = \alpha \tag{1-25}$$

$$\int \chi_m^* H \chi_n = \beta \quad \text{for adjacent } n \text{ and } m. \tag{1-26}$$

Thus, eq. (1-21) contains *N* terms with a contribution for the case of $n=m$ and the case that the two atoms are adjacent to each other:

$$\begin{aligned} \int \psi_k^* H \psi_k &= N\left[\alpha + \beta\left\{\exp(-ika) + \exp(ika)\right\}\right] \\ &= N\left\{\alpha + 2\beta\cos(ka)\right\}. \end{aligned} \tag{1-27}$$

From equations (1-20), (1-24), and (1-27), the following equation is derived:

$$E_k = \alpha + 2\beta\cos(ka). \tag{1-28}$$

In eq. (1-28), the *k* value is sufficiently close to zero. Therefore, E_k can be approximated as:

$$E_k = \alpha + 2\beta\left(1 - \frac{(ka)^2}{2}\right) = \alpha + 2\beta - \beta(ka)^2. \tag{1-29}$$

In a solid-state material, the mass of an electron is different from that of a free electron, which is generally referred to as the effective mass. The carrier effective mass is defined as

$$\frac{1}{m^*} = \left(\frac{1}{\hbar}\right)^2 \frac{\partial^2 E}{\partial k^2}. \tag{1-30}$$

Equations (1-5), (1-29), and (1-30) lead to the following relation:

$$\mu_{\mathrm{H}} = \frac{e\tau}{m^*} = e\tau\left(\frac{1}{\hbar}\right)^2 \frac{\partial^2 E}{\partial k^2} = -2e\tau a^2\beta \propto \beta. \tag{1-31}$$

The β value increases when the atomic orbital overlap becomes large, as seen in eq. (1-26). Thus, the considerable overlap of the atomic orbital leads to high μ_{H}. It should be noted that an exceptionally high-μ_{H} TCO based on *d*-orbital can also be realized, as confirmed in anatase TiO_2 [16].

In this study, I focused on Sn-based TCOs, in which the vacant *s*-orbital (*n*-type, Sn^{4+}-based) or occupied *s*-orbital (*p*-type, Sn^{2+}-based) is available for the conduction path, as explained in the following section.

(b) Carrier scattering

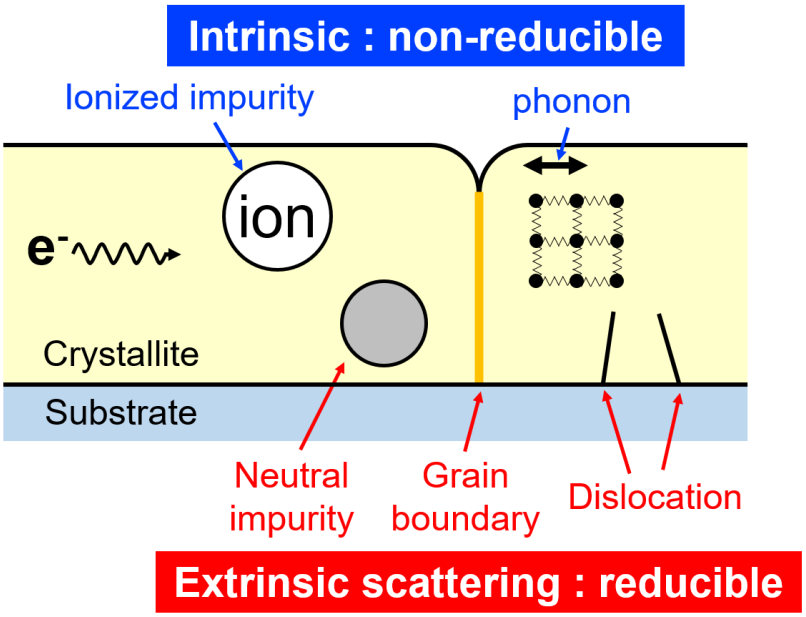

Fig. 1.4. A schematic illustration depicting the typical carrier scattering mechanisms in *n*-type TCOs.

When carriers traverse real crystals, the carriers are scattered by many kinds of defects unlike in perfect crystals, resulting in the decrease in τ and thereby reduced μ_H. Typical carrier scattering mechanisms can be roughly classified into two classes: intrinsic scatterings caused by ionized impurities and phonon, and extrinsic scatterings caused by neutral impurities, grain boundaries, and dislocations. The intrinsic scatterings impose an upper limitation of μ_H because they are non-reducible. On the contrary, the effect of the extrinsic scattering can be reduced by optimizing the film fabrication process.

Ionized impurity scattering is the intrinsic scattering caused by the Coulomb interaction between charge carriers and the ionized impurities in the lattice. Regarding temperature-dependence of μ_H, the ionized impurity scattering is pronounced at low temperatures, where the effect of phonon scattering is negligible. Concerning the n_e dependence of μ_H, electrical conduction tends to be dominated by the ionized impurity

scattering as n_e increases because of the increase in the number of ionized impurity atoms. The scattering of charge carriers by ionized impurities is ordinarily described by the Conwell-Weisskopf (CW) model or Brooks-Herring-Dingle (BHD) model [17,18]. In Conwell-Weisskopf model, the Coulomb potential is

$$V(r)=\frac{Ze}{4\pi\varepsilon_r\varepsilon_0 r} \tag{1-32}$$

where Z is the charge of the ionized impurity, e is the elementary charge, ε_r is the relative static dielectric constant, and ε_0 is the permittivity of free space. On the other hand, the BHD model employs the "screened" Coulomb potential:

$$V(r)=\frac{Ze}{4\pi\varepsilon_r\varepsilon_0 r}\exp\left(-\frac{r}{a}\right) \tag{1-33}$$

where a is the screening length or screening radius. Screening means that the free carriers cause the scattering potential of ionized impurities to decrease with distance rapidly. The BHD formula is calculated to be

$$\mu_{iis}=\frac{24\pi^3\left(\varepsilon_r\varepsilon_0\right)^2\hbar^3 n_e}{e^3 m^{*2} F_{ii} Z^2 n_I} \tag{1-34}$$

where μ_{iis} is the Hall mobility limited by ionized impurity scattering, $\hbar$ is the reduced Planck's constant, m^* is the effective electron mass, and n_I is the density of the ionized impurity. The screening function F_{ii} is given by

$$F_{ii}=\ln\left(1+\frac{4}{\xi}\right)-\frac{1}{\left(1+\frac{x}{\xi}\right)} \tag{1-35}$$

with

$$\xi = \frac{e^2 m^*}{\pi \varepsilon_r \varepsilon_0 \hbar^2 \left(3\pi^5\right)^{1/3} n_e^{1/3}} . \tag{1-36}$$

The μ_H values calculated by CW and BHD models are written in the same form except for the different logarithmic factors (F_{ii} for the BHD model) [17,18]. Thus, F_{ii} is responsible for expressing the screening effect. BHD model expresses the μ_H behavior at high n_e region rather well by taking into account screening by free carriers. For TCOs, which are degenerately-doped widegap semiconductors in general, the BHD model is frequently used for estimating the contribution of ionized impurity scattering (see Chapter 3 and 4).

In a solid or liquid material, each atom oscillates at a certain frequency. Quantum mechanics treats such vibration modes in condensed matters as a quasiparticle, which is called a phonon. Carrier scattering due to the phonons is called phonon scattering. The contribution of phonon scattering increases at high temperatures because the degree of vibration of each atom increases as the temperature increases. There are two types of phonons: acoustic phonons, whose frequency is almost proportional to the momentum or wavenumber of the atoms, and optical phonons, whose frequency does not depend much on the wavenumber of the atoms and whose energy is high. Therefore, there are two types of scattering mechanisms: acoustic phonon scattering and optical phonon scattering. Each phonon scattering mechanism can also be categorized into two: one is the scattering by

Table 1.1. Classification of phonon.

	deformation	Polarization
Optical	non-polar	polar
Acoustic	deformation potential	piezoelectric

the crystal lattice, which is mechanically distorted by vibration, and the other is the scattering by the electric dipole, which is caused by the ionic bonding between atoms. The name of each phonon scattering is listed in Table 1.1. As for parent materials for typical TCOs, polar optical phonon scattering is dominant, formulated as follows [19]:

$$\mu_{\mathrm{lat}}(T)=\frac{C_{\mathrm{ph}}\left(4\pi\varepsilon\varepsilon_0 E_{\mathrm{F}}\right)2kT}{n_{\mathrm{e}}e^3h^3\omega_0}\sinh^2\left(\frac{\hbar\omega_0}{2kT}\right) \tag{1-37}$$

where μ_{lat} is the Hall mobility limited by the phonon scattering, C_{ph} is an enhancement factor, and E_{F} is the Fermi energy.

Neutral impurity scattering is the extrinsic scattering of conduction carriers by neutral impurity centers such as inactive dopant atoms. Erginsoy estimated the scattering of carriers by assuming hydrogen-like neutral impurities as scattering centers [20]. The mobility is given by

$$\mu_{\mathrm{N}}=\frac{m^*e^3}{A(T)\varepsilon\varepsilon_0\hbar^3 n_{\mathrm{N}}} \tag{1-38}$$

where $A(T)$ is the temperature-dependent scattering cross-section factor, and n_{N} is the neutral impurity density. Due to the difficulty in evaluating the accurate value of n_{N} and $A(T)$ in a thin film, it is hard to quantify the contribution of neutral impurities.

Dislocation is a one-dimensional crystallographic defect which is almost invariably present in a real crystal. The dislocations cause atomic rearrangement inside the crystal. The displacement distance of the atoms is defined by a Burgers vector. In a thin film of an electrical conductor, three types of dislocations exist; edge dislocations, screw dislocations, and mixed dislocations. The Burgers vector is perpendicular (parallel) to the dislocation line in the case of edge (screw) dislocation. The edge dislocations vertical to the interface thread to the surface of the film (threading dislocations). The

reduction of μ_H by dislocations is evident particularly in the nondegenerate n_e region, as revealed in Ge and GaN [21,22]. Among various lattice defects inside a film, the threading dislocations have a pronounced effect on μ_H [22,23]. The dislocations are regarded as the negatively or positively charged lines acting as Coulomb scattering centers [22–25]. The contribution of dislocation scatterings to μ_H is calculated assuming the cylindrically symmetric potential around the dislocation lines. Pödör has analytically solved the Poisson equation for a plastically-deformed Ge in nondegenerately-doped region [21], and derived the μ_H considering dislocations (μ_{disl}) as follows:

$$\mu_{disl,\,non\,deg} = \frac{30\sqrt{2\pi}\left(\varepsilon_r\varepsilon_0\right)^2 a^2 \left(kT\right)^{\frac{3}{2}}}{N_{disl} e^3 {f_O}^2 \lambda_D \sqrt{m}} \tag{1-39}$$

where a is the distance between acceptor centers along the linear dislocation, f_O is the occupation rate of these acceptor sites, and λ_D is the Debye screening length as follows:

$$\lambda_D = \sqrt{\frac{\varepsilon_r\varepsilon_0 kT}{e^2 n_e}} \ . \tag{1-40}$$

From eq. (1-39) and eq. (1-40), the following relation is derived:

$$\mu_{disl,\,nondeg} \propto T\sqrt{n_e} \tag{1-41}$$

On the other hand, in degenerately-doped region, the μ_{disl} [26] is written as

$$\mu_{disl,\,deg} = \frac{4\times 3^{2/3} e c^2 n_e^{2/3}}{\pi^{8/3}\hbar N_{disl}} \left(1 + y\left(n_e\right)\right)^{3/2} \tag{1-42}$$

with

$$y\left(n\right) = \frac{2\times 3^{1/3}\pi^{8/3}\hbar^2 \varepsilon\varepsilon_0 n_e^{1/3}}{e^2 m^*} \ . \tag{1-43}$$

It is generally difficult to distinguish the contribution by dislocation scatterings to μ_H from

the other scattering factors in degenerately-doped regime, mostly due to a large contribution from ionized impurity scattering.

Grain-boundary is a region which separates two grains of the same phase, as schematically shown in Fig. 1.4. Seto successfully developed the model for grain boundary scattering for polycrystalline Si films [27]. In this model, the transport properties of polysilicon films are assumed to be governed by the carrier traps formed at

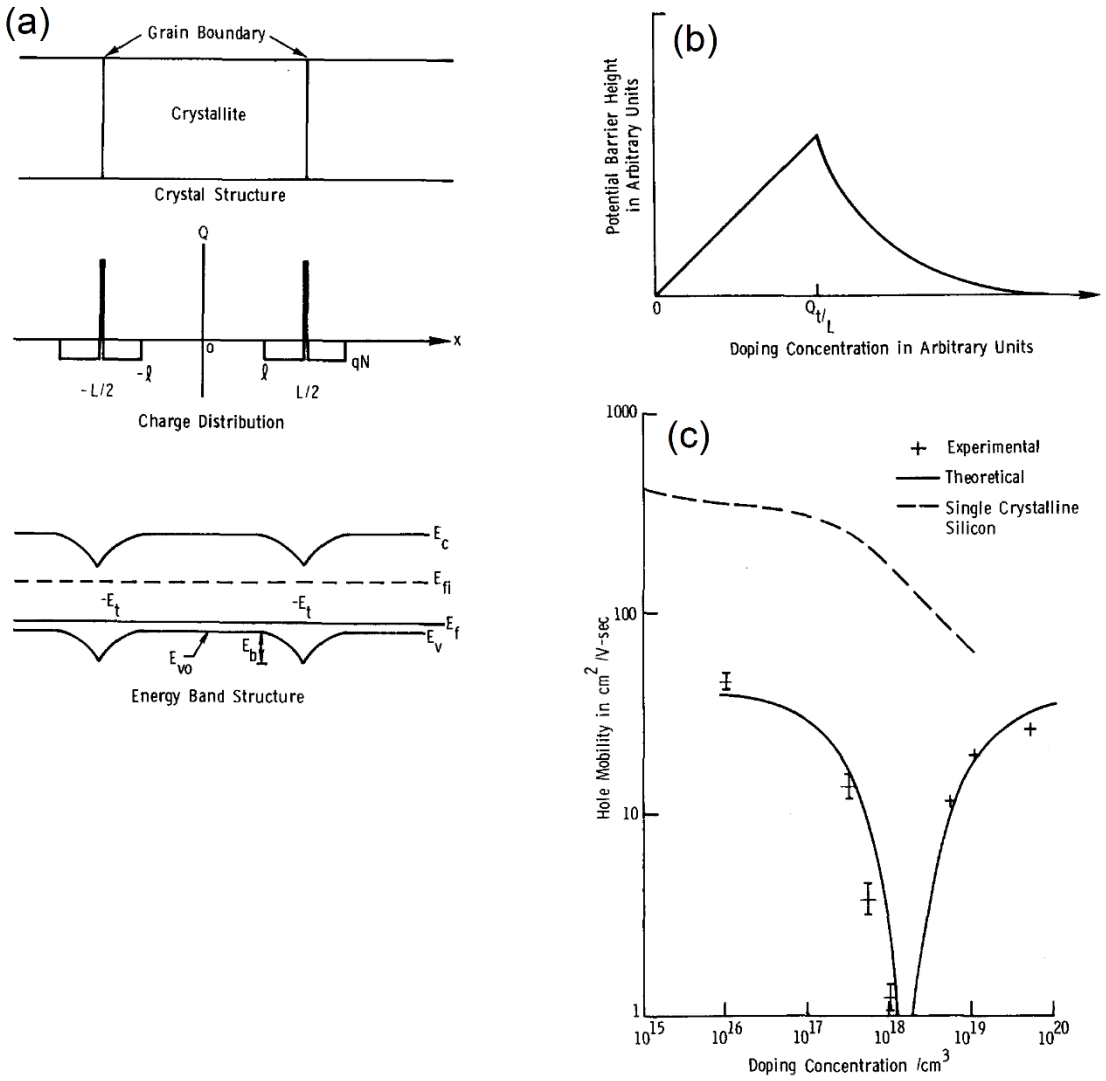

Fig. 1.5. (a) A modelled crystal grain structure of polysilicon films, the charge distribution inside the grains and grain boundary, and the energy band structure for polysilicon crystallites. (b) Doping concentration dependence of the potential barrier height. (c) Hole mobility as a function of doping concentration. Reprinted by permission with AIP Publishing LLC [27], Copyright (1975).

the grain boundaries. As the carrier density increases, carrier traps are gradually filled and produce a depletion layer at the grain boundaries, acting as double Schottky barriers (Fig. 1.5 (a)). The potential barrier height at the boundaries increases until all the traps are filled, and then the barrier height decreases due to the screening by the carriers (Fig. 1.5 (b)). Figure 1.5 (c) shows the hole mobility values for polysilicon films as a function of doping concentration. The modeled μ_H considering grain boundary scattering agreed well with the μ_H values for the obtained films.

The effect of grain boundaries and dislocations on μ_H is relatively small in epitaxial films than in polycrystalline films. In epitaxial films, the crystallinity is likely to depend on a lattice matching between film and substrate. Here, the lattice mismatch is defined as

$$f = \frac{a_{\text{film}} - a_{\text{substrate}}}{a_{\text{substrate}}} \tag{1-44}$$

where a_{film} and $a_{\text{substrate}}$ denote the in-plane lattice constants of the film and substrate in the same direction. If the f value is close to zero, the applied pressure inside the epitaxial films is so small that the films with high-crystallinity can be obtained, as demonstrated in ZnO/$ScAlMgO_4$ (SCAM) and In_2O_3/Y-stabilized ZrO_2 (YSZ) systems. Figures 1.6 (a) and (b) show μ_H as a function of n_e for epitaxial films of ZnO(0001)/SCAM(0001) at 300 K [28] and In_2O_3(001)/YSZ(001) at 300 K and 500 K [29], respectively. Figure 1.6 (c) plots μ_H as a function of Nb content for thin films of anatase TiO_2(001)/$SrTiO_3$(100) at 300 K [30], together with μ_H calculated by assuming intrinsic scatterings (phonon scattering, ionized impurity scattering). In all the samples, the effect of ionized impurity scattering was pronounced at high n_e region, simply because the amount of ionized impurity increased. In ZnO and In_2O_3, the experimental μ_H values agreed surprisingly

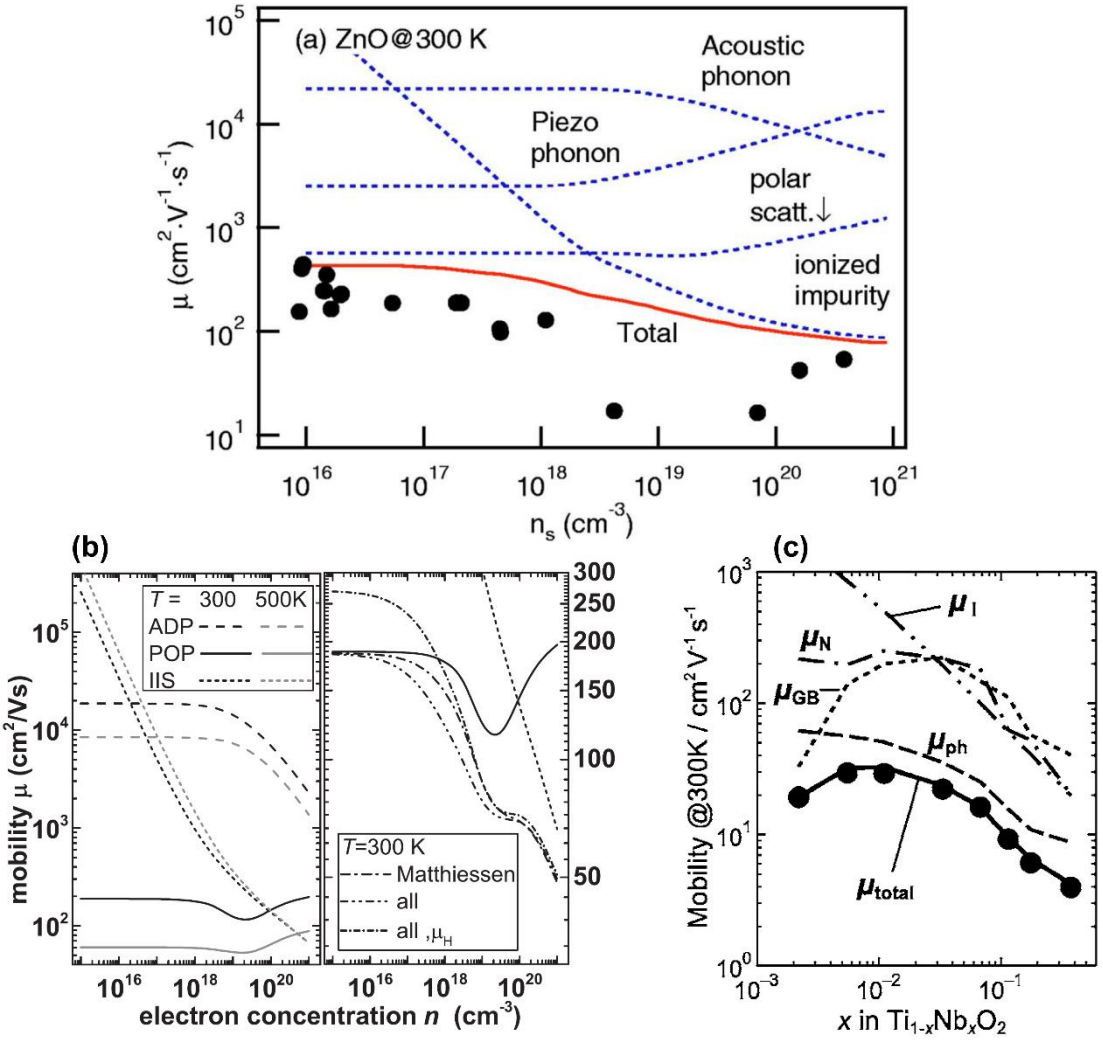

Fig. 1.6. The μ_H values as a function of n_e or dopant content for (a) ZnO at 300 K [28] (Copyright (2005) AIP publishing LLC), (b) In_2O_3 at 300 K and 500 K [29] (Copyright (2013) American Physical Society) and (c) TiO_2 [30] (Copyright (2007) AIP publishing LLC) epitaxial films, plotted together with the calculated μ_H values considering intrinsic scatterings (phonon and ionized impurity scattering).

well with the calculated ones assuming intrinsic scatterings, indicating that the quality of the films was so high that they are free from the effect of extrinsic scattering centers.

On the other hand, if small *f* cannot be realized due to the lack of suitable lattice-matched substrates, lattice relaxation would occur along with introducing grain boundaries and/or dislocations. In this case, intentional control of n_e is the key to achieving high μ_H because carriers play two competing roles in μ_H; an increase in n_e

enhances the screening of the Coulomb scattering potential and thus increases μ_H, whereas an increased amount of dopants suppresses μ_H owing to impurity scattering. It is helpful to review the carrier conduction in a polycrystalline film as an extreme case for understanding the carrier transport behavior in highly faulted epitaxial films. Figure 1.7 shows the transport properties for undoped and impurity-doped polycrystalline ZnO films [31]. The grain-boundary scattering is dominant at low n_e region ($n_e < 10^{20}$ cm^{-3}). As n_e increases, the grain-boundary scattering is gradually screened so that μ_H increases. Then μ_H decreased due to the dominant impurity-scattering at high n_e region ($n_e \geq 10^{20}$ cm^{-3}). The μ_H reaches the maximum when the contribution from grain boundaries and ionized impurities are comparable. Thus, controlling n_e is vital for achieving high μ_H in

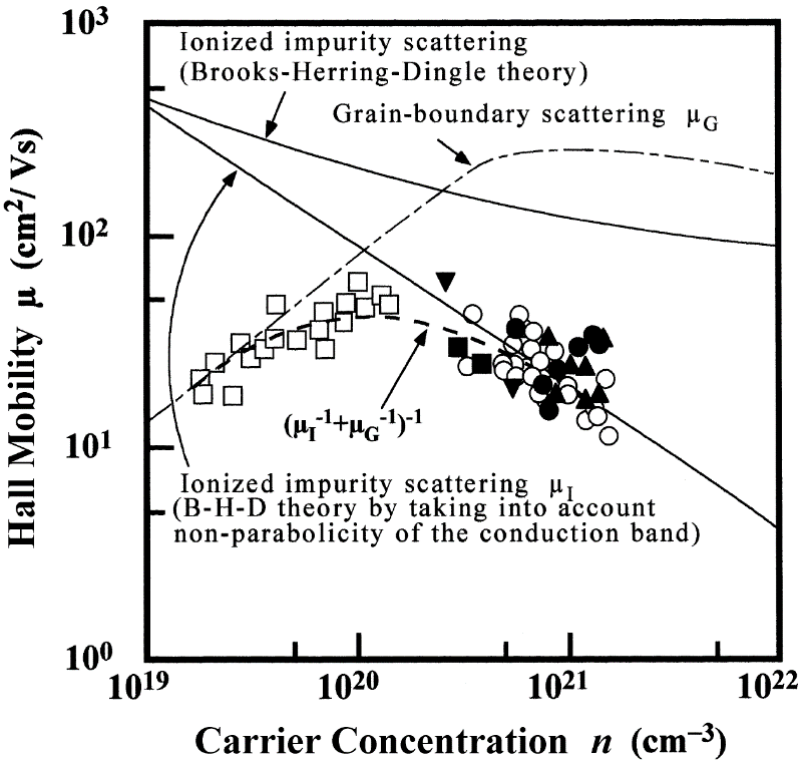

Fig. 1.7. μ_H versus ne of undoped ZnO films (□) and impurity-doped ZnO films: Al-doped (○,●), Ga-doped (▲), B-doped (■) and other (▼). The calculated μ_H values considering ionized impurities (μ_I) and grain boundaries (μ_G) are plotted together. Reprinted by permission from Cambridge University Press [31], Copyright (2000).

highly faulted epitaxial films.

(c) Dopant

Substitutional doping is of significant industrial importance not only for controlling n_e, but also for achieving high μ_H. Carriers are introduced to the materials by intentional substitution of cation or anion with a higher oxidation state (*n*-type) or lower oxidation state (*p*-type) than the replaced element. Traditionally, successful control of n_e by doping requires three conditions: (1) high solubility of the dopant element in the host material, (2) shallow dopant level, (3) lack of compensation of the carriers. As for point (1), conventional wisdom dictates that it is reasonably effective to select a dopant adjacent to the host element in the periodic table, taking Sn-doped In_2O_3 as a prime example. In this case, the dopant and host elements have similar ionic radii, achieving high solubility of the dopant without local lattice distortion.

The conventional doping strategy, i.e., selection of dopant adjacent to the host element, however, suffers from a large effective mass, i.e., low intrinsic μ_H due to a large hybridization of orbitals between the dopant and host elements, as seen in In_2O_3 doped with Sn [32–34]. Recent studies on Mo-doped In_2O_3 (IMO) proposed a new doping concept which facilitates effective carrier generation without diminishing carrier μ_H. Swallow *et al*. reported a comparative study of novel IMO and conventional ITO [33], demonstrating that the IMO thin films have higher μ_H than ITO. In ITO, the Sn 5*s* orbitals and the In 5*s* orbitals are mixed to form the CBM of In_2O_3. An increase of Sn concentration in In_2O_3 promotes further mixing of the orbitals at the CBM, resulting in the enhanced electron effective mass, i.e., low intrinsic μ_H. Contrary to the ITO, the Mo(IV) 4*d* orbitals in IMO, which works as donors, are energetically separated from the CBM and do not mix with the In 5*s* orbitals at the CBM. Figure 1.8 schematically shows

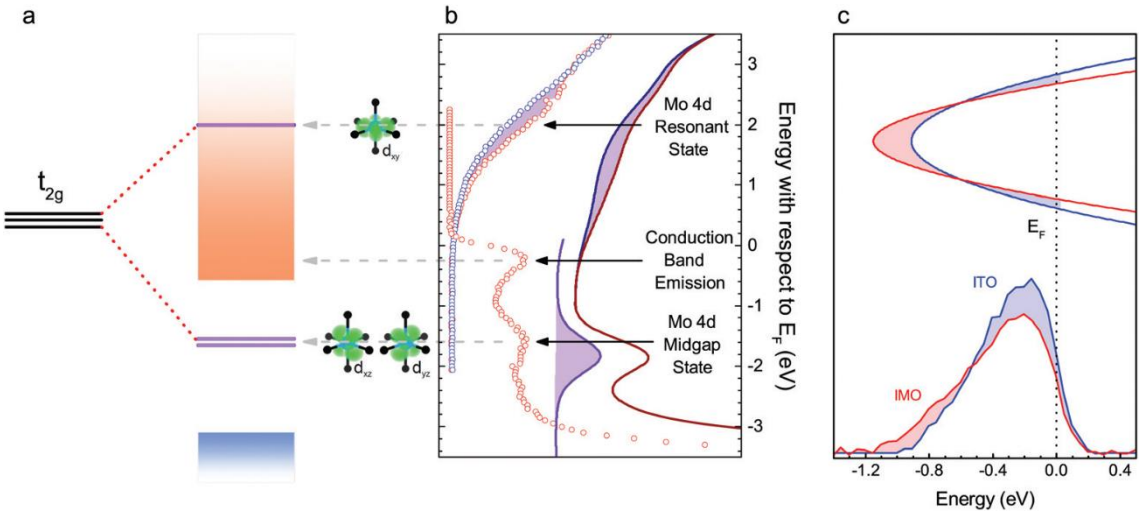

Fig. 1.8. (a) Schematic diagram for splitted Mo t_{2g} states in In_2O_3. (b) Inverse photoemission spectra taken from IMO (red) and ITO (blue). (c) Schematic band structure with vertical axis for wavevector and horizontal axis for energy. Below are HAXPES spectra displaying conduction band emission from IMO (red) and ITO (blue) [33]. Reprinted under a Creative Commons Attribution 3.0 Unported Licence.

the electronic band structures and experimentally observed photoemission spectrum of IMO. The Jahn-Teller-like distortion occurs at the Mo site, which causes the splitting of the three-fold degenerate t_{2g} state, upper d_{xy} state, and lower d_{xz} and d_{yz} states. The resultant *d* states are located well above and below the CBM of In_2O_3, preventing the Mo 4*d* state from hybridizing with In 5*s* state. Thus, a new doping criterion for high-μ_H can be established: transition metal dopants are favorable for carrier doping to *s*-orbital-based host materials since the donor *d* states hardly hybridize with the host cation *s*-states. The *d* orbitals of transition metals must possess energy levels that render the dopant atoms singly charged states. The donor *d*-state must be resonant in the conduction band, avoiding the hybridization at the CBM. This "resonant doping" allows the control of n_e without reducing μ_H in In_2O_3.

1.3 Tin-based transparent conductive oxides

Sn-based TCOs are a unique class of materials exhibiting high electron mobility and high hole mobility, depending on the valence of Sn as exemplified by *n*-type SnO_2 and *p*-type SnO. Here I review *n*-type and *p*-type TCOs based on Sn.

1.3.1 *n*-type tin-based transparent conductive oxides

An *n*-type counterpart in tin-based TCOs is typified by a binary system, SnO_2. At present, SnO_2 is used in various applications such as field-effect transistors [35,36], gas sensors [37–39], and transparent electrodes [3,40,41]. SnO_2 possesses rutile structure with a tetragonal unit cell with lattice parameters of $a = b = 0.4738$ nm and $c = 0.3187$ nm [42], as shown in Fig. 1.9 (a). The SnO_2 rutile structure has Sn atoms coordinated by six oxygen atoms forming SnO_6 octahedra. As seen in Fig. 1.9 (b), each SnO_6 octahedron is connected with two adjacent octahedra by their edges (corners) in the

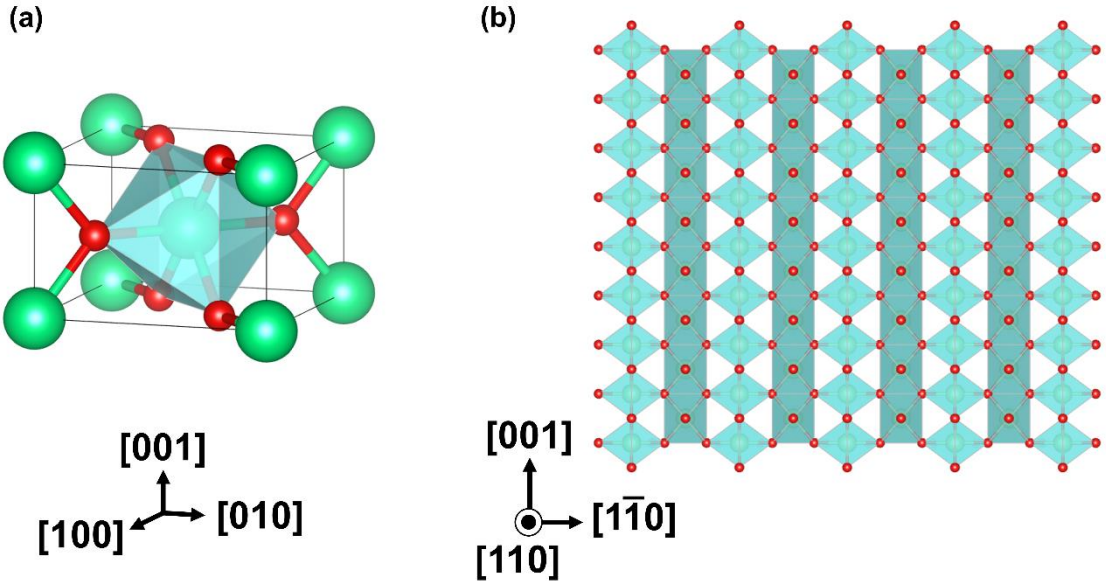

Fig. 1.9 (a) Crystal structure of the tetragonal SnO_2 using the VESTA software [145]. Green spheres indicate Sn atoms and red spheres indicate O atoms. (b) Crystal structure of the tetragonal SnO_2 from [110] direction.

c-axis (*a*- and *b*-axis) direction. In addition, the Sn^{4+} ion in SnO_2 has $5s^0$ electronic configuration. As mentioned in Section 1.2.1 (a), the structure including edge-sharing octahedra and cations possessing ns_0 electronic configuration is advantageous for achieving low m^* and thereby high μ_H. Figure 1.10 shows the density of states (DOS) of SnO_2 calculated by density functional theory within the hybrid functional framework [43]. The partial density of states (PDOS) indicates that the CBM of SnO_2 is composed of strongly hybridized Sn 5*s* and O 2*p* orbitals. The highly dispersive curve of

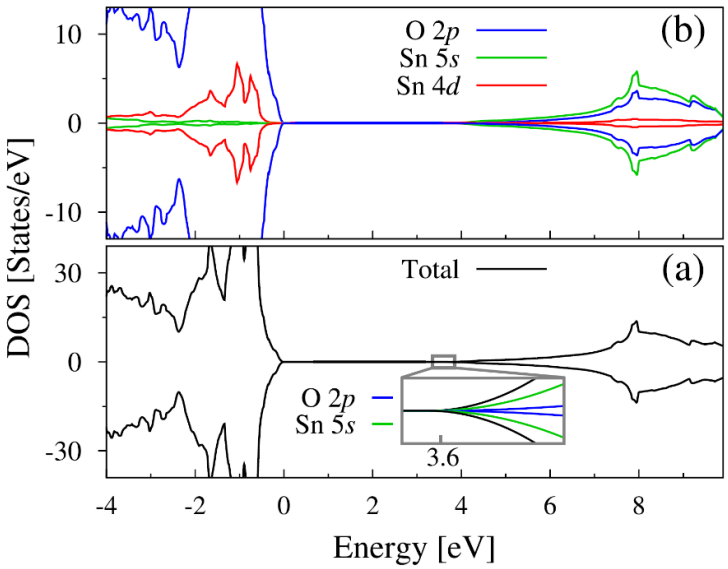

Fig. 1.10. (a) Total density of states and (b) partial density of states for SnO_2 calculated by density functional theory. The inset shows the enlarged picture around CBM. Reprinted by permission with AIP Publishing LLC [43], Copyright 2015.

Table 1.2. Basic properties of SnO_2, In_2O_3, ZnO and Si [44].

Property	In_2O_3	SnO_2	ZnO	Si
Mineral name	—	cassiterite	zincite	silicon
Average amount of the metal in the earth's crust (ppm)	0.1	40	132	2.58×10^5
Band gap E_g (300 K) (eV)	2.7 (indir) 3.75 (dir)	3.6 (dir)	3.4 (dir)	1.12 (indir) 4.18 (dir)
Static dielectric constant ε_r	≈9	∥*c*: 9.6 ⊥*c*: 13.5	∥*c*: 8.75 ⊥*c*: 7.8	11.9
Effective electron mass m^*/m_e	0.35	∥*c*: 0.23 ⊥ *c*: 0.3	0.28	0.337
Crystal structure	cubic, bixbyite	tetragonal, rutile	hexagonal, wurtzite	cubic, diamond
Space group (number)	$I2_13$ (no199)	$P4_2mnm$ (no 136)	$P6_3mc$ (no 186)	Fd3m (no 227)
Lattice parameter(s) (nm)	a: 1.012	a: 0.474 c: 0.319	a: 0.325 c: 0.5207	a: 0.5431

the states near the CBM indicates large band dispersion at the CBM, leading to small m^* in SnO_2. Indeed, SnO_2 exhibits the smallest m^* among conventional TCOs such as In_2O_3 and ZnO [44], as shown in Table 1.2.

Many efforts have been devoted to searching for high-μ_H SnO_2. The μ_H values of bulk SnO_2 single crystals range from 70 to 260 $cm^2V^{-1}s^{-1}$ at room temperature [45–47]. Figure 1.11 shows the μ_H values for undoped and Sb-doped SnO_2 single crystals as a function of temperature [45]. The figure also includes theoretical μ_H considering carrier scattering by polar optical phonon (μ_{IC}), acoustic deformation potential (μ_{AD}), and

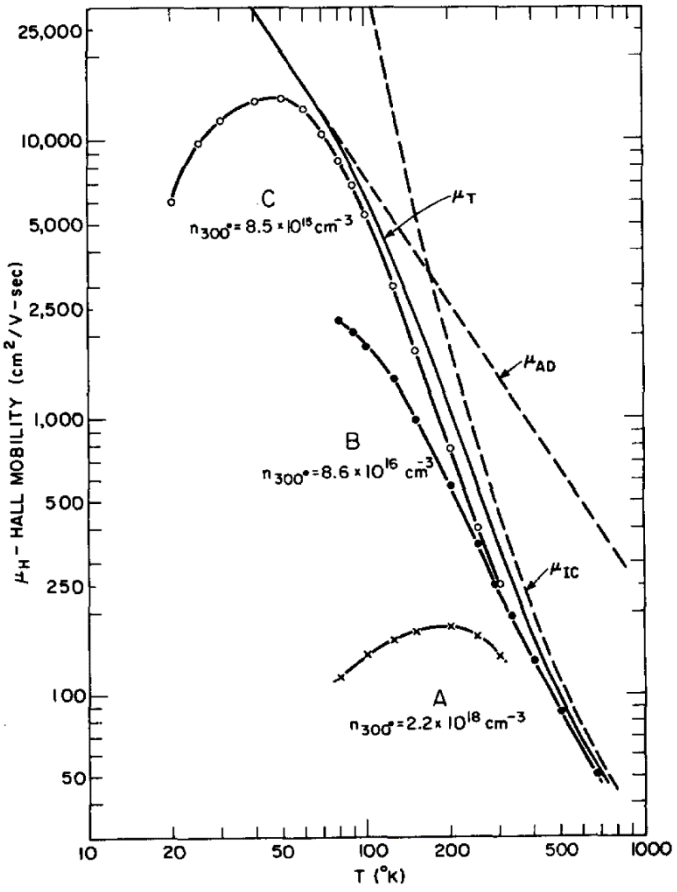

Fig. 1.11. μ_H values for undoped (A) and Sb-doped (B and C) SnO_2 single crystals as a function of temperature, plotted together with theoretical μ_H considering polar optical phonon (μ_{IC}), acoustic deformation potential (μ_{AD}) and the combination of these two scattering mechanisms (μ_T). Reprinted by permission from AIP Publishing LLC [45], Copyright 1971.

sum of these two (μ_T) [45]. Similar to other TCOs shown in Fig 1.5 in Section 1.2.1 (b), μ_H of SnO_2 single crystal is dominated by polar optical phonon scattering at room temperature, manifesting high crystalline quality.

SnO_2 thin films, however, show rather low μ_H of less than 100 $cm^2V^{-1}s^{-1}$ even in well-optimized epitaxial films [48,49], which limits the practical use of SnO_2. The lower μ_H in SnO_2 epitaxial thin films is primarily attributable to the lack of lattice-matched substrates. Thus far, corundum Al_2O_3 and rutile TiO_2 have been widely used as the substrates for the epitaxial growth of SnO_2 [50,51]. Particularly, Al_2O_3, with a high thermal and chemical stability, is suitable for the growth of SnO_2 thin films at high temperatures. Still, the SnO_2 thin films deposited on Al_2O_3 suffer from lowered crystallinity due to the crystal structure difference between the film and substrate. Indeed, very low μ_H values have been frequently observed for epitaxial SnO_2 films on Al_2O_3. TiO_2 shares the same rutile structure as SnO_2, but it has a relatively large lattice-mismatch with SnO_2, 3.1% (*a*-axis) and 7.7% (*c*-axis). As a consequence, μ_H of the undoped SnO_2 film with (001) orientation on TiO_2 (001) is limited to rather low values of ~40 $cm^2V^{-1}s^{-1}$ [52]. To overcome the above-mentioned difficulty, very thick self-buffer layers [48,49] have been employed to grow high-μ_H epitaxial SnO_2 films on Al_2O_3.

An essential point for achieving high μ_H in such highly-faulted epitaxial films is to control n_e, as reviewed in Section 1.2.1 (b). To date, much effort has been made to grow undoped [49–54] or heavily doped [55–58] SnO_2 films on a wide variety of substrates. Heavily doped SnO_2 films, albeit practically important, show low μ_H dominated by impurity scattering. Attempts to pursue high μ_H in undoped SnO_2 thin films have been unsuccessful owing to the significant carrier scattering by grain boundaries [54,59] and

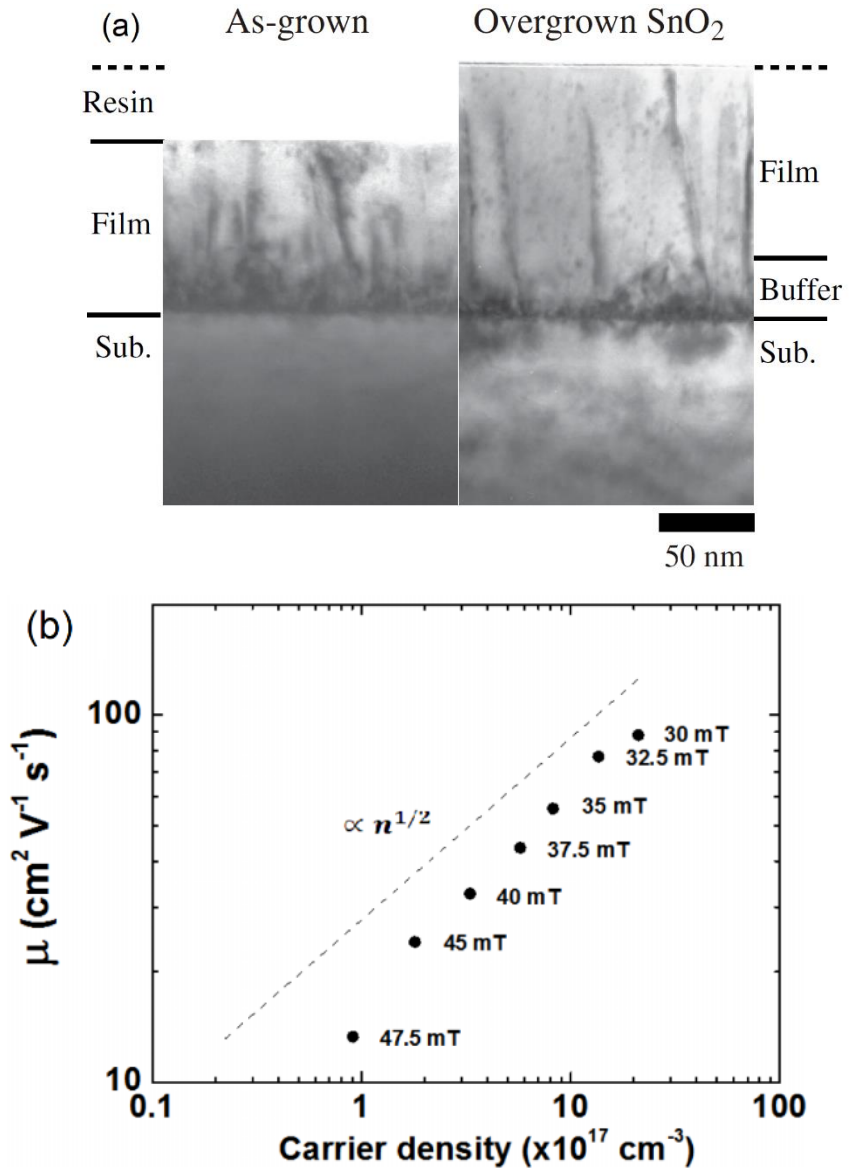

Fig. 1.12. (a) Cross-sectional TEM image of SnO_2 (001) epitaxial films on TiO_2 (001) substrates. As-grown (left) and overgrown SnO_2 (right) films [52]. (Copyright (2008) IOP Publishing Ltd.) (b) μ_H for SnO_{2-x} films on buffered *r*-plane Al_2O_3 plotted as a function of n_e at room temperature [48]. The square-root law was clearly seen, indicating the dislocation scattering is dominant (Section 1.2.1(b)). Reprinted under a Creative Commons Attribution 3.0 Unported Licence.

dislocations [25,49] induced by lattice-mismatched substrates as shown in Fig. 1.12. There is a possibility to realize high mobility in the intermediate n_e region between undoped and heavily doped SnO_2, but little attention has been paid to lightly doped [48,59] SnO_2 films.

It is also vitally crucial to select a suitable dopant of SnO_2 for achieving high-μ_H in impurity-doped SnO_2 epitaxial thin films. According to the newly established principles in Section 1.2.1 (c), a *d*-block dopant is effective for achieving high-μ_H in TCOs comprising *p*-block cation. This concept is also applicable to SnO_2. Indeed, high-μ_H in SnO_2 thin films has been realized by doping *d*-block dopants such as Ta [58,60] and W [61,62]. As for Ta-doped SnO_2, Williamson *et al.* conducted comparative experimental and theoretical studies for the transport properties of Ta-doped SnO_2 and Sb-doped SnO_2 [63]. They revealed that Ta substituting for Sn is stable and acts as a singly charged donor, based on the calculation for the defect formation energy of dopant. Moreover, the theoretical study elucidated that the Ta *d* state is located fairly above the CBM of SnO_2 ("resonant"), preventing the mixing of Ta *d* state with Sn *s* state. Contrary to Ta, Sb 5*s* states hybridized with Sn 5*s* state at the CBM, resulting in the increase of m^* and thereby decrease of intrinsic μ_H. Thus, Ta is an appropriate dopant for achieving high-μ_H with successfully controlling n_e. On the other hand, little has been known about their electric properties of W-doped SnO_2 thin films. Nakao *et al*. carried out a comparative study on W- and Ta-doped SnO_2 thin films using anatase TiO_2 seed layer and revealed that W-doped SnO_2 exhibited high-μ_H comparable to that of Ta-doped SnO_2 [61]. There remain some unanswered questions regarding the valence state of W and the local structure around W.

The theoretical calculation has become a powerful tool to explore promising dopants of TCOs. Recently, P has been theoretically predicted to be a suitable dopant for SnO_2 comparable with typical dopants such as F, Sb, and Ta in terms of the defect formation energy [43,64]; the formation energy of P^{5+} is almost the same as Sb^{5+}, which

has been widely utilized as a dopant of SnO_2 [43]. Moreover, calculation results indicated that P^{5+} is stable in SnO_2. In contrast to the extensive theoretical studies, experimental reports on P-doped SnO_2 ($Sn_{1-x}P_xO_2$, PTO) films were rather scarce. Pioneering studies by Hsu and Ghandhi demonstrated that n_e systematically increased as P concentration increased, although the n_e values and doping efficiencies were less than 1×10^{20} cm^{-3} and 10%, respectively [65]. Such low n_e in PTO can be explained by the formation of native donors, such as oxygen vacancies. Upadhyay *et al*. reported n_e exceeding 1×10^{20} cm^{-3} in PTO films using PCl_5 as a P source [66]. But they did not conduct composition analysis, and the doping efficiency and the amount of unintentional dopants such as Cl were unaddressed. Therefore, whether P serves as a suitable dopant for SnO_2 is still an open question.

n-type tin-based oxides include other promising TCOs such as $BaSnO_3$. In this study, however, I mainly focus on impurity-doped SnO_2 films, which have currently been the most widely utilized tin-based TCOs, and tackle the above-mentioned questions.

1.3.2 *p*-type tin-based transparent conductive oxides

For the realization of advanced active junction-based devices, it is necessary to combine *p*- and *n*-type materials. However, such applications are strongly limited by the current lack of suitable *p*-type TCOs [67]. The current issue for known *p*-type TCOs is the low μ_H compared to those of *n*-type TCOs. Thus, exploring mother materials for *p*-type TCOs with high-μ_H is a present challenge [68]. This low-μ_H in *p*-type oxides can be rationalized by the flat VBM with O 2*p* character, resulting in low μ_H by localization of carriers at the VBM. One of the most promising ways to realize dispersive VBM is to use main group cations with ns^2 electronic configuration (Sn^{2+}, Pb^{2+}, and Bi^{3+}, etc.). This concept is the *p*-type counterpart to the structural requirement for *n*-type TCOs with high-μ_H, introduced in Section 1.2.1 (a). Figure 1.13 shows the crystal structure and density of

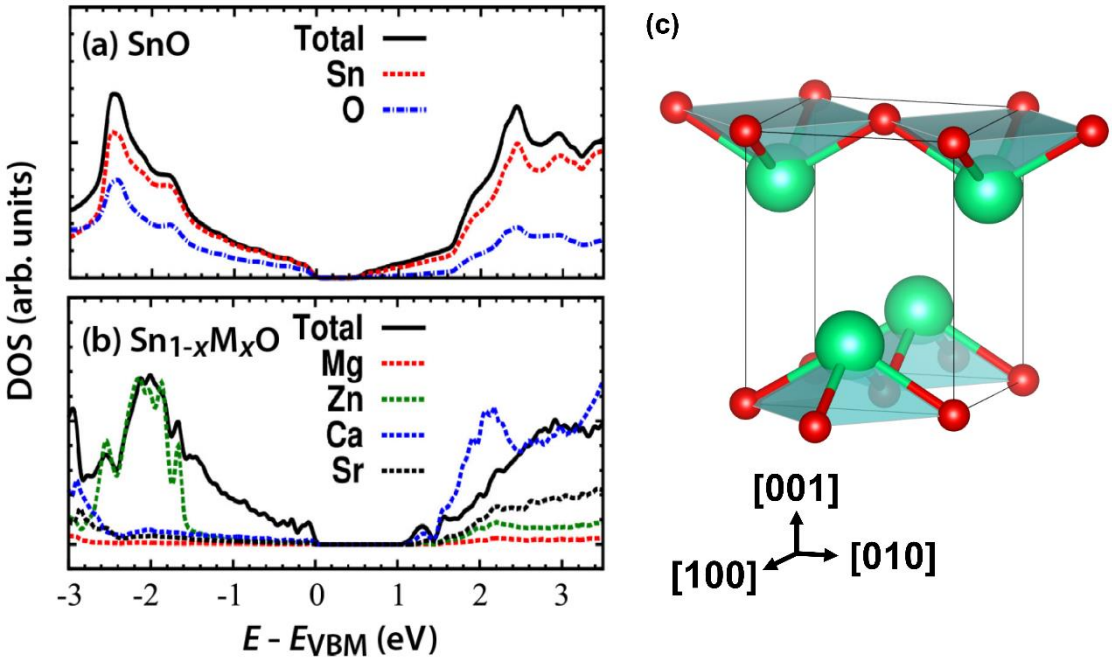

Fig. 1.13. (a) The total and local density of states calculated for (a) SnO and (b) $Sn_{1-x}M_xO$ at $x = 0.125$ where *M* is doped metal element [69]. Reprinted under a Creative Commons Attribution 4.0 License. (c) The crystal structure for litharge SnO using the VESTA software [145].

states for the simplest Sn-based *p*-type oxide, SnO [69]. SnO has a litharge structure with a tetragonal unit cell. As shown in Fig 1.13 (a), the VBM of SnO is mainly composed of Sn 5*s* state, leading to the much itinerant character of the holes in SnO.

The theoretical calculation is a powerful tool for the discovery of new Sn-based *p*-type TCOs. Figure 1.14 shows the hole effective mass (m_h) as a function of Sn-O-Sn angle for promising *p*-type Sn-based TCOs calculated by density functional theory [70]. As shown from this graph, there is a general trend that low m_h is achieved by evaluating the angle. As a whole, Sn-based TCOs are expected to exhibit high μ_H. Furthermore, Xu *et al*. predicted that tin(II) phosphates with the formulae of $Sn_2(P_2O_7)$, $Sn_3(PO_4)_2$, $Sn_4O(PO_4)_2$, and $Sn_5O_2(PO_4)_2$ [71–73] are promising candidates for *p*-type TCOs possessing both large bandgap and small hole effective mass [74]. $Sn_2(P_2O_7)$ is a

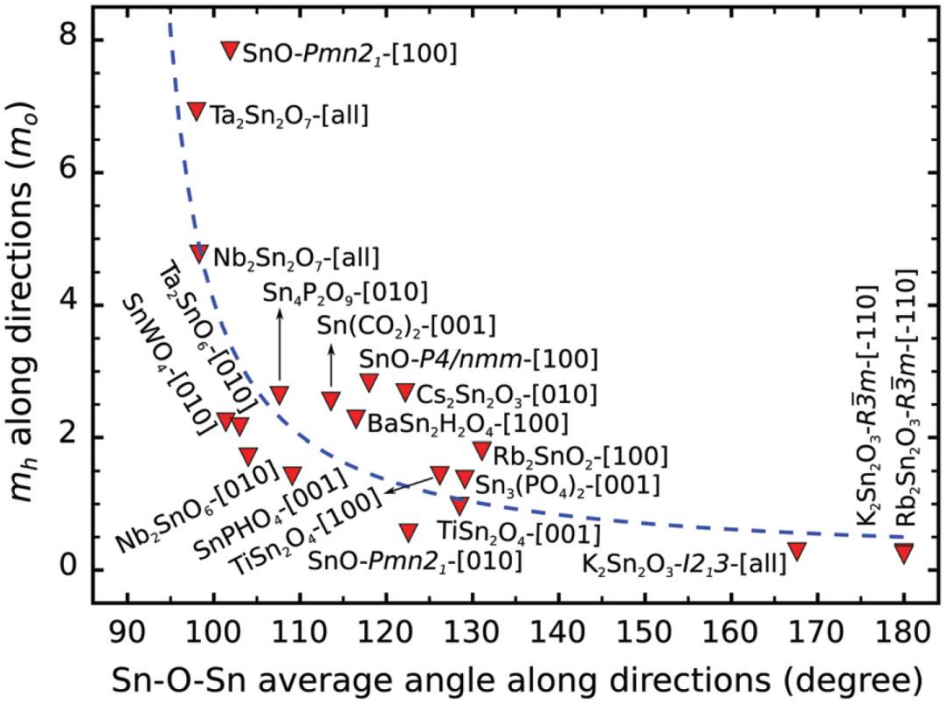

Fig. 1.14. (a) The hole effective masses (m_h) as a function of the average Sn-O-Sn angle along different directions for various Sn-based oxides. For each data point (red triangles), the chemical formula and the direction are explicitly indicated [70]. Reprinted by permission from Royal Society of Chemistry, Copyright 2013.

pyrophosphate containing $(P_2O_7)^{4-}$ anion with a P-O-P bridge. By contrast, $Sn_3(PO_4)_2$ is a simple tin(II) phosphate. $Sn_4O(PO_4)_2$ and $Sn_5O_2(PO_4)_2$ are the only two structurally-related oxy-phosphates, containing oxygen atoms bonded only to tin atoms, unlike $Sn_2(P_2O_7)$ and $Sn_3(PO_4)_2$. Figure 1.15 shows the band structures of $Sn_nP_2O_{5+n}$ (a (n = 1), b (n = 2 (α)), c (n = 2 (β)), d (n = 3), e (n = 4), and f (n = 5)) calculated by using the mBJ potential. As can be seen from Fig. 1.15, triclinic $Sn_5O_2(PO_4)_2$ is theoretically predicted to have a low hole effective mass of 1.87 m_e as well as a large bandgap of 3.40 eV [74], indicating that tin(II) phosphates could be a promising class of *p*-type conducting TCOs. In this study, I focus on the fabrication of $Sn_5O_2(PO_4)_2$ films.

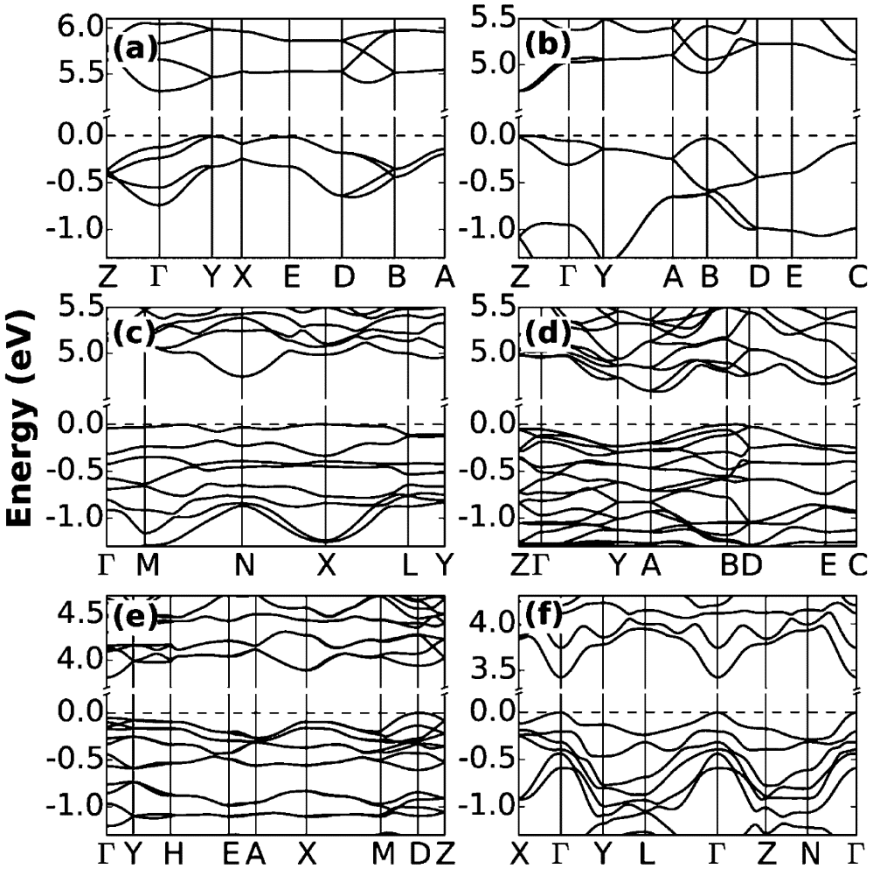

Fig. 1.15. band structures of $Sn_nP_2O_{5+n}$ (a (n = 1), b (n = 2 (α)), c (n = 2 (β)), d (n = 3), e (n = 4), and f (n = 5)) calculated by using the mBJ potential. Reprinted with permission from [73]. Copyright (2017) American Chemical Society.

1.4 Purpose of this study

As reviewed in the previous sections, there remain a lot of challenges to be tackled toward achieving high-μ_H in thin films of Sn-based TCOs. In this study, I aim to develop *n*-type SnO_2 and *p*-type $Sn_5O_2(PO_4)_2$ with high-μ_H. The background and purpose of this study are briefly summarized below.

As for SnO_2, high-quality thin films with μ_H comparable to that of bulk crystals have never been fabricated due to the lack of lattice-matched substrates. To develop a guiding principle to achieve high-μ_H in SnO_2 thin films, I investigated electron transport properties of Ta-doped SnO_2 epitaxial films, focusing on the growth orientation and n_e dependence of μ_H.

Next, I explored promising dopants of SnO_2, allowing both high μ_H and controllable n_e. As stated in Section 1.2.1 (c), the dopant is another important key to achieve high-μ_H. Recent studies on TCOs have proposed a new doping concept that facilitates effective carrier generation without decreasing μ_H. According to this concept, transition metal doping to *s*-orbital-based host materials is favorable for achieving high μ_H with controlling n_e. From this point of view, I selected W as a dopant for SnO_2 and investigated the transport properties of W-doped SnO_2 epitaxial thin films. The carrier generation mechanism of W was investigated in detail by probing local structure around doped W atoms in SnO_2.

Then I explored another promising dopant for SnO_2, P, which has been suggested as an effective dopant for SnO_2 by first-principles calculation. In contrast to the extensive studies of calculations, experimental reports on P-doped SnO_2 films were relatively scarce. Therefore, whether P serves as a suitable dopant for SnO_2 is still an open question. In this

study, I systematically investigated the transport properties of PTO films fabricated on glass and single crystalline substrates.

To implement the thin films of SnO_2 into an application, I tried to fabricate SnO_2 films in a practical manner. In thin-film Si photovoltaics, textured surfaces of TCOs are highly desirable to compensate for the low absorption coefficients of the active layers. Based on this situation, I tried to establish a fabrication technique of textured transparent conductive SnO_2 films by processing the substrates.

For realizing active junction-based devices, it is necessary to integrate *p*- and *n*-type materials. However, such applications are strongly limited due to the lack of suitable *p*-type TCOs. I selected $Sn_5O_2(PO_4)_2$ as a *p*-type host material, which has been suggested as a promising *p*-type TCOs with high-μ_H. I tried to grow phase-pure $Sn_5O_2(PO_4)_2$ thin films by using structure-directing Y_2O_3 buffer layers.

Chapter 2

Experimental techniques

2.1 Thin-film preparation

Thin-film deposition methods can be roughly classified into two groups; physical vapor deposition and chemical vapor deposition. As for physical vapor deposition, pulsed laser deposition (PLD), molecular beam epitaxy (MBE), and sputtering have been widely utilized. PLD and MBE are mainly used in lab-scale experiments and are suitable for fabricating high-quality thin films allowing the investigation of intrinsic material properties. On the other hand, sputtering is used for large-area fabrication of thin films and thus is suited for applications. In this study, I performed thin-film fabrication primarily by PLD and partly by sputtering technique, as introduced in Chapter 6.

2.1.1 Pulsed laser deposition

Figure 2.1 (a) shows a schematic illustration and a picture of the PLD system. In PLD, the constituent elements of the film are supplied to the substrate by laser ablation of a solid or liquid (called “target”). Physical aspects of the PLD process at each step are reviewed by Schou [75]. First, the laser radiation is absorbed on the surface of the target. This leads to the melting and evaporation of the material from the target if the laser fluence is large enough to induce the kinetic energy higher than the cohesive energy of

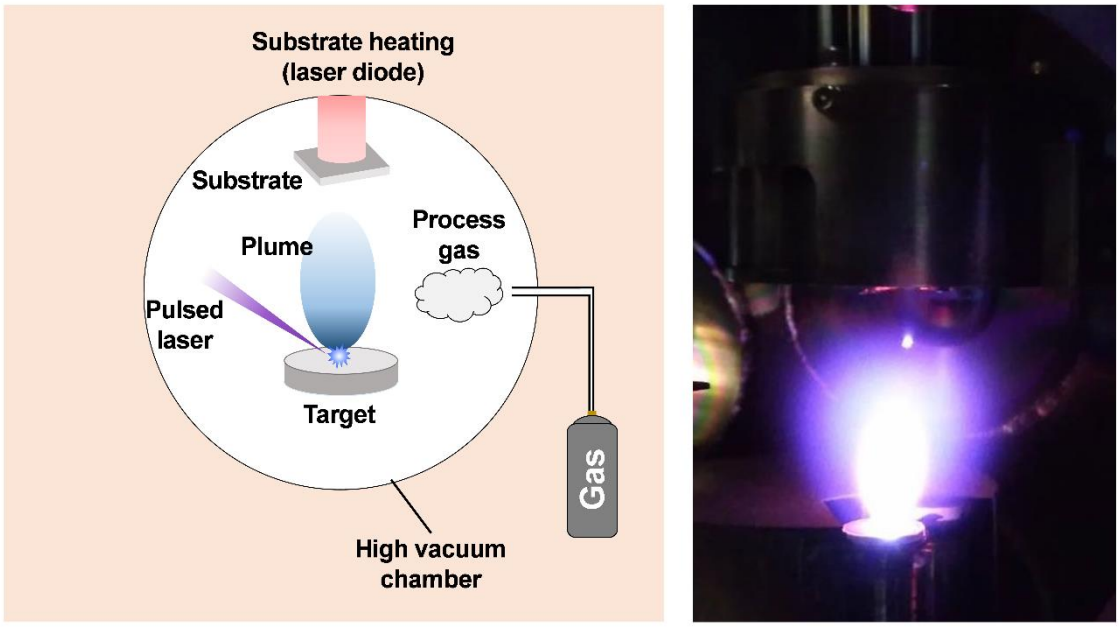

Fig. 2.1. (Left) Schematic illustration of pulsed laser deposition (Right) A picture of the ejected plume from the target during the pulsed laser deposition process

the material. Above a certain laser energy fluence, the material is evaporated from the target and interacted with the laser, forming an ejected luminous plume, as shown in Fig 2.1 (b). The threshold energy fluence for producing a plume depends on the target material itself, the morphology of the target, pulse duration, and the wavelength of the laser. The ejected plume from the target is then scattered and reacted with the background gas. The elements in the plume are adsorbed on the surface of the substrate, migrate on the surface, then nucleate for crystal growth or just form an amorphous thin film. As can be understood from the above-mentioned process, the tunable parameters in the PLD system are laser energy fluence, background gas species, its pressure, substrate temperature, and, in certain cases, target composition (see below).

The PLD technique is well suited to investigate functional oxides with multicomponent because of the following advantages:

1. Nearly stoichiometric composition transfer from the target to the thin-film sample under optimized deposition condition

2. Controllable pressure during the deposition ranging from an ultra-high vacuum (reductive) to atmospheric pressure (oxidative)
3. Ease in the fabrication of multilayers or superlattices with nanometer precision
4. The capability of ablating a wide variety of materials owing to the high energy of a pulsed beam

It should be stressed that the advantage (1) holds when the laser fluence of the focused laser is chosen properly, as Lowndes *et al.* pointed out [76]. Moreover, the stoichiometric transfer is likely to fail, especially when the film is deposited at high temperature by ablating a target containing compounds with high evaporation pressure (see Chapter 7). Such a phenomenon occurs due to the re-evaporation of the material from the substrate surface at elevated substrate temperature. If this is the case, high crystallinity, which is generally accessible by high-temperature fabrication, is incompatible with the stoichiometric composition of the film. Even in such a case, it is often effective to change target composition and/or apply the solid phase crystallization method, which can compensate the easily-evaporating materials inside the films, for obtaining stoichiometric thin films with high crystallinity [77,78].

2.1.2 Sputtering deposition

Film deposition by sputtering [79] is the most popular method for practical large-area film deposition of TCOs. The sputtering deposition is based on the ion bombardment of a target. Ion bombardment occurs when cation species in a plasma generated by electrical discharge in process gas hit the target. This ion bombardment produces vapor of the target substances, which are transferred and deposited on a

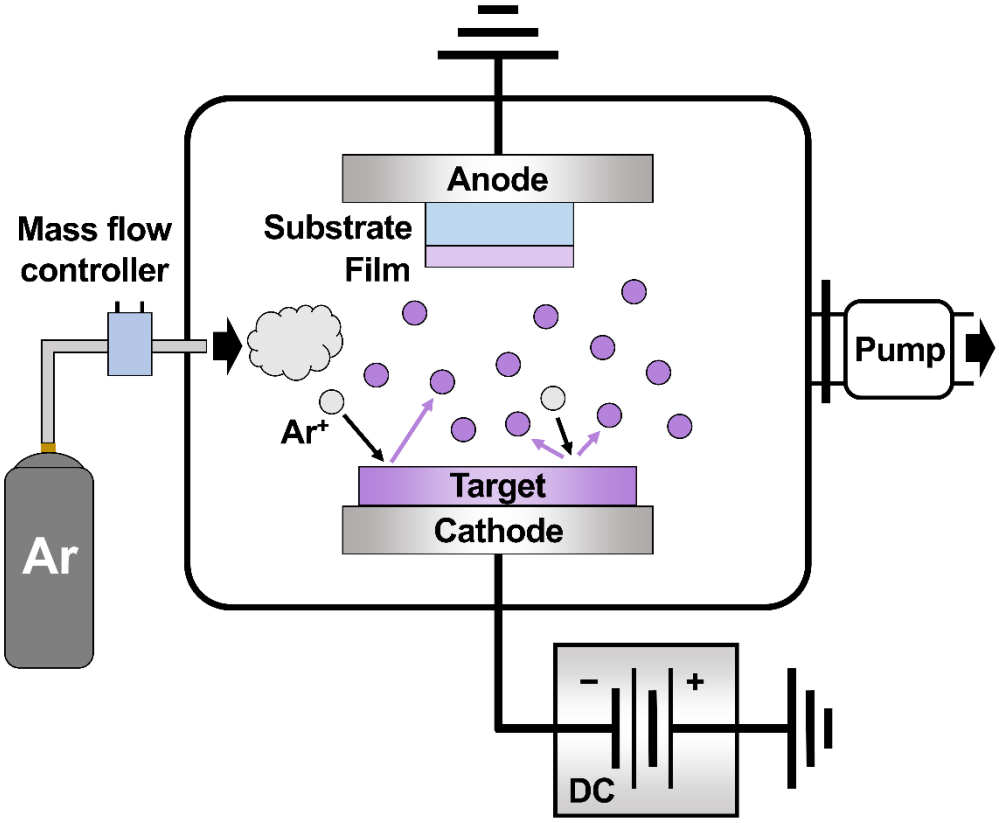

Fig. 2.2. Schematic illustration of a basic DC sputtering system

substrate to make thin films. Ar gas is generally used as a process gas for electrical discharge. There are two modes for supplying electrical power: direct current (DC) and radio frequency (RF) modes. Figure 2.2 shows a schematic illustration of a basic DC sputtering system. As for DC sputtering, the substrate is placed on the anode side, and negative bias is applied to the target, composed of conducting compounds. DC sputtering is inapplicable to insulating materials because the surface of the target is positively charged by the collisions with cations. In RF sputtering, on the other hand, RF bias causes electrons and cations to hit the surface of the target alternatively, preventing the charging of the target. Thus, RF sputtering can be used to fabricate thin films by using both conducting or insulating targets.

In this study, I performed thin-film fabrication by DC magnetron sputtering as in

Chapter 6.

2.2 Crystallographic characterization

This section introduces two complementary methods for structural characterization of thin films, X-ray diffraction and transmission electron microscopy. X-ray diffraction is commonly used to probe the macroscopic crystal structure in a micrometer size, whereas a transmission electron microscope gives structural information with sub-nanometer resolution. In addition to these methods, I introduce X-ray fluorescence holography, which allows the investigation of the local atomic environment around a certain atom (emitter). Structural information obtained by these methods often helps us elucidate the mechanism behind the physical properties of the material (see Chapter 3 and Chapter 4).

2.2.1 X-ray diffraction

X-ray diffraction is commonly used as a fundamental technique for the determination of crystal structure. X-rays are electromagnetic radiation with wavelengths of the order of an Ångström (10^{-10} m), which is almost the same order as the spacing between crystal planes (*d*-spacing). Such a feature allows the investigation of the atomic structure of not only bulk samples but also of nano-scale materials, e.g., nanoparticles and ultra-thin films in the range of nanometers. Here I summarize the basic principles of XRD and various operation modes of XRD measurements.

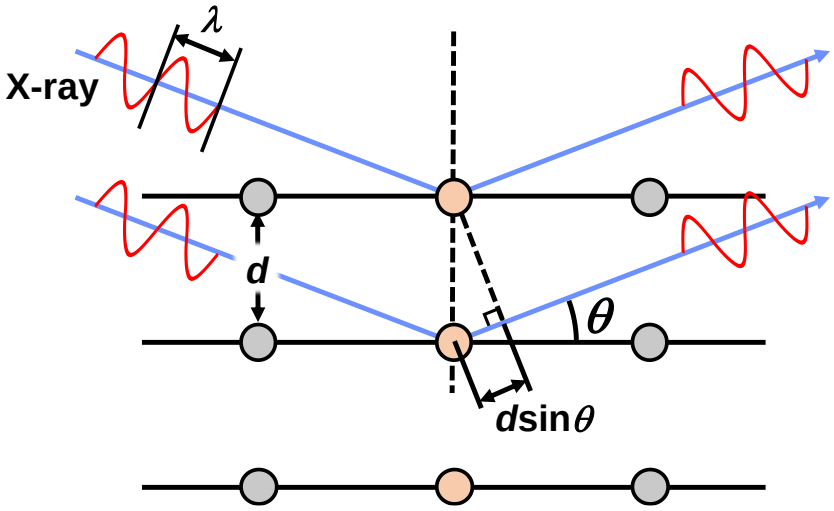

Fig. 2.3. A schematic illustration of the concept of Bragg's law.

Basic principle: Bragg's law

A simple explanation for the diffraction of X-rays from a crystal was proposed by W. L. Bragg. Figure 2.3 schematically shows the concept of Bragg's law. When a monochromatic X-ray with a wavelength λ is irradiated to a crystalline sample, the incident X-ray is scattered by the sample. In Fig 2.3, two of the X-ray beams are drawn for simplicity. The optical path difference between the two beams is $2d\sin\theta$, where d is the lattice spacing between the crystalline planes and θ is one-half of the angle between the incident and reflected X-ray. Thus, Bragg's law

$$n\lambda = 2d\sin\theta \tag{2-1}$$

is derived, where n is an integer. Eq. (2-1) is the condition under which constructive interference of X-ray beams occurs.

Operation modes

Figure 2.4 is a schematic illustration of the XRD instrument used in this study, which allows rotating the 4-axis (or to change the angles ϕ, χ, ω and θ). Various

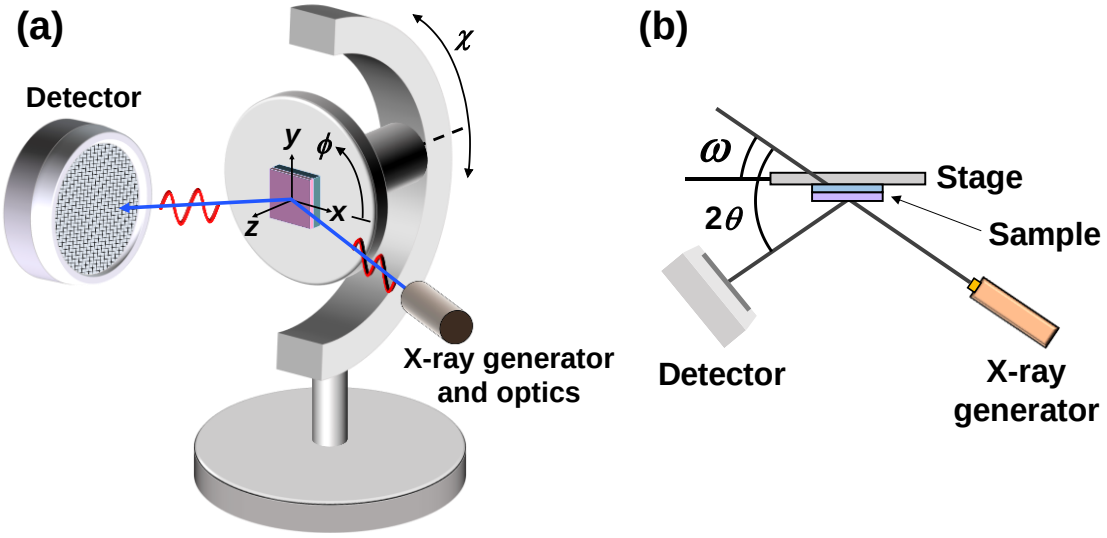

Fig. 2.4. A schematic image of the XRD measurement setup showing the direction of controllable 4-axis, (a) ϕ, χ, (b) ω and θ.

crystallographic information of a thin film can be obtained by changing these angles, as described below.

Coupled ω-2θ (θ-2θ) scan

In coupled ω-2θ scan, the angle between sample and X-ray generator, ω, is fixed at θ, which is one-half of the angle between the incident and reflected X-ray. The coupled ω-2θ scan is used for detecting symmetric reflections from the targeting films and the substrates. Diffraction peaks appear when θ satisfies Bragg's condition, from which the lattice spacing can be calculated. One can derive lattice constants of epitaxial films by out-of-plane ($\chi = 90°$) and in-plane ($\chi \neq 90°$) coupled ω-2θ scan.

ω-scan

ω-scan is a decoupled ω-2θ scan with a fixed 2θ value, which is also called as X-ray rocking curve (XRC) measurement. In ω-scan, the detector is fixed at the Bragg angle (θ_B) from the sample. The sample is then rotated ("rocked") around $\omega = \theta_B$, while the fixed detector records the intensity of the beam reflected from the sample. The full

width at half maximum (FWHM) of the obtained rocking curve provides information on the crystallinity of a sample (see Chapter 3, 4, and 5).

ϕ-scan

The XRD stage can rotate by an angle ϕ, which allows detecting in-plane Bragg peaks. ϕ-scan is usually used to check the in-plane symmetry of a single-crystalline sample by detecting in-plane Bragg peaks from the inclined sample ($\chi \neq 90°$). The ϕ-scan is particularly useful for checking the domain structure of the sample or determining the epitaxial relationship between film and substrate.

Reciprocal space mapping

Reciprocal space mapping (RSM) is a powerful technique to confirm the epitaxial relation between a film and substrate directly. RSM pattern is recorded by adjusting both 2θ and ω values. The pair of real space coordinate (2θ, ω) is transformed into the reciprocal space coordination (q_x, q_z) by the following equation:

$$q_x = \frac{1}{\lambda}\left\{\cos\left(2\theta - \omega\right) - \cos\omega\right\} \tag{2-2}$$

$$q_z = \frac{1}{\lambda}\left\{\cos\left(2\theta - \omega\right) + \sin\omega\right\} \tag{2-3}$$

where λ is the wavelength of the irradiated X-ray. When the films are coherently grown on a substrate, the in-plane value for the film, i.e., q_x, is the same as that of the substrate. In contrast, when film relaxation occurs, the in-plane value for the film would approach that for the bulk value.

2.2.2 Transmission electron microscopy

Transmission electron microscopy (TEM) is a technique to visualize the

structure of materials with atomic resolution by using a transmitted electron beam. TEM provides structural information on the scale ranging from sub-nanometer to several tens of micrometer. Particularly, in the case of thin films, TEM can characterize not only the crystallographic structures of the film and substrate underneath but also the structure of defects such as dislocations and grain boundaries.

For the TEM measurement, the samples need to be thinned down to several hundreds of nanometers so that the electrons transmit in the film. The TEM specimen is prepared by some slicing techniques such as ion milling or focused ion beam technique.

The images obtained by TEM measurements can be classified into two, bright-field image and dark-field image. Bright-field image is the traditional imaging constructed from the transmitted electrons through the specimen without much deflection. Since the bright field mode selects an unscattered electron beam, dark contrast indicates that the electrons are absorbed or diffracted. Thus, heavy atoms are imaged with dark contrast. On the other hand, a dark-field image is produced by diffracted waves, enabling the analysis of lattice defects such as dislocations and stacking faults inside the specimen.

2.2.3 X-ray fluorescence holography

X-ray fluorescence holography (XFH) is a technique to determine the 3D atomic structure of a crystalline sample [80,81]. Figure 2.5 shows a setup for measuring XFH [82]. XFH has two measurement modes, normal mode and inverse mode, which can be summarized as follows. When an X-ray possessing higher energy than the absorption edge of the targeting element (emitter) is irradiated to a crystalline sample, the emitter generates a fluorescent X-ray with energy corresponding to the absorption edge of the emitter. The emitted X-ray partially arrives at the detector without scattering. The rest of the emitted X-ray is scattered by the atoms surrounding the emitter and then arrives at the detector. In the normal mode, the unscattered and scattered fluorescent X-ray is

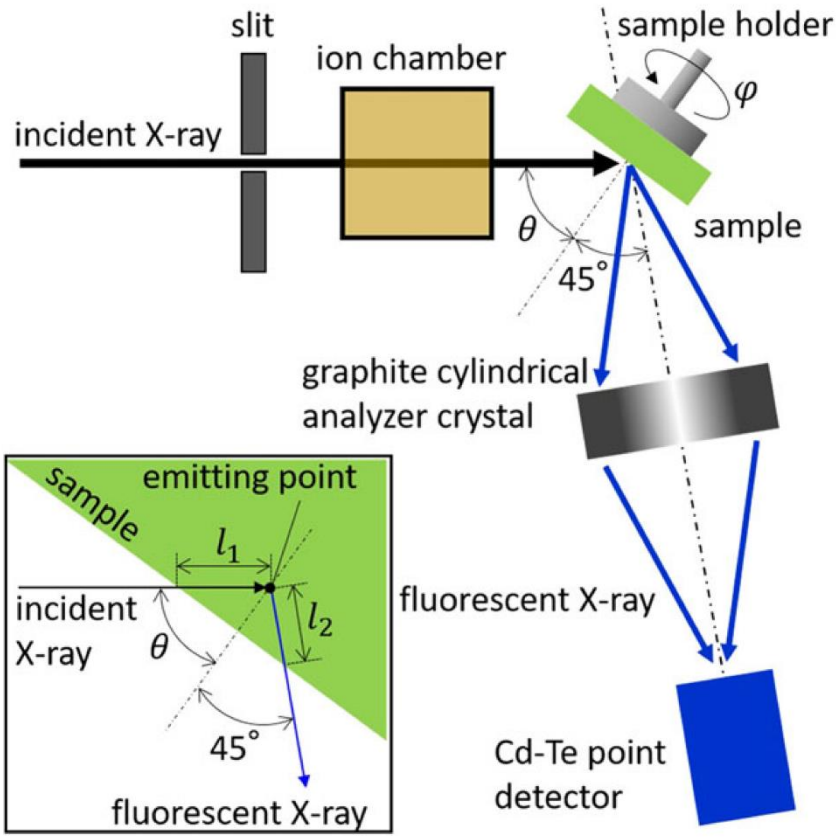

Fig. 2.5. Schematic image of the experimental setup for measuring XFH. Inset shows the enlarged image around the emitting point. Reprinted from Ref [82] with permission from John Wiley and Sons, Copyright 2018.

treated as a reference and objective waves, respectively. The inverse mode is based on the optical reciprocity of the normal mode. Most of the XFH measurements in synchrotron radiation facilities have been performed by using inverse mode because of the experimental advantage, that is, energy-tunable X-ray sources. Ghost images are considerably suppressed by using multiple-energy X-ray holograms. [81]. In this study, inverse mode XFH measurements were performed on beamline BL13XU of SPring-8 (Chapter 4).

2.3 Composition analysis

Analysis of chemical composition often helps us understand the structure and physical properties of TCOs. For example, as briefly mentioned in Chapter 1, deviation of oxygen content from stoichiometry causes intrinsic carrier doping, severely affecting the electrical properties of TCOs. As mentioned in Chapter 2.1, PLD basically guarantees the stoichiometric transfer from the target to the substrate. However, this is not the case when the thin film or target contains volatile compounds. In such a situation, film composition does matter. This section introduces two measurement techniques for composition analysis of thin films used in this study (see Chapter 4, 5, and 7).

2.3.1 Energy-dispersive X-ray spectroscopy

Energy-dispersive X-ray spectroscopy (EDX, EDS) is a technique to determine the elemental composition of a sample by detecting the characteristic X-ray emitted from the constituent atoms in the sample. The energy of characteristic X-ray corresponds to

each element, which allows the identification of the constituent elements in the sample. The intensity of each elemental peak provides information about the composition of the sample. The mechanism can be simply explained as follows: When an electron beam is irradiated to the atoms, inner-shell electrons are excited and ejected outside the atom, creating vacancies in the inner-shell. Then, the outer-shell electrons fill the vacancy in the inner-shell. In this process, the energy difference between the higher and lower energy shells is emitted in the form of characteristic X-rays. Since characteristic X-rays have specific energies depending on the element, elemental analysis can be performed by measuring these energies. It should be noted that the charging effect is non-negligible, particularly when one measures the insulating sample. To obtain a much accurate result, the charging effect must be removed by depositing a conducting layer on the sample such as carbon or platinum. EDX is usually installed in a scanning electron microscope (SEM) or transmission electron microscope.

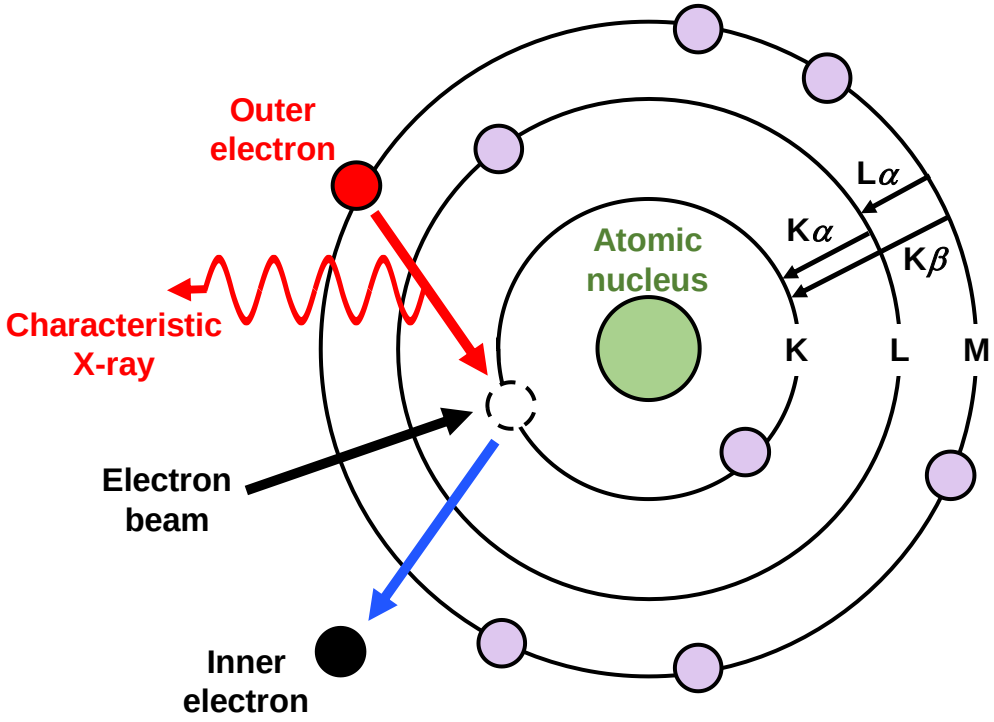

Fig. 2.6. A schematic image of the principle of EDX.

2.3.2 Rutherford backscattering spectrometry

Rutherford backscattering spectrometry (RBS) is widely utilized as a non-destructive quantification technique to determine the chemical composition of materials [83–85]. Figure 2.7 explains the basic experimental setup for the RBS measurement [86]. A target placed at the center of the chamber is bombarded by the incident ions with MeV energy. Then the energy and intensity of the backscattered particles are recorded by a conventional solid-state detector (SSD) as RBS spectra. The RBS spectra provide three kinds of information on the thin film: the type of the constituent elements in the film, the depth distribution of the constituent elements, and the concentration of each element.

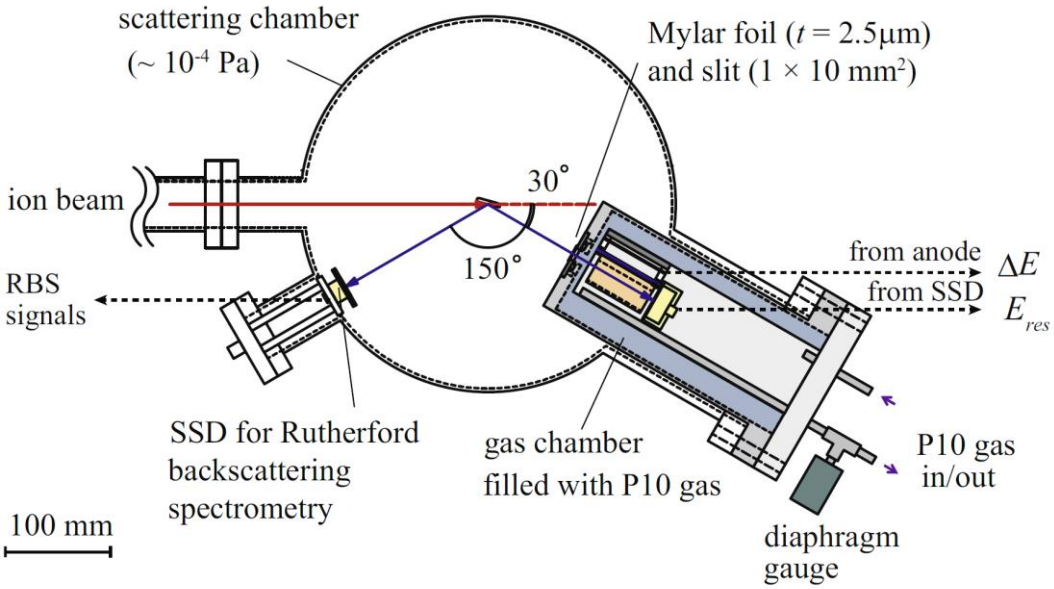

Fig. 2.7. A schematic image of the Rutherford backscattering spectrometry system. Reprinted from Ref [86] with permission from Elsevier, Copyright (2016).

2.4 Optoelectronic characterization

2.4.1 Four-point probes method

The four-point probes method is a convenient technique to measure electrical transport properties such as resistivity and sheet resistance, as shown in Fig. 2.8 (a). In this technique, the current is supplied by a pair of probes. The voltage between an inner pair of probes is measured using a voltmeter, allowing a much more accurate evaluation of resistance than the two-point probes method. In the two-probes method, two terminals are used for carrying the current and sensing the voltage, and thus the measured resistance is the sum of the lead and contact resistance (R_{lead}) and the sample resistance (R_{sample}) (Fig. 2.8 (b)). On the other hand, in the four-point probes method, voltage probes are separated from the current probes so that no voltage drop occurs between voltage sensing probes. Thus the contribution from R_{lead} is eliminated (Fig. 2.8 (c)). By using this method, much accurate volumetric resistance of the sample can be evaluated.

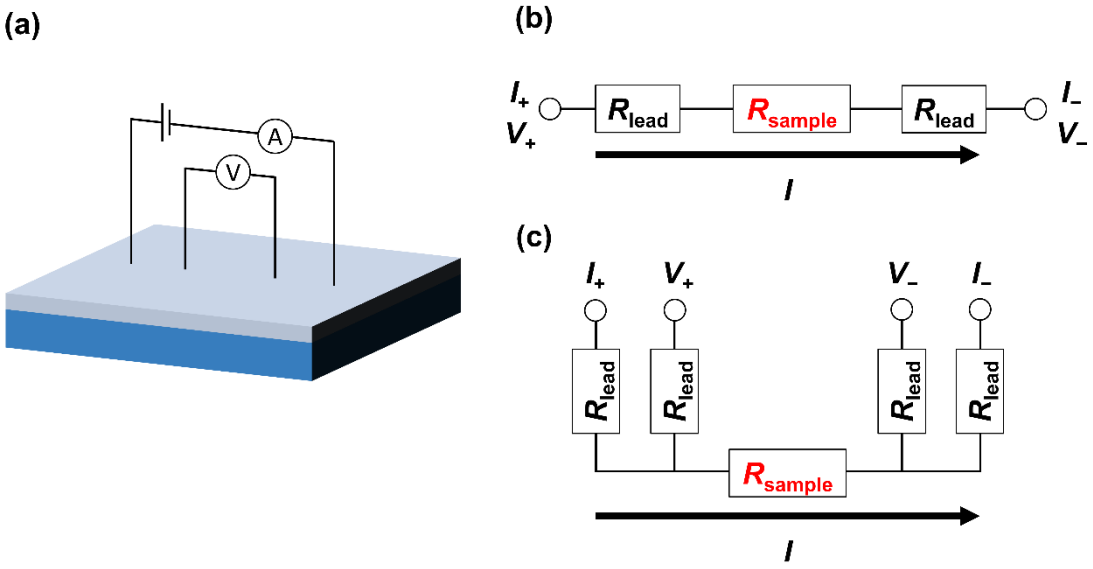

Fig. 2.8. Schematic images of (a) four-point probe configuration. Equivalent circuit diagrams for (b) two-probe and (c) four-probe sensing. *I*: current, *V*: voltage.

2.4.2 Hall effect measurement

Hall effect is a generation of an electric field perpendicular to the applied electric and magnetic field. Hall effect measurement is performed to evaluate the carrier type and the carrier transport properties such as ρ, n_e, and μ_H. Figure 2.9 (a) shows an experimental configuration of Hall effect measurement for a thin film sample in this study. Voltage is applied along the *x*-direction and an electric current, *I*, flows along *x*. The resistance is measured by the aforementioned four-point probes method, ensuring the measured resistance is free from the wire resistance or the contact resistance. The magnetic field **B** = μ_0**H** points in the *z*-direction, where μ_0 is the permeability of vacuum and **H** is the magnetic field strength. When a carrier, *q*, is traveling through the sample at a velocity of **v**, Lorenz force is derived as

$$\mathbf{F} = q(\mathbf{v} \times \mathbf{B}). \tag{2-4}$$

The Lorenz force causes the accumulation of electrons at one side of the sample, as schematically shown in Fig 2.9 (b), which leads to the production of an electric field along the *y*-direction, E_y. After the system reaches the equilibrium state, the following equation holds:

$$\left(q(\mathbf{v} \times \mathbf{B})\right)_y + qE_y = 0. \tag{2-5}$$

The current density in the *x*-direction, j_x, is given by $j_x = nqv_x$. Therefore, E_y is derived as follows:

$$E_y = \frac{j_x B_z}{nq}. \tag{2-6}$$

Here, Hall coefficient, R_H, is defined as

$$R_{\mathrm{H}} \equiv \frac{E_y}{j_x B_z} = \frac{1}{nq}. \tag{2-7}$$

When R_{H} is negative (positive), the major carriers inside the film are electrons (holes). By substituting $E_y = V_{\mathrm{H}} / w$ and $j_x = I / wt$ (w and t represent the width and the thickness of the film), the equation of R_{H} can be transformed into the following equation:

$$\frac{V_{\mathrm{H}}}{I} = \frac{R_{\mathrm{H}}}{t} B_z \tag{2-8}$$

where V_{H} denotes the Hall voltage. In a Hall-effect experiment, V_{H} / I (Hall resistance) is measured with changing **B**, and then R_{H} / t is evaluated. By using R_{H}, n_{e} and μ_{H} are

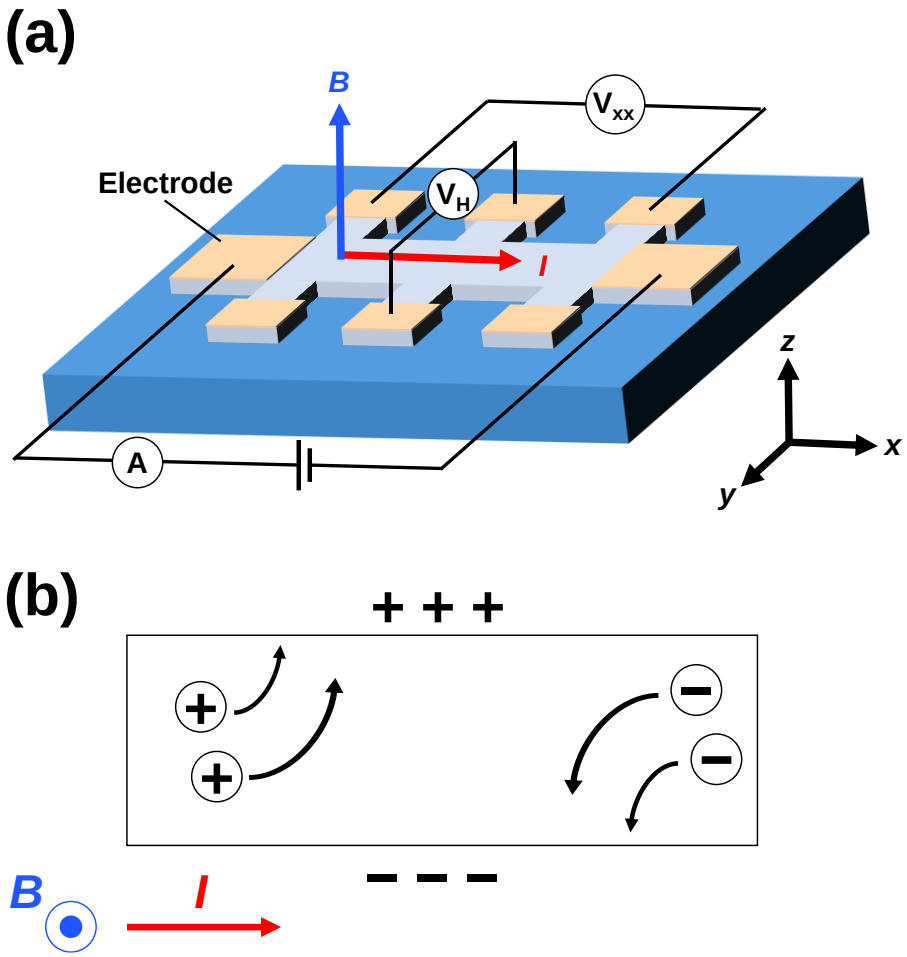

Fig. 2.9. (a) An experimental configuration of Hall effect measurement on a Hall-bar patterned sample. (b) Schematic image of Hall effect.

expressed as follows:

$$n_{\mathrm{e}} = \left| \frac{1}{R_{\mathrm{H}} q} \right| \tag{2-9}$$

$$\mu_{\mathrm{H}} = \left| \frac{R_{\mathrm{H}}}{\rho} \right| \tag{2-10}$$

2.4.3 Ultra violet-visible-near infrared spectroscopy

Ultraviolet-visible (UV-vis) or near-infrared (NIR) spectrophotometer is a powerful tool to explore the electronic structure of a material. The measurement involves absorption or reflection spectroscopy in the spectral region ranging from UV to NIR. The absorptance (A) and absorption coefficient (α) of a thin film are approximately written as

$$A = 1 - T - R \tag{2-11}$$

$$\alpha = \frac{1}{t} \ln \frac{1}{T} \tag{2-12}$$

where t is film thickness, T is transmittance, and R is reflectance. These equations do not consider the multiple reflections from the sample.

Chapter 3

High mobility approaching the intrinsic limit in Ta-doped SnO_2 films epitaxially grown on TiO_2 (001) substrates *

3.1 Introduction

As mentioned in Chapter 1, SnO_2 has been extensively studied as a practical transparent oxide semiconductor. In this chapter, I focus on lightly doped SnO_2 thin films to achieve a high μ_H. I investigated the electrical transport properties of lightly Ta-doped SnO_2 ($Sn_{1-x}Ta_xO_2$, TTO) films grown on TiO_2 (001) substrates, which are isostructural to SnO_2, with the smallest lattice mismatch. I found that the increase in n_e by Ta-doping dramatically enhanced μ_H, probably owing to a screening of the carrier scattering by the grain boundaries and dislocations. The TTO films with $n_e \sim 1 \times 10^{20}$ cm^{-3} exhibited μ_H of

* This chapter contains the contents of the following publications.

M. Fukumoto, S. Nakao, K. Shigematsu, D. Ogawa, K. Morikawa, Y. Hirose, and T. Hasegawa, Sci. Rep. **10**, 6844 (2020).

130 $cm^2V^{-1}s^{-1}$, which is the highest among SnO_2 films thus far reported. Moreover, this value is close to the intrinsic limit of μ_H calculated by assuming that only phonon and ionized impurities contribute to the carrier scattering.

3.2 Method

TTO films with a thickness of 100–120 nm, with $x = 3 \times 10^{-5}$–1×10^{-2}, were grown on TiO_2 (001) substrates by pulsed laser deposition (PLD) with a KrF excimer laser. TTO films with $x = 3 \times 10^{-3}$ were grown (001)-, (101)-, and (110)-planes of TiO_2, and m-, r-, and c-planes of Al_2O_3 substrates. The repetition rate and the fluence of the laser were set at 2 Hz and 1–2 $J \cdot cm^{-2}$, respectively. The typical growth rate was 0.14–0.17 Å per shot. Sintered pellets of TTO with $x = 3 \times 10^{-4}$–1×10^{-2} were used as PLD targets. TTO films with $x = 3 \times 10^{-5}$ were fabricated by alternating ablation [59] of a commercial undoped SnO_2 (4N purity, Toshima MFG) target and a TTO pellet with $x = 3 \times 10^{-4}$. In this study, nominal x values were used to represent the chemical compositions of the films because the stoichiometric transfer of Ta from the targets to the films has been reported for TTO films grown under a similar condition [59]. The base pressure of the PLD chamber was maintained at 3×10^{-9} Torr. Oxygen partial pressure and T_s during film growth were 1×10^{-2} Torr and 400–700 °C, respectively. Crystal structure and crystallinity were evaluated by XRD measurements using a four-circle diffractometer (Bruker AXS, D8 DISCOVER). The cross-sectional microstructure of the films was observed by using a transmission electron microscope (FEI, Titan Cubed G2 60-300) operated at 300 kV. Hall effect and resistivity were measured by using a standard six-

terminal method. The Hall-bar width and the distance between voltage terminals for four-probe measurements were 1 mm and 2.4 mm, respectively. Ag or In electrodes were used for ohmic contacts. A laboratory constructed system equipped with a 2 T electromagnet was used for room temperature measurements. Current–voltage characteristics and Hall voltage-magnetic field characteristics were measured repeatedly (at least twice) to confirm the reliability and reproducibility of the measurements. Temperature dependence of the transport properties was measured with a commercially available system (Quantum design, physical properties measurement system (PPMS Model 6000)).

3.3 Results and discussion

I first optimized the substrate temperature (T_s) for the growth of the TTO film, where the Ta content x was fixed at 3×10^{-3}. Figure 3.1 (a) shows θ-2θ X-ray diffraction (XRD) patterns for the TTO films prepared at various T_s. Only 002 diffraction peaks from SnO_2 and TiO_2 were observed in all the films, which indicated epitaxial growth of (001)-

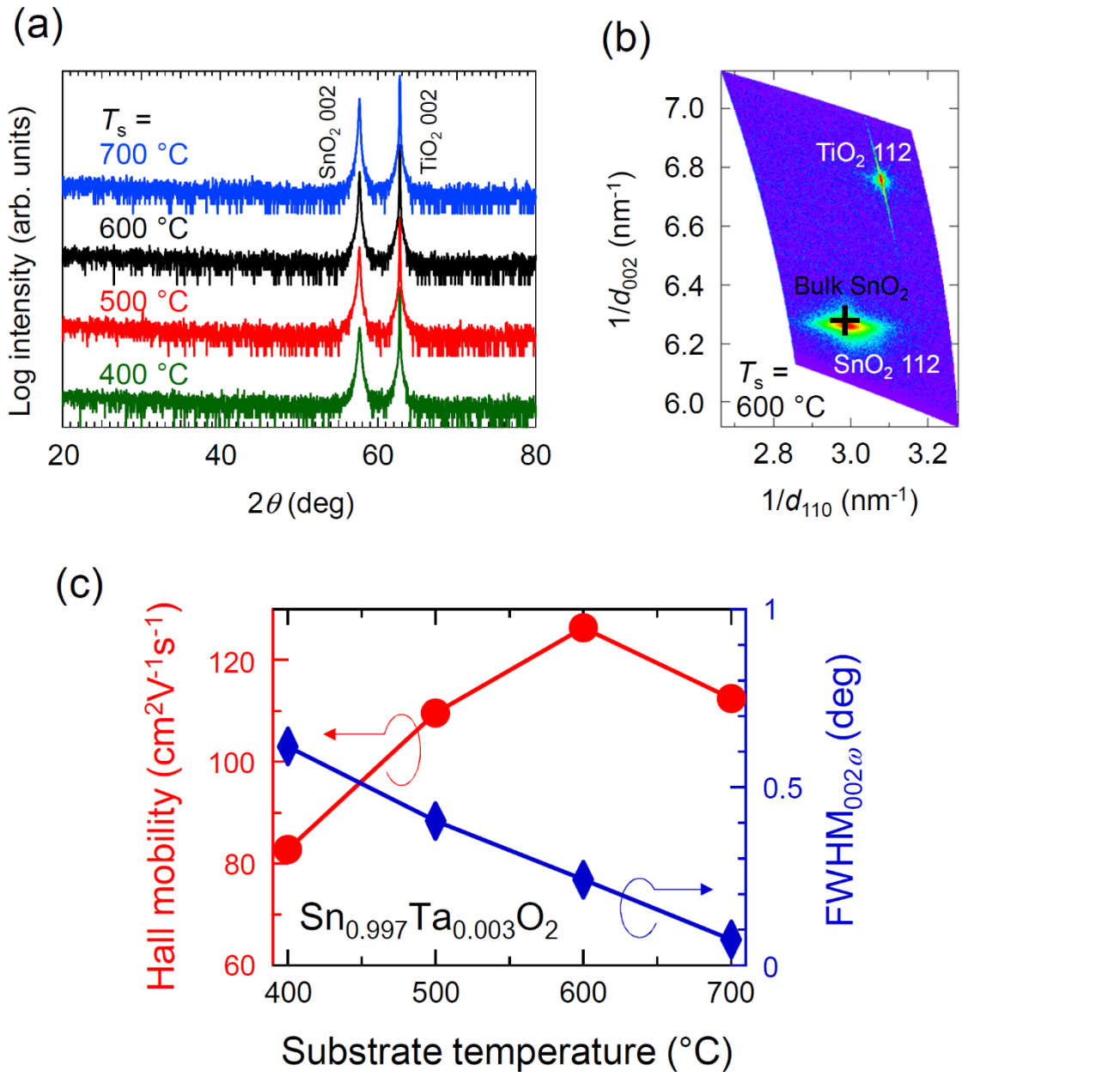

Fig. 3.1. (a) ω-2θ X-ray diffraction patterns for $Sn_{1-x}Ta_xO_2$ (TTO) films with $x = 3 \times 10^{-3}$ grown at various substrate temperatures (T_s). (b) A reciprocal space map around the asymmetric 112 diffraction peaks for a TTO film grown at T_s = 600 °C. A cross represents the peak position for bulk SnO_2. (c) T_s dependence of Hall mobility (μ_H, circles) and full width at half maximum of rocking curve (ω scan) for 002 diffraction peak ($FWHM_{002\omega}$, diamonds) for the TTO ($x = 3 \times 10^{-3}$) films.

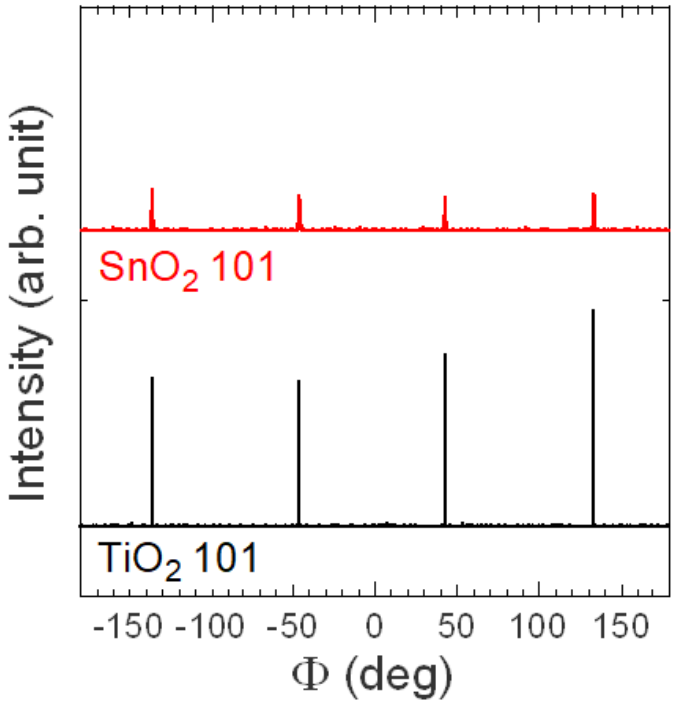

Fig. 3.2. Off-specular Φ-scan of 101 diffraction peak from $Sn_{1-x}Ta_xO_2$ (TTO) film with $x = 3 \times 10^{-3}$ and 101 diffraction from TiO_2 substrate. The epitaxial relationship is $SnO_2(001)[100]$ // $TiO_2(001)[100]$.

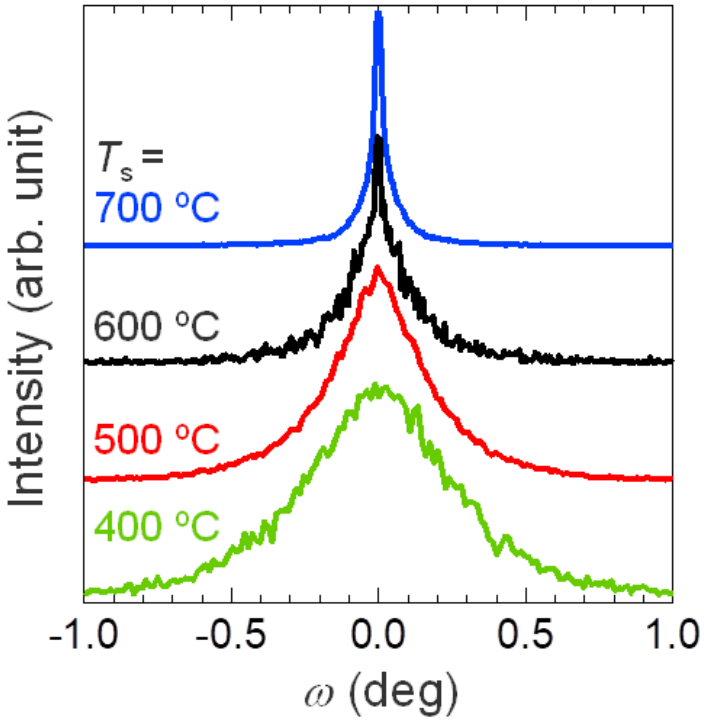

Fig. 3.3. Rocking curves (ω scan) of the 002 diffraction for TTO films with $x = 3 \times 10^{-3}$ grown at various substrate temperatures (T_s).

oriented SnO_2 films on TiO_2 (001) without any impurity phases. Epitaxial growth of the SnO_2 films was further confirmed by an off-specular Φ-scan of 101 diffraction peaks from SnO_2 and TiO_2 substrates (Fig. 3.2). Figure 3.1 (b) shows the reciprocal space map observed around the asymmetric 112 diffraction peak for the TTO film grown at T_s = 600 °C. The film was almost fully relaxed, as reported [52] for undoped SnO_2 films on TiO_2 (001). Figure 3.1 (c) plots the full width at half maximum of the rocking curve (Fig. 3.3) of the 002 diffraction ($FWHM_{002\omega}$) as a function of T_s. Notably, $FWHM_{002\omega}$ monotonically decreased with an increase of T_s and reached 0.07° at the highest T_s = 700 °C. This $FWHM_{002\omega}$ value is much smaller than that reported for the SnO_2 film on a thick self-buffer layer [48], that is, 0.31°, which indicated very high crystallinity of the present TTO film. A similar trend, that is, improved crystallinity at high T_s, was reported in the previous research on SnO_2 epitaxial films [59,87,88]. The TTO films grown at higher T_s tended to exhibit higher μ_H, as shown in Fig. 3.1 (c). However, a slight decrease in μ_H was observed for the film grown at T_s = 700 °C in spite of the good crystallinity. I speculate that at such high T_s, interdiffusion of Sn and Ti atoms occurred at the film/substrate interface [89], which might have caused impurity scattering and thus suppressed μ_H. Hereafter, I fixed T_s at 600 °C.

Next, I investigated the dependence of the transport properties of the TTO films on x. As shown in Fig. 3.4, the TTO film with the lowest $x = 3 \times 10^{-5}$ showed $n_e = 4 \times 10^{17}$ cm^{-3} and $\mu_H = 36$ $cm^2V^{-1}s^{-1}$, which are close to those [52] reported for undoped SnO_2 films on TiO_2 (001). Furthermore, n_e was proportional to x and lay on the line representing a 100% doping efficiency, which indicated that each Ta^{5+} ion generated one carrier electron. This implied that the lightly-doped TTO films were free from

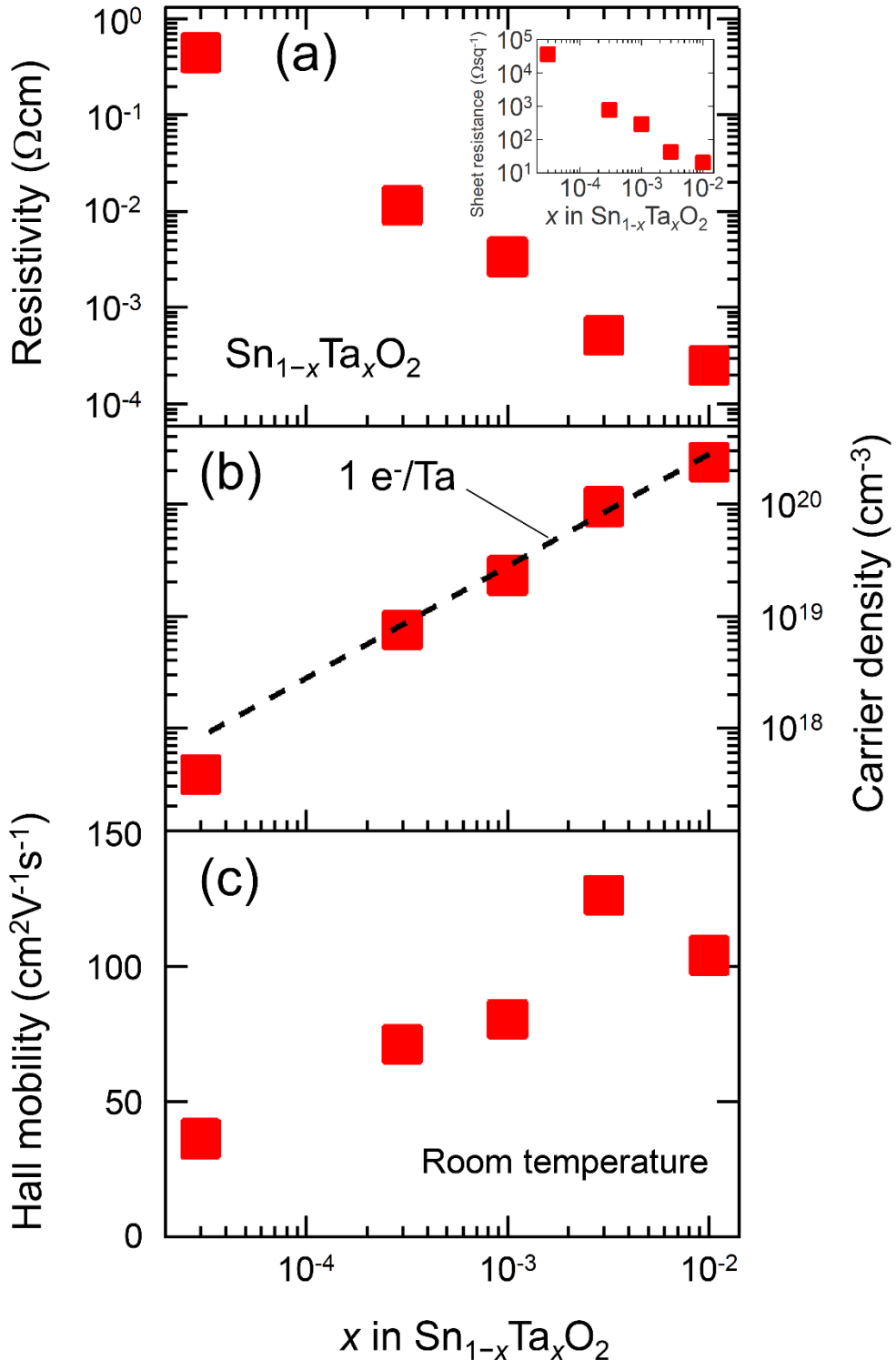

Fig. 3.4. Room temperature (a) resistivity, (b) carrier density (n_e), and (c) μ_H for the TTO films as a function of x. The inset of (a) shows sheet resistance of the films. The broken line is the expected n_e when all the doped Ta^{5+} ions substitute to the Sn^{4+} sites and generate one electron per Ta (100% doping efficiency).

unfavourable defects such as clustered dopants [44] and accepter-like defects [90]. Remarkably, μ_H dramatically increased with increasing x at $x \leq 3 \times 10^{-3}$. This behavior was rationalized by assuming an enhanced screening of dislocations [49] and/or grain boundaries [54,59] owing to the increased n_e. The TTO films with $x = 3 \times 10^{-3}$ ($n_e \sim 1 \times 10^{20}$ cm^{-3}) exhibited the highest μ_H of 126 – 131 cm^{2}V^{-1}s^{-1}, which is the highest among the μ_H values reported for undoped and doped SnO_2 films so far. Further increase in x yielded a slight decrease in μ_H, possibly owing to the manifestation of ionized impurity scattering, as will be discussed later. The lowest resistivity, 2.5×10^{-4} Ωcm, and sheet resistance, 20.2 Ωsq.$^{-1}$, were obtained for the TTO film with $x = 1 \times 10^{-2}$, as shown in Fig. 3.4 (a).

I now discuss the transport properties of the TTO films in comparison with the literature data. Figure 3.5 plots μ_H against n_e for thin films [48,49,52,59], including ours, and bulk single crystals [45,47] of SnO_2. The previously reported μ_H values for thin films were generally lower than those of bulk single crystals with similar n_e values. However, my TTO films with $n_e \sim 1 \times 10^{20}$ cm^{-3} exhibited a record-high μ_H (130 cm^{2}V^{-1}s^{-1}) for thin films, comparable to that for a bulk single crystal with a similar n_e value. Such an extremely high μ_H value suggests that the film contained a negligibly small amount of extrinsic sources of carrier scattering, such as neutral impurities, grain boundaries, and dislocations. In other words, intrinsic sources of carrier scattering, such as phonons and ionized impurities, supposedly dominated μ_H.

To test the above-mentioned hypothesis, I calculated the Hall mobility (μ_{cal}) taking only phonon and ionized impurity scattering into account, as

$$\mu_{cal}^{-1} = \mu_{lat}^{-1} + \mu_{iis}^{-1},$$

where μ_{lat} is the lattice mobility associated with phonon scattering and μ_{iis} is the Hall mobility limited by ionized impurity scattering. For μ_{lat}, I used a fixed value (260 $cm^2V^{-1}s^{-1}$) observed for undoped single crystals in the *a*-direction [45]. The μ_{iis} value was calculated by using the Brooks–Herring–Dingle (BHD) formula [18], which has been successfully used to analyze μ_{iis} for Sn-doped In_2O_3 [91], Al-doped ZnO [44,90],

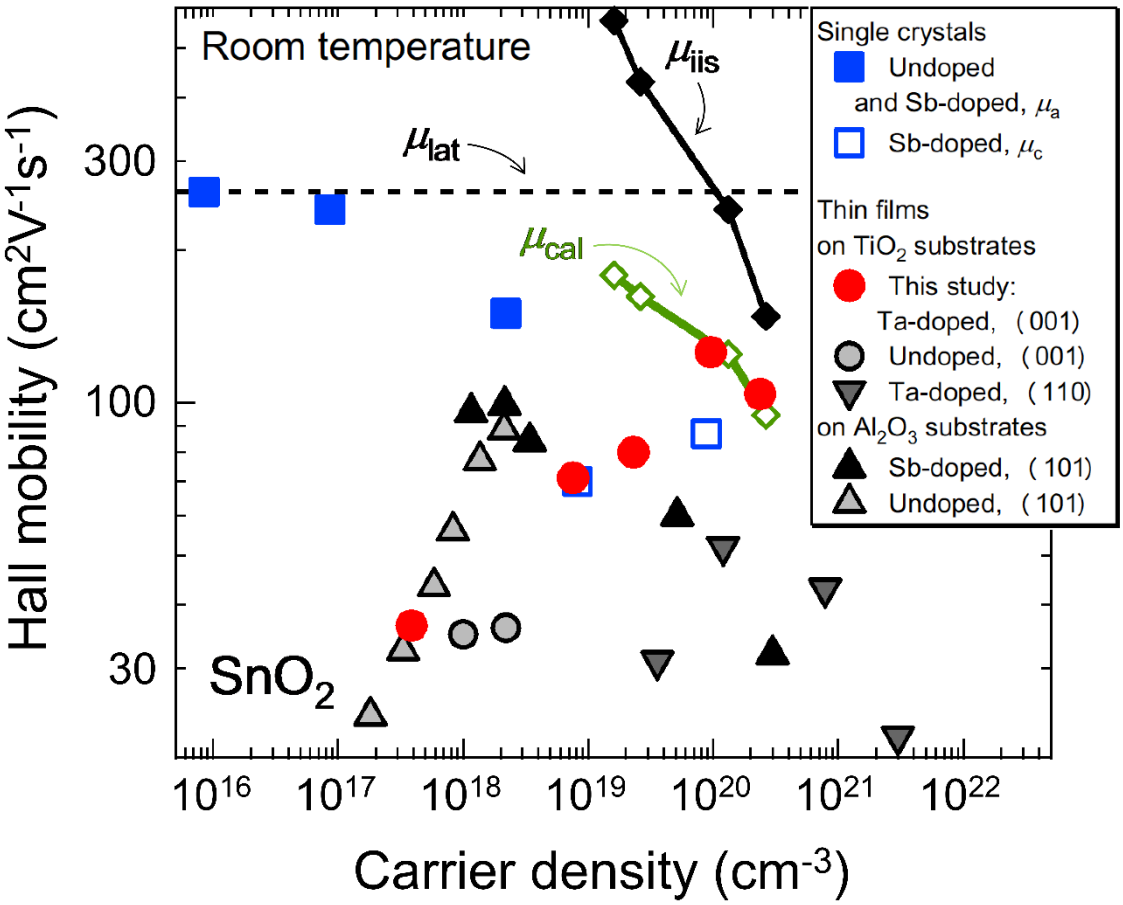

Fig. 3.5. Room temperature μ_H as a function of n_e for SnO_2 bulk single crystals (squares) and thin films [circles (present study) and triangles (literature data)]. The data for undoped single crystals in the *a*-direction (μ_a) and Sb-doped single crystals in the *c*-direction (μ_c) are from [44], [46], respectively. The data for Ta-doped (110)-, undoped (001)-, Sb-doped (101)-, and undoped (101)-films are from [58], [51], [47], and [48], respectively. A solid line with diamond symbols (μ_{cal}) represents calculated μ_H assuming that only phonon (μ_{lat}, broken line) and ionized impurity (μ_{iis}, solid line) scattering contribute to μ_H ($\mu_{cal}^{-1} = \mu_{lat}^{-1} + \mu_{iis}^{-1}$).

and Nb-doped TiO_2 [30]. The BHD formula is written as eq. (1-34).

Considering the high doping efficiency, all the doped Ta was supposed to behave as singly charged ions (Ta^{5+} substituting for Sn^{4+}). Although it was difficult to determine the valence state of Ta in TTO experimentally [92] (Fig. 3.6), theoretical calculations [43,63] reported that Ta exists in the pentavalent state (Ta^{5+}) in TTO. Thus, I assumed $Z = 1$ and $n_I = n_e$. Because the films in this study were (001)-oriented, I used $\varepsilon_{ra} = 13.5$ for ε_r [93]. For m^*, I used experimentally determined m^*_a values as a function of n_e and their linear interpolation [34]. As shown in Fig. 3.5, μ_{cal} was higher than most of the experimental data, which indicated that the suppression of μ_H arose from carrier scattering by extrinsic sources. Notably, however, the μ_H values at $n_e \geq 9 \times 10^{19}$ cm^{-3} ($x = 3 \times 10^{-3}$ and 1×10^{-2}) in the present study agreed well with μ_{cal}. This proved that in these high μ_H films, carrier scattering by neutral impurities, dislocations, and grain-boundaries was negligibly small compared with that by ionized impurities and phonons,

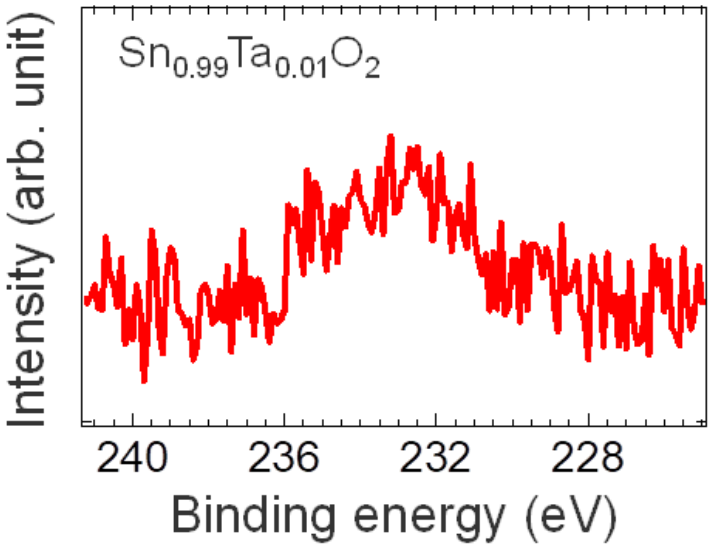

Fig. 3.6. Ta 4*d* 5/2 photoemission spectrum of TTO film with $x = 0.01$ measured by an X-ray photoemission spectrometer (JEOL, JPS-9010MC). The Ta 4*d* 5/2 emission line was too weak to determine the valence state of Ta experimentally.

and that the reduced μ_H at $n_e = 2.4 \times 10^{20}$ cm^{-3} ($x = 1 \times 10^{-2}$) was attributed to the increased ionized impurity scattering.

To discuss the carrier scattering mechanisms in more detail, I measured the temperature dependences of n_e and μ_H for the TTO films with $x = 3 \times 10^{-4} - 1 \times 10^{-2}$. As shown in Fig. 3.7 (a), the n_e values were independent of temperature, indicating that the TTO films in this study were in the degenerately-doped regime. Notably, the TTO films with $x \geq 1 \times 10^{-3}$ showed negative temperature coefficients of μ_H (Fig. 3.7 (b)) around

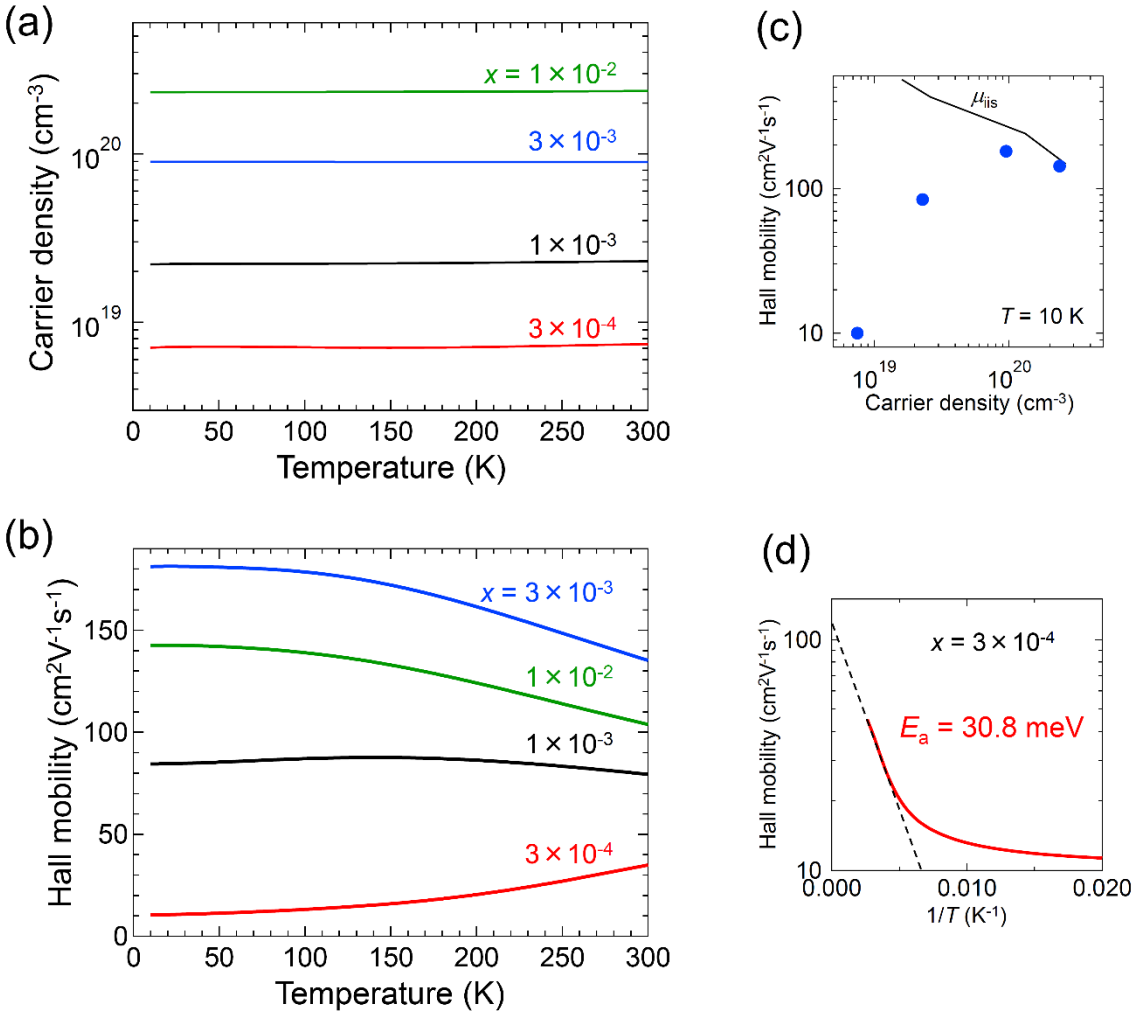

Fig. 3.7. Temperature dependence of (a) n_e and (b) μ_H for the TTO films with $x = 3 \times 10^{-4} - 1 \times 10^{-2}$. (c) μ_H at 10 K (circles) as a function of n_e, in comparison with μ_{iis} (solid line). (d) μ_H for the TTO film with $x = 3 \times 10^{-4}$ plotted against the inverse of temperature ($1/T$). The dashed line represents the least-squares fit to the Arrhenius equation, yielding an activation energy value of 30.8 meV.

room temperature, being the specific characteristic of phonon scattering. This implies that, at room temperature, the μ_H values are dominated by phonon scattering, consistent with the arguments based on the room temperature data (Fig. 3.5). At low temperature, phonon scattering is suppressed [45], and ionized impurities are supposed to be the intrinsic sources of carrier scattering. Remarkably, as shown in Fig. 3.7 (c), μ_H at 10 K for the TTO film with $x = 1 \times 10^{-2}$ ($n_e = 2.4 \times 10^{20}$ cm^{-3}) agrees well with μ_{iis}, which is known to be temperature-independent in the degenerately-doped regime. This result supports the conclusion that μ_H of the film is dominated by ionized impurity scattering and phonon scattering at room temperature (Fig. 3.5). As x and thus n_e decreased, μ_H at 10 K started deviating downward from μ_{iis}. This behaviour indicates that the TTO films with $x < 1 \times 10^{-2}$ contain extrinsic sources of carrier scattering, pronounced especially at low temperature. Thermal-activation-type behaviour of μ_H was observed for the TTO film with $x = 3 \times 10^{-4}$ (Fig. 3.7(d)), demonstrating that μ_H is governed by grain boundary scattering [94] in the film, although grain-boundary scattering in SnO_2 epitaxial films has scarcely been studied so far. Dominguez *et al.* proposed that {101} crystallographic shear planes (CSPs) in SnO_2 films, which are induced by misfit dislocations [95], may act like grain boundaries [54]. Similarly, I speculated that the carrier scattering at {101} CSPs was responsible for the lower μ_H than μ_{cal} at $n_e < 9 \times 10^{19}$ cm^{-3}.

Judging from the complete screening by free carriers at $n_e \geq 9 \times 10^{19}$ cm^{-3}, the CSP-based grain-boundary scattering in the TTO films was supposed to be weak. I considered that lattice matching and growth orientation play an essential role in the CSP-based grain-boundary scattering as follows. Owing to the good lattice-matching to SnO_2, the TiO_2 (001) substrate would induce lower densities of misfit dislocations and thus

CSPs in the films than other substrates [54,95]. Furthermore, the angle between {101} CSPs and the basal plane of the SnO_2 (001) film was approximately 34°, as shown in Fig. 3.8 (a). The shallow angle would cause termination of the {101} CSPs at the crossing point with complementary {101} CSPs [95] at the early stage of the film growth. Indeed, as shown in Fig. 3.8 (b), cross-sectional TEM observations revealed that the TTO films on the TiO_2 substrate had lower densities of CSPs than those on other substrates [54,95] and that the CSPs did not reach the film surface, which supported the above-mentioned scenario. These structural characteristics can account for the lower contribution of carrier scattering at the CSP-based grain boundaries to the carrier transport in the TTO films on TiO_2 (001). However, SnO_2 epitaxial films on other substrates than TiO_2 (001) have reportedly shown highly populated {101} CSPs inclined steeply to the basal planes [54,95], as schematically illustrated in Fig. 3.8 (a). The CSPs in SnO_2 epitaxial films are induced by misfit dislocations, and they are not energetically favorable in a bulk

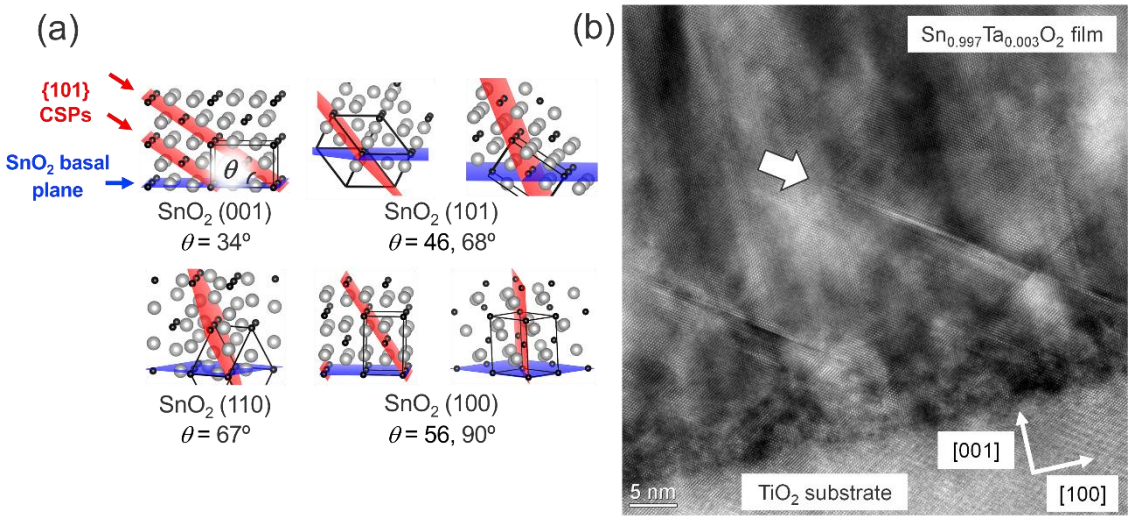

Fig. 3.8. (a) Schematics of {101} planes, at which crystallographic shear planes (CSPs) are formed, against SnO_2 basal planes with (001), (101), (110), and (100) orientation using the VESTA program [145]. θ denotes the angle between {101} and each SnO_2 basal plane. (b) Cross-sectional transmission electron microscopy image of a TTO film with $x = 3 \times 10^{-3}$. The incident electron beam was parallel to the [010] direction. The arrow in the film indicates {101} CSP.

crystal, unlike the CSPs induced by off-stoichiometry, as seen in oxygen-deficient rutile TiO_2 crystals [96]. Therefore, the density of CSPs decreased as the film thickness increases [54]. Nevertheless, some of the CSPs in those films survived even near the surface of the films [54]. These results suggest that the CSP-based grain-boundary scattering is more significant in the SnO_2 epitaxial films on other substrates than TiO_2 (001), which can account for the lower μ_H than those for the TTO films on TiO_2 (001), as depicted in Fig. 3.5.

To verify the proposed model, I investigated film thickness and growth orientation dependence of μ_H for TTO films with $x = 3 \times 10^{-3}$ grown on various substrates [14–23,25–29,41,43,44], (001)-, (101)-, and (110)-planes of TiO_2, and m-, r-, and c-planes of Al_2O_3 substrates (Fig. 3.9). Figure 3.10 plots room temperature n_e and μ_H for the TTO films with various film orientations as a function of the film thickness. With increasing

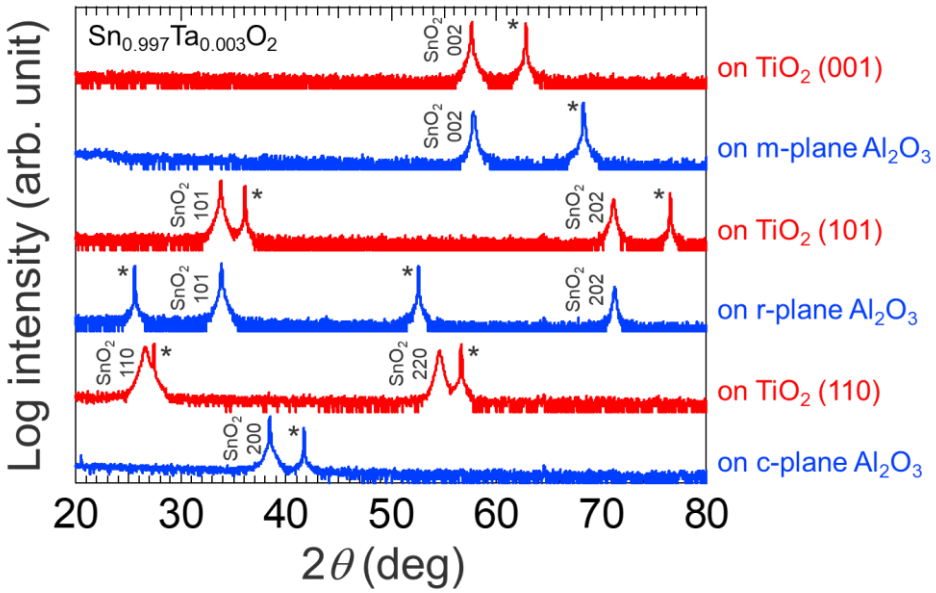

Fig. 3.9. ω-2θ X-ray diffraction patterns for 300-nm-thick TTO films with $x = 3 \times 10^{-3}$ grown on various substrates. The asterisk symbols denote substrate peaks.

film thickness, the μ_H values increased probably owing to the synergistic effect of enlarged crystalline grains [99,100] and reduced density of threading dislocations [25] and {101} CSPs [54,95]. The highest μ_H was achieved for the (001)-oriented TTO films, followed in order by the (101)-, the (110)-, and the (100)-oriented ones. This behaviour can be explained by the CSP-based grain-boundary scattering because the angle between the CSP and the basal planes of the films becomes small in the same order (Fig. 3.8 (a)). Notably, the TTO films with the same orientation showed similar μ_H values even though different kinds of substrates were used. The orientation dependence of μ_H cannot be

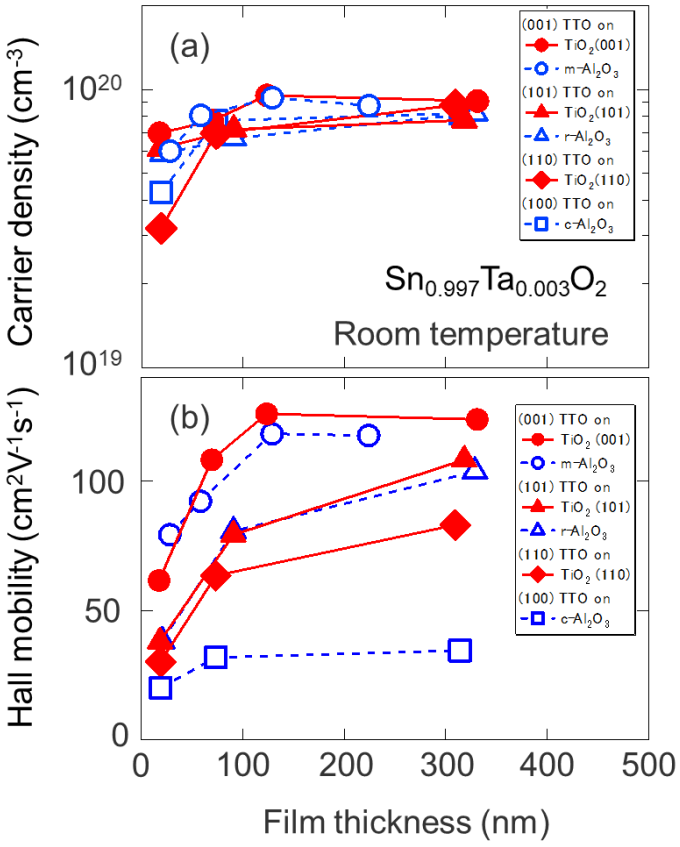

Fig. 3.10. Film thickness dependence of room temperature (a) n_e and (b) μ_H for the TTO films with (001) (circles), (101) (triangles), (110) (diamonds), and (100) (squares) orientations grown on TiO_2 (closed symbols) and Al_2O_3 (open symbols) substrates.

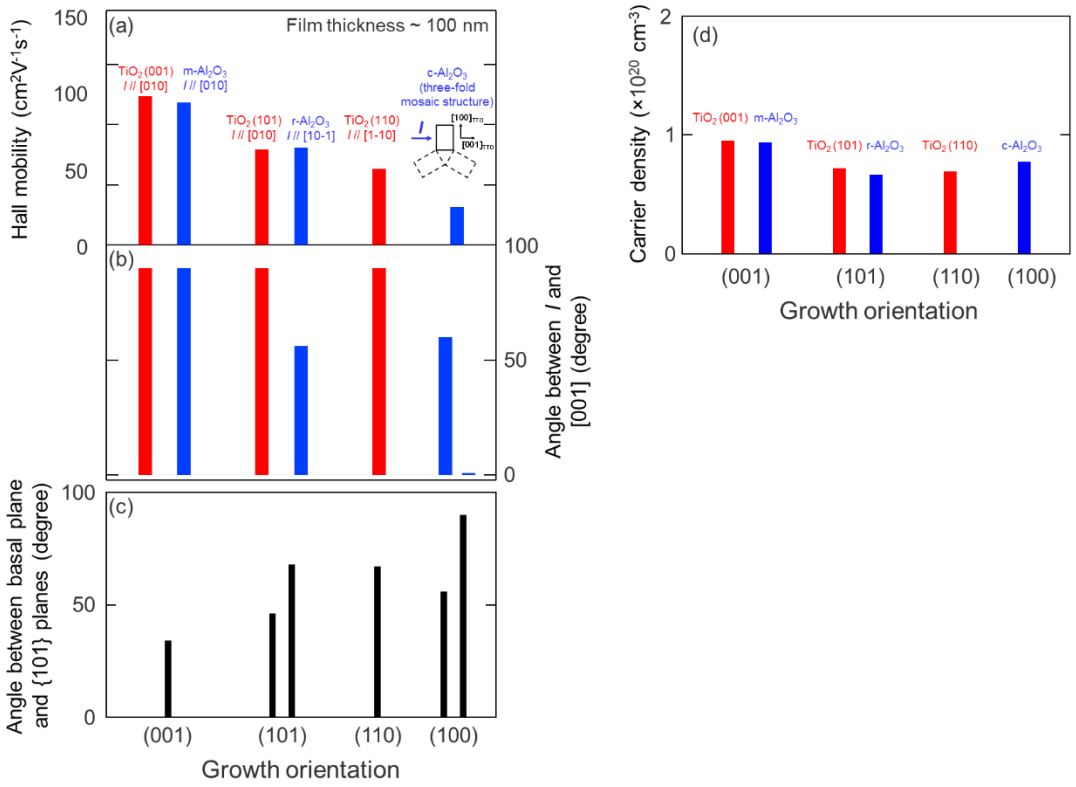

Fig. 3.11. (a) Hall mobility, (b) angle between the current direction (I) and [001], (c) angle between basal plane and {101} planes, and (d) carrier density of $Sn_{1-x}Ta_xO_2$ (TTO) epitaxial films with various growth orientation. Inset of (a) denotes the I and in-plane orientation of the three domains in the TTO film grown on c-Al_2O_3.

explained by the anisotropy in the electron effective mass of SnO_2 (Fig. 3.11). It was suggested that {101} CSPs play a significant role in the carrier transport in the TTO epitaxial thin films.

3.4 Conclusion

I investigated the transport properties of $Sn_{1-x}Ta_xO_2$ (TTO) films with $x = 3 \times 10^{-5}$–1×10^{-2} epitaxially grown on TiO_2 (001) substrates. The n_e values for the TTO films were almost equal to the concentrations of Ta dopants, which demonstrated the very high

doping efficiency of Ta. The μ_H values of the TTO films with $n_e \geq 9 \times 10^{19}$ cm^{-3} ($x \geq 3 \times 10^{-3}$) agreed well with the intrinsic limit of μ_H, assuming that only phonon and ionized impurities contributed to carrier scatterings. Negligible contribution of the grain-boundary scattering to μ_H might arise from a reduced density of CSPs. The TTO films with $n_e \sim 1 \times 10^{20}$ cm^{-3} ($x = 3 \times 10^{-3}$) exhibited a very high μ_H of 130 cm^{2}V^{-1}s^{-1}, which is the highest among SnO_2 films thus far reported. The μ_H values for the TTO ($x < 3 \times 10^{-3}$) films rapidly decreased with a decrease of x, which suggested a weakened screening of dislocation and/or grain-boundary scatterings owing to the decreased n_e.

Chapter 4

Carrier generation mechanism in W-doped SnO_2 epitaxial films with high mobility

本章については、5 年以内に雑誌等で刊行予定のため、非公開。

Chapter 5

Fabrication of P-doped SnO_2 thin films by pulsed laser deposition

本章については、5 年以内に雑誌等で刊行予定のため、非公開。

Chapter 6

Fabrication of textured SnO_2 transparent conductive films using self-assembled Sn nanospheres *

6.1 Introduction

Conversion efficiencies of photovoltaics (PVs) are markedly influenced by the transparent conductive oxide (TCO) layers used as electrodes [105–113]. Important properties of TCOs for these purposes include conductivity, transparency, work function, durability to processing, and surface morphology [105,106]. In particular, textured surfaces of TCOs are highly desirable for thin-film Si PVs to compensate for the low absorption coefficients of the active layers [107,108,110,111]. The compensation is achieved by providing an elongated optical path of incident light scattered at the textured surface of TCOs. In addition, the texture of TCOs reduces the reflectance losses of light

* This chapter contains the contents of the following publications.

M. Fukumoto, S. Nakao, Y. Hirose and T. Hasegawa, Jpn. J. Appl. Phys. **57**, 060307 (2018).

at the interface between the TCOs and active layers. Light trapping technologies in TCOs developed to date have contributed to improved conversion efficiencies in PVs.

The fabrication of textured surfaces, which critically determine surface morphologies of TCOs, can be classified into the following three types. The first method is to use as-deposited TCO surfaces [105,114–119]. In particular, SnO_2:F grown by chemical vapor deposition (CVD) [114–116] has been extensively studied for practical purposes, leading to commercial products. The surface morphology of TCOs fabricated by this method includes pyramidal features owing to the faceted nature of the surface. A cauliflower-like morphology, which is described as double-textured, has also been achieved with the use of state-of-the-art deposition methods, although details of the deposition have not been reported [116]. A second approach involves the etching of TCO layers [105,120–122]. This method has been widely studied on sputtered ZnO:Al, yielding craterlike morphologies, which are more suitable than pyramidal ones for applications to PVs. Disadvantages of this method include its limited applicability (applicable only to easily etchable TCOs), the necessity for thick as-deposited films, and complicated controllability depending not only on the etching but also on the film growth. A third approach is to process the substrates by top-down (i.e., lithography or nanoimprinting) [123–126] or bottom-up (i.e., deposition of nanostructured templates) [127–131] techniques. These methods can be applied to any kind of TCO material deposited by various techniques. Furthermore, this method allows us to fabricate various morphologies, such as double-textured [123,125] and pillar [132] features, in a controlled manner. However, this method requires further processing equipment in addition to that used for TCO deposition, which is thus less productive and scalable than the aforementioned methods.

In this chapter, I propose the fabrication of textured transparent conductive SnO_2 films by processing substrates with a bottom-up technique. I used self-assembled nanospheres of SnO_2 as nanostructured templates. This template approach is potentially more productive and scalable than alternative methods because the template can be fabricated in the same sputtering chamber used to deposit TCO layers.

6.2 Method

Figure 6.1 shows schematics of the proposed method for the fabrication of the textured SnO_2 films. A key point of this method is the use of aggregated Sn as a template for a textured surface. Metallic Sn has a low melting point (231.9 °C) together with a low vapor pressure above its melting point. Moreover, glass surfaces show poor wettability with respect to molten Sn. Therefore, metallic Sn films on glass substrates aggregate when heated above the melting point of Sn, resulting in self-assembled nanospheres of Sn [133,134]. The presently proposed method consists of four steps, specifically three steps (Figs. 6.1 (a)–6.1 (c)) to prepare the nanostructured templates and one step for deposition of TCO layers on the templates (Fig. 6.1 (d)). The nanostructured templates were prepared as follows. First, 25-nm-thick Sn films were deposited on unheated alkaline-free glass substrates by DC magnetron sputtering (Sanyu Electron SC-701HMCII) equipped with a molecular drag pump (Fig. 6.1 (a)). A metallic Sn disk (99.9% purity) was used as a sputtering target. Second, the as-deposited precursor films were annealed in H_2 ambient at 600 °C for 1 min in a rapid thermal annealing furnace (Fig. 6.1 (b)). This step yielded self-assembled Sn nanospheres. Third, the Sn nanospheres

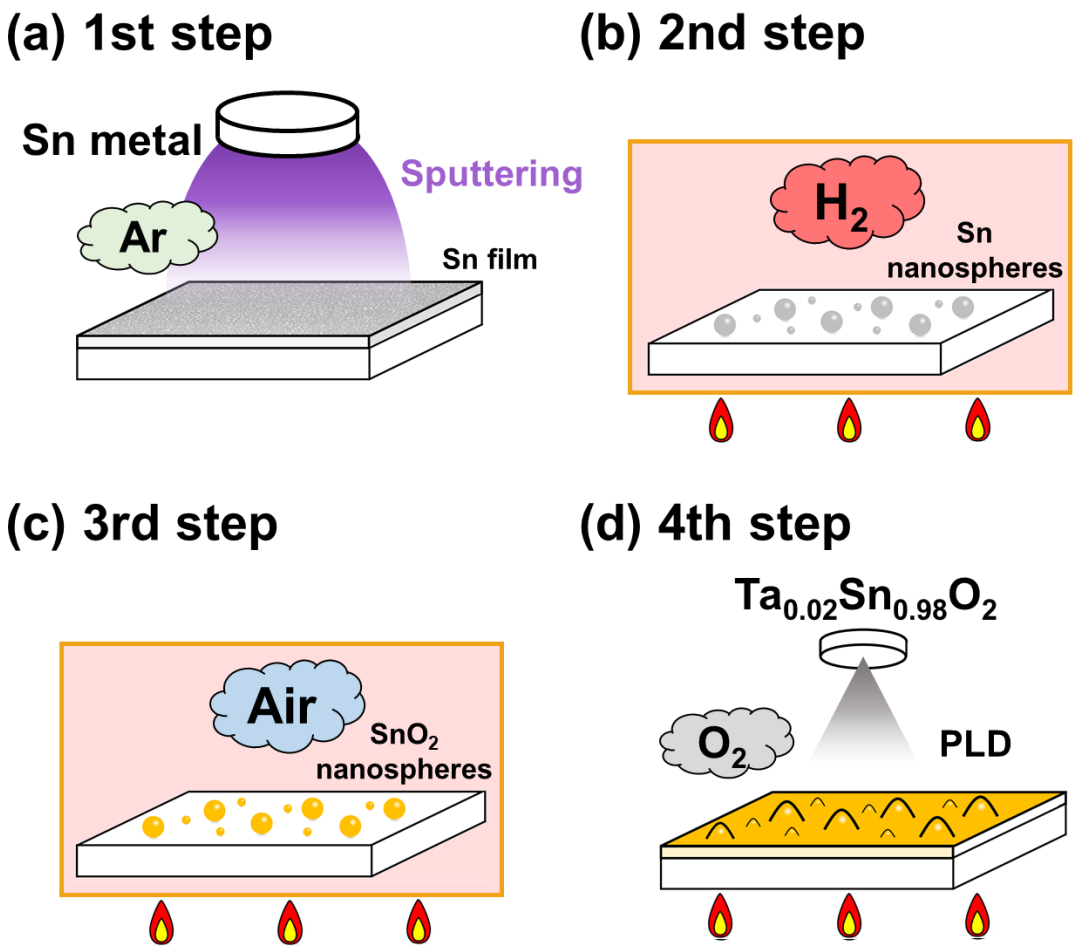

Fig. 6.1. Schematic illustrations of the proposed method consisting of (a) deposition of precursor Sn films on glass substrates (first step), (b) formation of self-assembled Sn nanospheres with reductive annealing (second step), (c) conversion of the spherical Sn into SnO_2 with oxidative annealing (third step), and (d) conformal deposition of transparent conductive TTO layers on the self-assembled spherical SnO_2 templates (fourth step).

were converted into oxide templates by annealing in air at 600 °C for 1 h (Fig. 6.1 (c)). Finally, the nanostructured templates were conformally coated with transparent conductive SnO_2 layers (Fig. 6.1 (d)). In this proof-of-concept demonstration, I used pulsed laser deposition (PLD) instead of sputtering for simplicity. A ceramic pellet of SnO_2:Ta ($Sn_{0.98}Ta_{0.02}O_2$, TTO) was used as a PLD target. Substrate temperature and oxygen partial pressure during the film growth were 550 °C and 1×10^{-2} Torr, respectively. Details of the film growth have been described elsewhere [58,102]. The thickness of the

TTO layer measured with a stylus profiler was 740 nm. I measured the height difference between the TTO layer and the template that was masked during TTO deposition. The height difference was defined as the TTO layer thickness. Although this value contains large uncertainties due to the rough surfaces of the TTO layers and the templates, cross-sectional observations (shown later) yielded similar values.

Crystal structures and surface morphologies of the samples were characterized by X-ray diffraction (XRD) and scanning electron microscopy (SEM), respectively. Total transmittance (T_{tot}) and diffuse transmittance (T_{dif}) were evaluated with a UV/visible/near-infrared spectrophotometer equipped with an integrating sphere. Haze values, a measure of the light-trapping ability, were calculated as T_{dif}/T_{tot}. Electrical transport properties, including sheet resistance (R_s), resistivity, carrier density, and Hall mobility, were measured by the van der Pauw method.

6.3 Results and discussion

We first characterized the structural properties of the samples. Figures 6.2 and 6.3 show SEM images and XRD patterns, respectively, of the sample observed after each step. In the first step (precursor deposition), a polycrystalline β-Sn thin film composed of small grains (~25 nm) was obtained, as shown in Fig. 6.2 (a). Similar to previous studies based on vacuum evaporation [133,134], the sample in the second step (reductive annealing above the melting point) was covered with self-assembled nanospheres of Sn (Fig. 6.2 (b)). Relatively large nanospheres with a diameter of approximately 100–200 nm were sparsely distributed and tiny nanospheres filled in the space between the large

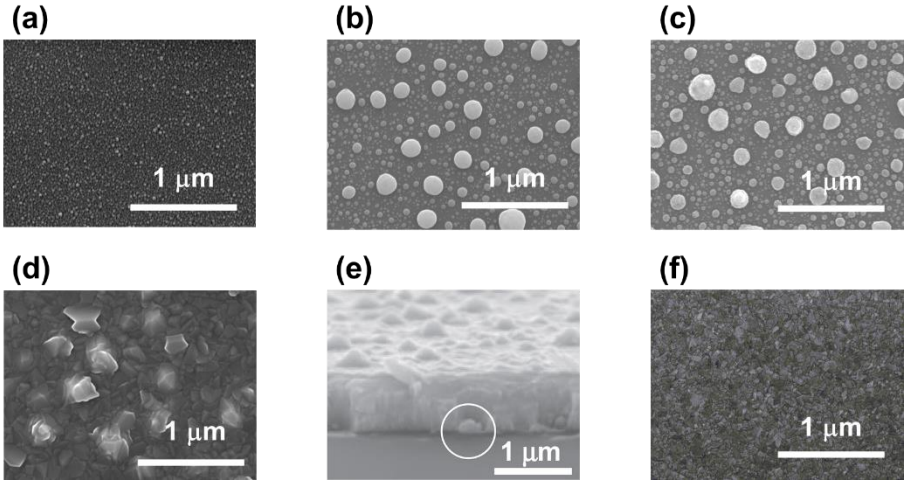

Fig. 6.2. Plane-view SEM images of the sample after each step of the proposed method, (a) precursor Sn films (first step), (b) Sn nanospheres (second step), (c) oxidized nanospheres (third step), and (d) conformally deposited TTO layer on the template (fourth step). (e) Cross-sectional SEM image of the TTO on the template. A circle in (e) indicates a nanosphere near glass substrate. (f) Plane-view SEM image of reference sample (TTO grown on bare glass substrates without template).

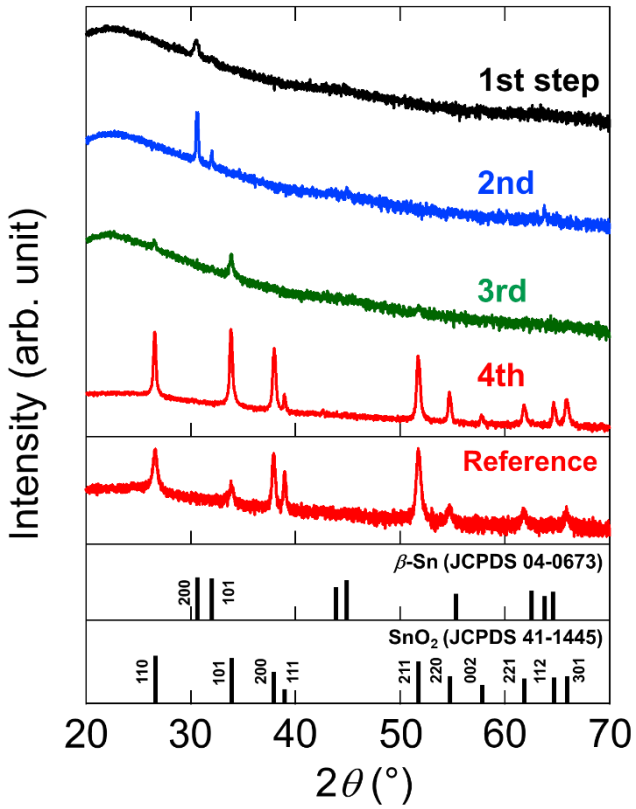

Fig. 6.3. XRD patterns of the sample after each step and reference TTO grown without the template. Bar charts show the XRD patterns of bulk SnO_2 (JCPDS 41-1445) and bulk Sn (JCPDS 04-0673).

spheres. Although I did not optimize the fabrication process of the Sn nanospheres in this study, the size of spheres could potentially be more precisely controlled by selecting appropriate experimental conditions, such as film thickness, surface treatment, and annealing parameters [133]. The surface morphology formed by the Sn nanospheres was well-preserved even after the third step of oxidative annealing, as shown in Fig. 6.2 (c). XRD measurements revealed that the oxidative annealing completely converted β-Sn into SnO_2 (Fig. 6.3). We hereafter refer to the nanostructured templates composed of the self-assembled nanospheres of SnO_2 as SNS templates. As shown in Fig. 6.2 (d), TTO deposited on the SNS template (TTO/SNS) in the fourth step exhibited a textured surface characterized by grain structure of TTO layers superimposed on the morphology of the SNS templates. Cross-sectional observations (Fig. 6.2 (e)) on cleaved samples revealed that the TTO/SNS had a dense internal structure. Generally, SnO_2 films grown by physical vapor deposition such as sputtering and PLD exhibit flat surfaces. Indeed, TTO grown on bare glass substrates without the SNS template (TTO/glass) showed a flat surface with fine grains, as shown in Fig. 6.2 (f). To our knowledge, this study presents the first report of a textured SnO_2 film grown by a method other than CVD.

As a result of the textured surface morphology, the TTO/SNS showed improved light trapping ability. Figure 6.4 compares the optical properties of TTO/SNS and the TTO/glass. Both samples exhibited a high T_{tot} of approximately 70% in the wavelength region of 400–1200 nm, which meets the requirements for transparent electrodes in PVs. The haze value of the TTO/glass was almost zero, which was consistent with the flat surface morphology. On the other hand, TTO/SNS showed a considerably higher haze value than that of TTO/glass owing to its textured surface morphology. At present, the haze value of the TTO/SNS was lower than those of commercial TCOs [105]. However,

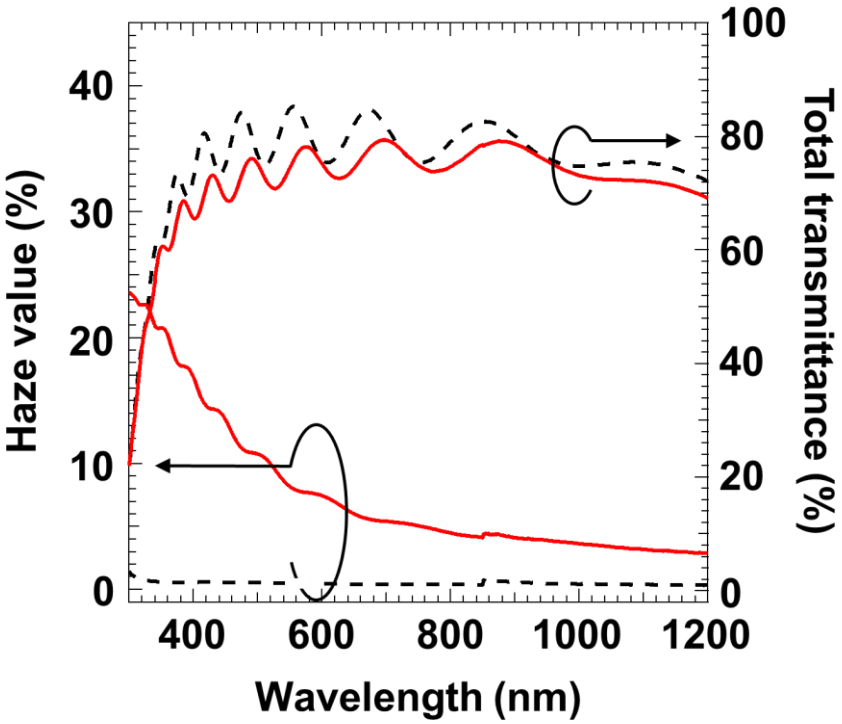

Fig. 6.4. Total transmittance and haze values of TTO films with (solid lines) and without the templates (dashed lines).

further improvements in the haze value might be expected by increasing the diameter of the Sn nanospheres, which is basically determined by the thickness of the precursor Sn films [133]. The use of hemispherical nanospheres [133] might be beneficial for suppressing possible voids formed between nanospheres and substrates. Moreover, additional control of the surface morphology might be possible by modifying the experimental conditions for oxidization of the Sn nanospheres [135] and deposition of the TCO layers [122]. Multiple-step fabrication of the texture might pave the way for a double-textured surface [116,123,125], and shows great promise for next-generation PVs that harness near-infrared light.

Next, I discuss the effects of the SNS templates on the electrical properties of the TTO layers grown on the templates. Table 6.1 summarizes R_s values and thicknesses of TTO/SNS and TTO/glass. The R_s value for TTO/SNS, 5.2 $\Omega sq.^{-1}$, was sufficiently low

Table. 6.1. Electrical transport properties of SnO_2:Ta (TTO) thin films with and without the templates.

Sample	Thickness (nm)	Sheet resistance ($\Omega sq.^{-1}$)	Resistivity (Ωcm)	Carrier density (cm^{-3})	Hall mobility ($cm^2V^{-1}s^{-1}$)
Without the template (TTO / glass)	670	12	8.2×10^{-4}	4.2×10^{20}	18
With the template (TTO / SNS)	740	5.2	3.8×10^{-4}	4.4×10^{20}	37

for application to PVs. Interestingly, the R_s value was approximately half that of TTO/glass with a similar layer thickness owing to doubled mobility. A previous study showed that crystalline templates (seed layers) enlarge the grain size of TTO grown on them and thus enhanced the mobility and conductivity of TTO [58,102]. Similarly, the SNS templates enhanced the conductivity of the TTO layers owing to the enlarged grain size; most of the grains of TTO/SNS were larger than 100 nm (Fig. 6.2 (d)), whereas the grain size of TTO/glass was less than 100 nm (Fig. 6.2 (e)). Similar enhanced conductivity on nanostructured templates has been previously reported [131].

At present, our method is complicated and thus less productive. I used two deposition methods (i.e., sputtering and PLD) and additional annealing equipment. However, I believe that the method could be more productive if reactive sputtering was applied with metallic targets, such as sintered Sn:Ta [136] and alloyed Sn:Sb [137]. In this case, both the SNS templates and the TCO layers could be fabricated with the use of only one chamber for reactive sputtering with one metallic target. Furthermore, I expect that the two annealing steps for the fabrication of SNS templates could be performed in the sputtering chamber, and thus no annealing furnace would be necessary. These annealing steps could be combined with the procedures for the TCO deposition. For example, substrate heating prior to the TCO deposition could sufficiently aggregate the Sn films. The oxygen introduced for reactive sputtering could oxidize the Sn nanospheres

as well as the target surface. The textured SnO_2 might then be obtained by adding only one step, i.e., deposition of the Sn films on unheated substrates, to usual TCO deposition.

6.4 Conclusion

In conclusion, I propose a novel method of fabricating transparent conductive SnO_2 films with textured surfaces by processing substrates with a bottom-up technique. Substrate processing consists of three steps: deposition of precursor Sn films on glass substrates, the formation of self-assembled Sn nanospheres with reductive annealing, and conversion of Sn to SnO_2 with oxidative annealing. SnO_2 films conformally deposited on the templated substrates feature textured surfaces, resulting in enhanced haze values. In addition, the templates acted as seed layers and thus promoted grain growth, which contributed to increased conductivity in the TTO layers. These optical and electrical properties show promise for the use of the substrates as transparent electrodes in PVs. The proposed method could be highly productive and scalable provided that the method can be adapted to reactive sputtering with metallic targets.

Chapter 7

Experimental evidence of wide bandgap in triclinic (001)-oriented $Sn_5O_2(PO_4)_2$ thin films on Y_2O_3 buffered glass substrates *

7.1 Introduction

As described in Chapter 1, the lack of *p*-type TCOs limits the realization of advanced active junction-based devices. $Sn_5O_2(PO_4)_2$ is a promising parent material as a *p*-type TCO with high μ_H [74]. For optoelectronic applications, high-quality thin films of TCOs are required. However, thin-film growth of triclinic $Sn_5O_2(PO_4)_2$ is difficult due to the lack of suitable lattice-matched single-crystalline substrates. Glass substrates are a common alternative, which is suitable in general for large area deposition. The competition of various series of tin(II) phosphates usually leads to impurity phases in $Sn_5O_2(PO_4)_2$. So far, $Sn_5O_2(PO_4)_2$ has been synthesized only in powder form, and its

* This chapter contains the contents of the following publications.

M. Fukumoto, C. Yang, W. Yu, C. Patzig, T. Höche, T. Ruf, R. Denecke, M. Lorenz and M. Grundmann, J. Mater. Chem. C **8**, 14203 (2020).

fundamental physical properties have not been investigated experimentally [73]. In this study, I demonstrated the growth of phase-pure $Sn_5O_2(PO_4)_2$ thin films for the first time. Control of the crystal orientation in the PLD process was achieved by means of structure-directing Y_2O_3 buffer layers. The obtained high-quality thin films allow for the experimental study of the optical band gap of $Sn_5O_2(PO_4)_2$ [138].

7.2 Method

The $Sn_5O_2(PO_4)_2/Y_2O_3$ layer system and the reference Y_2O_3 sample were deposited by PLD using a KrF excimer laser (λ = 248 nm) [139]. A ceramic Y_2O_3 target was sintered from Y_2O_3 powder (99.99% purity, Aldrich Chemie) at 1700 ºC for 12 h in air. A pulsed laser beam was focused on the Y_2O_3 target at a repetition rate of 10 Hz. Y_2O_3 buffer layers with a thickness of 110 nm were deposited at 790 ºC on fused silica glass at an oxygen partial pressure of 2.5×10^{-3} mbar. $Sn_5O_2(PO_4)_2$ thin films were subsequently grown on the Y_2O_3 layers by ablating a $Sn_2P_2O_7$ target, which was sintered from $Sn_2(P_2O_7)$ powder (95.0% purity, Alfa Aesar) at 400 ºC for 10 h in air. 300 nm thick $Sn_5O_2(PO_4)_2$ films were deposited at temperatures in the range 535−595 ºC with a base pressure of 1.2×10^{-6} mbar. For $Sn_5O_2(PO_4)_2$ growth, the laser pulse frequency was 5 Hz, and the laser energy density on the target was approximately 2 $J \cdot cm^{-2}$. I used a phosphorus-rich $Sn_2P_2O_7$ target compared to the resulting $Sn_5O_2(PO_4)_2$ films in order to compensate for phosphorus loss due to the (re-)evaporation of phosphorus from the films during PLD. Crystal structure and crystalline quality were evaluated by X-ray diffraction (XRD) using Cu $K\alpha$ radiation from a parabolic mirror in a PANalytical X'Pert Pro MRD

system with a PIXcel^{3D} detector.

Cross-sectional (scanning) transmission electron microscopy ((S)TEM, ThermoFisher FEI Titan^3 80−300) was performed to investigate the microstructural morphology of the thin films. In addition to that, the chemical composition and element distribution within the thin films were evaluated by energy-dispersive X-ray spectroscopy in the same (S)TEM setup with nm resolution (SuperX-EDX Detector, ThermoFisher FEI). A standard-free quantification of the thin film composition was done by an evaluation of the intensities of the Sn-*L*, P-*K*, and O-*K* X-ray intensities using the software Esprit 1.9 (Bruker) and based on the Cliff-Lorimer factors provided within the software. The sample preparation for (S)TEM in order to obtain electron-transparent thin films was done using a mechanical wedge-polishing approach: After face-to-face gluing of two sample surfaces versus each other, a thin wedge was mechanically polished with a dedicated polishing system (MultiPrep, Allied High Tech Products) into the sample, such that the interface region turned very thin (< 1 μm thickness). Final thinning to electron transparency, alongside sample cleaning, was done by low-energy Ar^+ ion beam milling (Precision Ion Polishing System PIPS, Gatan Inc.).

The elemental composition of the obtained films was also determined by X-ray photoelectron spectroscopy. Experiments were performed with a VG ESCAlab 220 iXL spectrometer using Al $K\alpha$ excitation. The measurements were performed at UHV conditions with a base pressure of 5×10^{-9} mbar. The C 1s peak of carbonaceous contaminants, located at 285 eV, was used as binding energy reference for the energy scale calibration to compensate charging [140]. Iterative curve fitting, including the spectral Shirley background as well as Voigt profiles obtained by convolution of Gaussian and Lorentzian functions for the Sn 3*d*, P 2*s*, P 2*p*, and O 1*s* core-level spectra, was

performed using the UNIFIT software [141].

The optical absorption coefficient α of each layer was calculated by the following equation using the thickness of each layer (t) and transmittance (T) measured with a UV-visible-NIR spectrometer.

$$\alpha = \frac{1}{t} \ln \frac{1}{T}$$

7.3 Results and discussion

Figure 7.1 (a) shows θ–2θ XRD patterns of the $Sn_5O_2(PO_4)_2$ films with and without Y_2O_3 buffer layer prepared at substrate temperature (T_s) of 565 ºC. For the sample directly grown on a bare glass substrate, diffractions peaks of a mixture of the tin(II) phosphates were observed. In particular, besides the desired $Sn_5O_2(PO_4)_2$ phase, impurity phases mainly composed of $Sn_4O(PO_4)_2$ are present. This growth behavior is related to

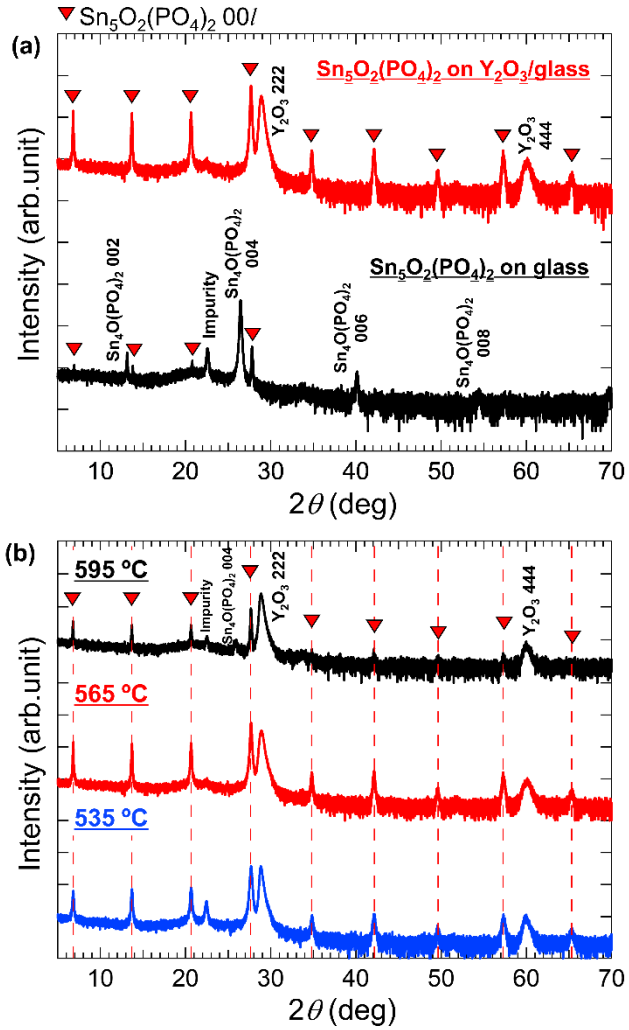

Fig. 7.1. (a) θ–2θ XRD patterns of $Sn_5O_2(PO_4)_2$ films with and without Y_2O_3 buffer layers grown at 565 °C. (b) θ–2θ XRD patterns of $Sn_5O_2(PO_4)_2$ films on Y_2O_3/glass grown at various T_s. Closed triangles represent (00l) diffraction peaks of $Sn_5O_2(PO_4)_2$. Dashed red lines show nominal (00l) peak positions of $Sn_5O_2(PO_4)_2$ based on powder diffraction pattern of $Sn_5O_2(PO_4)_2$ (JCPDS no. 01-077-5722).

the difficulty of precise control of the chemical film composition and the lack of structural phase stabilization by a crystalline template. The evaporation of phosphorus from the films during deposition leads to a competition of the formation of various tin(II) phosphates. Moreover, the amorphous glass substrate denied the selective growth of $Sn_5O_2(PO_4)_2$. To solve these problems, in addition to using a phosphorus-rich target, we introduced a (111)-oriented Y_2O_3 buffer layer on the amorphous glass substrate [142], considering the in-plane structural similarity between $Sn_5O_2(PO_4)_2$ (001) and Y_2O_3 (111) and the dissimilarity between $Sn_4O(PO_4)_2$ (001) and Y_2O_3 (111). As a result, I succeeded in obtaining phase-pure $Sn_5O_2(PO_4)_2$ thin films, as shown in Fig. 7.1 (a). The lattice spacing calculated from the (001) diffraction peak is d = 1.30 nm. It is worth to note that the use of other single-crystalline substrate materials such as r-plane Al_2O_3, YSZ (111), Y_2O_3 (111)/YSZ (111), $SrTiO_3$ (111), and Si (111) always led to the existence of the impurity phases as shown in Fig. 7.2. These results indicate that the presence of the (111)-oriented Y_2O_3 buffer layer is essential for the selective growth of triclinic $Sn_5O_2(PO_4)_2$.

Moreover, (00*l*) diffraction peaks from $Sn_5O_2(PO_4)_2$ and (*hhh*) diffraction peaks from Y_2O_3 can be clearly observed in the film sample with the Y_2O_3 buffer layer. This result indicates that the orientation-controlled growth of $Sn_5O_2(PO_4)_2$ films was achieved simply by using an out-of-plane oriented Y_2O_3 buffer layer, even on the amorphous substrate. Hence, I expect that this approach is feasible to further control and improve the orientation of $Sn_5O_2(PO_4)_2$ thin films by optimizing the structure of the Y_2O_3 buffer layer.

Subsequently, the substrate temperature T_s was optimized to carefully adjust the required phosphorus loss from the $Sn_2P_2O_7$ target towards the envisaged thin-film

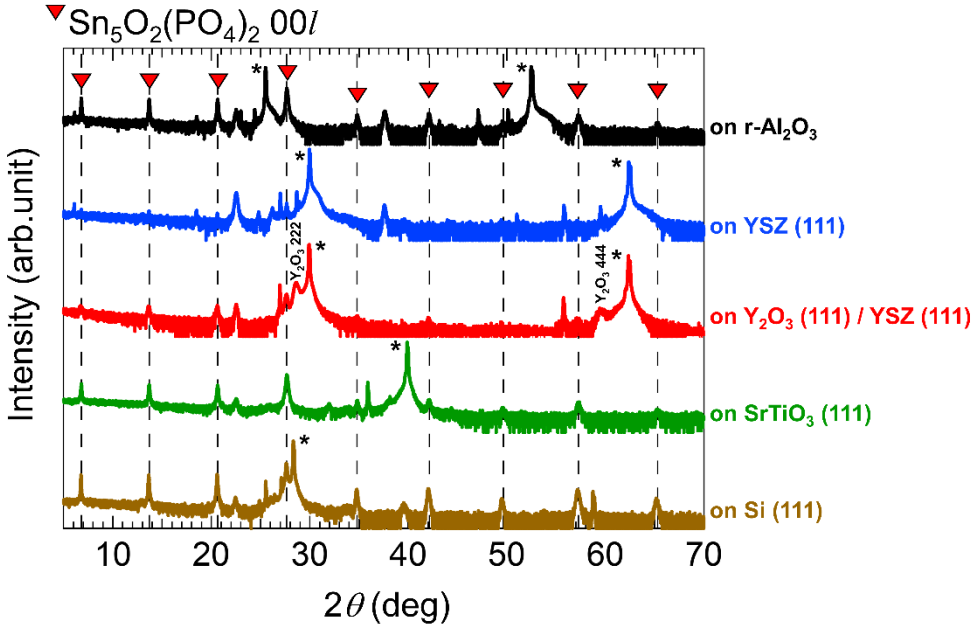

Fig. 7.2. θ–2θ XRD pattern of $Sn_5O_2(PO_4)_2$ films grown at 565 °C on various substrates. The asterisks indicate substrate peaks.

material $Sn_5O_2(PO_4)_2$. I found that there is only a small window of possible T_s manipulation to obtain phase-pure $Sn_5O_2(PO_4)_2$. For illustration, the θ–2θ XRD patterns for the $Sn_5O_2(PO_4)_2/Y_2O_3$ films prepared at three typical T_s with 30 ºC interval are compared in Fig. 7.1 (b). The (00*l*) diffraction peaks from $Sn_5O_2(PO_4)_2$ and the (*hhh*) peaks from Y_2O_3 peaks were observed in all the samples. A phase-pure $Sn_5O_2(PO_4)_2$ film was obtained at 565 ºC, whereas higher and lower T_s resulted in the generation of impurity phases such as $Sn_4O(PO_4)_2$. The observation of these impurity phases might be related to their lower formation enthalpy compared to $Sn_5O_2(PO_4)_2$, which was calculated by the first-principles calculation [74]. Under non-optimal growth conditions, the impurity phases appeared most likely due to their higher thermodynamic stability. Hereafter, we discuss the result of the phase-pure $Sn_5O_2(PO_4)_2$ film fabricated at the optimal substrate temperature of 565 ºC.

As mentioned above, the oriented growth of phase-pure $Sn_5O_2(PO_4)_2$ is induced by the in-plane structural similarity of $Sn_5O_2(PO_4)_2$ (001) and Y_2O_3 (111), and

dissimilarity of $Sn_4O(PO_4)_2$ (001) and Y_2O_3 (111), as shown in Fig. 7.3 [143]. In $Sn_5O_2(PO_4)_2$ (001), the lattice plane can be regarded as a quasi-equilateral triangle because the angle between *a*- and *b*-axis is 61.43° and lattice parameters along *a*- and *b*-direction are 0.7142 nm and 0.7175 nm, respectively. On the other hand, $Sn_4O(PO_4)_2$ (001) forms a rectangle with sides of 0.7353 nm along the *a*-axis and 0.9499 nm along the *b*-axis. Y_2O_3 (111) has an equilateral triangular surface structure with triangle side lengths of 1.4996 nm, which is roughly twice the lattice parameters of $Sn_5O_2(PO_4)_2$ along *a*- and *b*-direction, thus allowing for an in-plane epitaxial relationship between Y_2O_3 and $Sn_5O_2(PO_4)_2$ unlike $Sn_4O(PO_4)_2$. The lattice mismatches between $Sn_5O_2(PO_4)_2$ and Y_2O_3 are −4.7% and −4.3% along the *a*- and *b*-direction of $Sn_5O_2(PO_4)_2$, respectively. However,

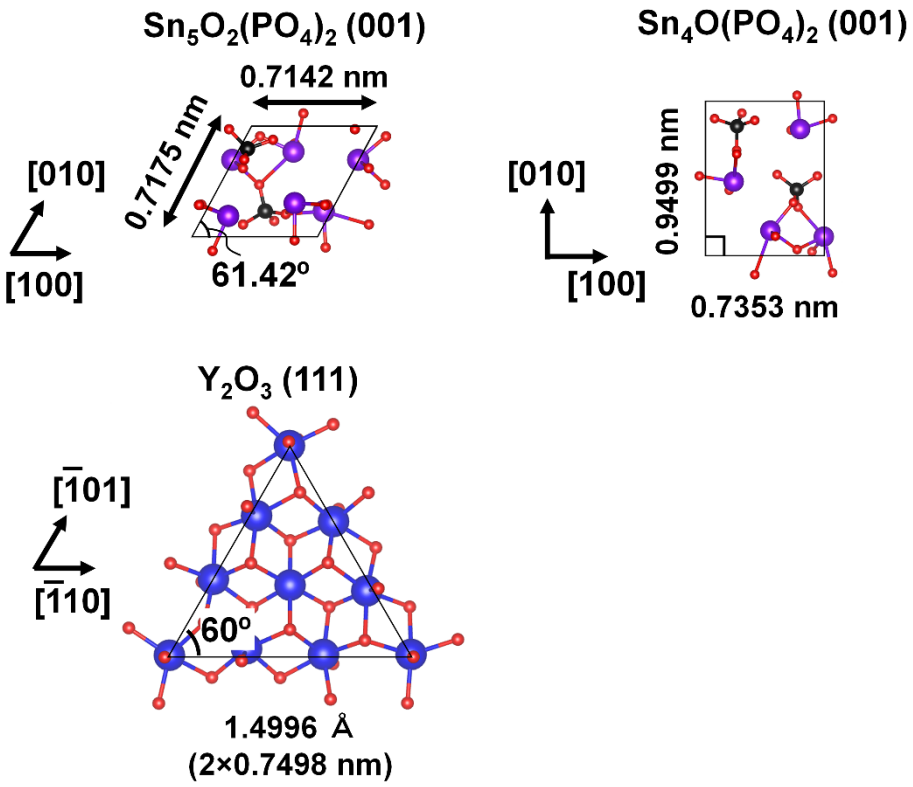

Fig. 7.3. Schematic lattice planes of $Sn_5O_2(PO_4)_2$ (001), $Sn_4O_2(PO_4)_2$ (001) and Y_2O_3(111) using the VESTA software [145]. Purple spheres indicate Sn atoms, black spheres indicate P atoms, green spheres indicate Y atoms and red spheres indicate O atoms.

since the Y_2O_3 buffer layer is oriented on glass and randomly in-plane oriented, the $Sn_5O_2(PO_4)_2$ layer is consequently also randomly in-plane oriented. Therefore, there are no periodic peaks observed by XRD phi-scans (not shown), and the in-plane epitaxial relationship cannot be proven experimentally at this point.

A low-magnification cross-section bright-field TEM micrograph is shown in Fig. 7.4 (a). A columnar structure is observed for both $Sn_5O_2(PO_4)_2$ and Y_2O_3 layers, suggesting that the (001)-oriented structure of $Sn_5O_2(PO_4)_2$ is inherited from the (111)-oriented structure of the Y_2O_3 buffer layer. The high-resolution TEM image in Fig. 7.4

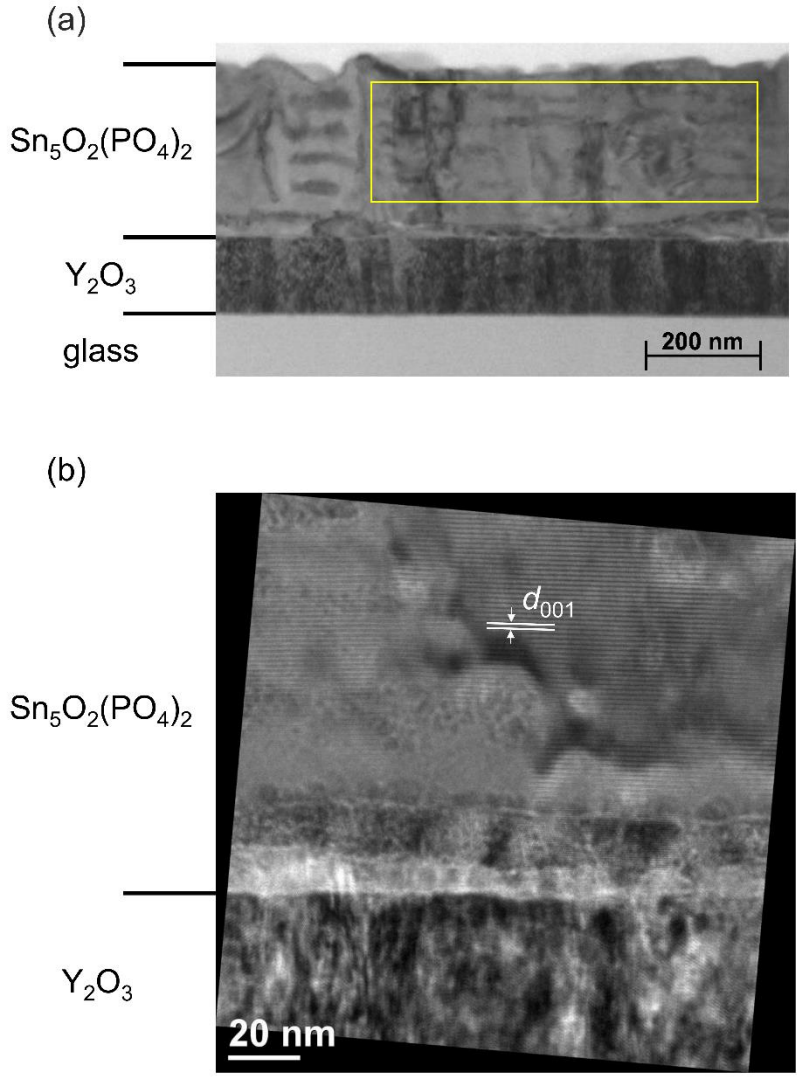

Fig. 7.4. (a) Bright-field TEM image of the cross-section of the $Sn_5O_2(PO_4)_2/Y_2O_3$ layer system. (b) High-resolution TEM image of the $Sn_5O_2(PO_4)_2/Y_2O_3$ layer system.

(b) shows the lattice pattern of the $Sn_5O_2(PO_4)_2$ structure with a distinguishable lattice spacing of d = 1.32 ± 0.02 nm, which resembles the lattice spacing of $Sn_5O_2(PO_4)_2$ in (001) direction, d = 1.29 nm [73]. The lattice spacing confirmed by TEM agrees well with the value derived by XRD, d = 1.30 nm. In addition, the TEM analysis reveals an intermediate layer with a rather inhomogeneous microstructure in-between Y_2O_3 and $Sn_5O_2(PO_4)_2$, which might originate from the lattice mismatch between film and buffer layer [144].

The chemical composition of the film within the area marked by the yellow box in Fig. 7.4 was determined to be $Sn_{5.5}P_2O_{10.7}$ by STEM-EDX on the assumption of P = 2, which is close to the stoichiometric composition $Sn_5O_2(PO_4)_2$ within an experimental error of approximately ±10%, that is due to the fact that the EDX quantification was done in a standard-free fashion. Also, sample preparation during TEM preparation might have a small effect on the composition of the film. As a complementary method to EDX, additional X-ray photoelectron spectroscopy (XPS) was used to evaluate the composition of the film. In the XPS measurement, Sn 3*d*, O 1*s*, P 2*s*, and P 2*p* regions were probed, as shown in Fig. 7.5. Due to the small phosphorus content, the P peaks were detected in the XPS spectra only as a weak signal with a poor signal-to-noise ratio, which might result in some enhanced experimental error in the composition evaluation. Both Sn 3*d* and P 2*p* binding energy values clearly coincide with values published for comparable oxides [145–147]. However, different possible oxidation states do not lead to significant binding energy differences [146,148] thus not enabling their identification with the given resolution. Due to the high surface sensitivity of XPS, some oxygen-containing surface contaminants can artificially enhance the oxygen content to some extent, adding an additional source of error for this constituent. By calculating the atomic fractions from Sn

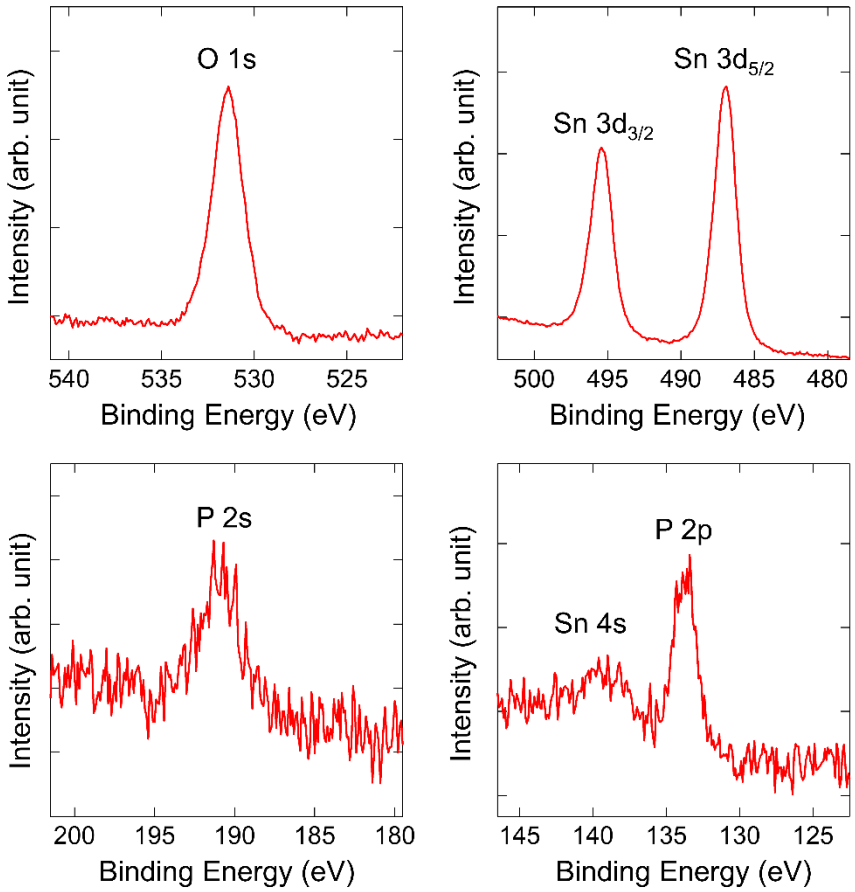

Fig. 7.5. Photoemission spectra of O 1*s*, Sn 3*d*, P 2*s* and P 2*p* of the $Sn_5O_2(PO_4)_2$ film measured by Al $K\alpha$ excitation.

3*d*, P 2*s*, and O 1*s* using sensitivity factors and inelastic mean free paths, the composition was determined to be $Sn_{5.8}P_2O_{11}$. Thus, the averaged composition of the film by EDX and XPS was calculated to be $Sn_{5.7}P_2O_{10.9}$. Both STEM-EDX and XPS revealed within their experimental error that the Sn/P ratio is close to or slightly higher than 5/2, thus indicating the formation of $Sn_5O_2(PO_4)_2$, i.e., the phase having the largest Sn/P ratio among the tin(II) phosphates. As mentioned already, the Sn/P ratio of the film was significantly higher than that of the target $Sn_2P_2O_7$, indicating the (re-)evaporation of phosphorus species from the substrate during the deposition. This is also consistent with the XRD results, see Fig. 7.1.

Such phase-pure stoichiometric thin films allow reliable optical measurements

of $Sn_5O_2(PO_4)_2$ to explore its so far unknown electronic structure and related fundamental parameters. Figure 7.6 shows the optical transmission spectra and the derived absorption coefficients of the $Sn_5O_2(PO_4)_2/Y_2O_3$ film and a bare Y_2O_3 film as a function of wavelength. The transmittance of the base layer Y_2O_3 is not higher than that of $Sn_5O_2(PO_4)_2/Y_2O_3$. The averaged transmittance in the visible region are 78% and 77% for the $Sn_5O_2(PO_4)_2/Y_2O_3$ layer system and the Y_2O_3 film, respectively. This indicates the extremely high transparency of the $Sn_5O_2(PO_4)_2$ film throughout the visible and near-infrared spectral regions. The bandgap of the phase-pure $Sn_5O_2(PO_4)_2$ grown on Y_2O_3/glass was experimentally evaluated here for the first time with the value of 3.87 eV from the Tauc plot, assuming the direct bandgap transition model as shown in the inset of Fig. 4. This value can be used as an estimate of the bandgap for $Sn_5O_2(PO_4)_2$ since the bandgap of the Y_2O_3 layer is much larger (~5.8 eV) as shown in the inset of Fig. 7.6,

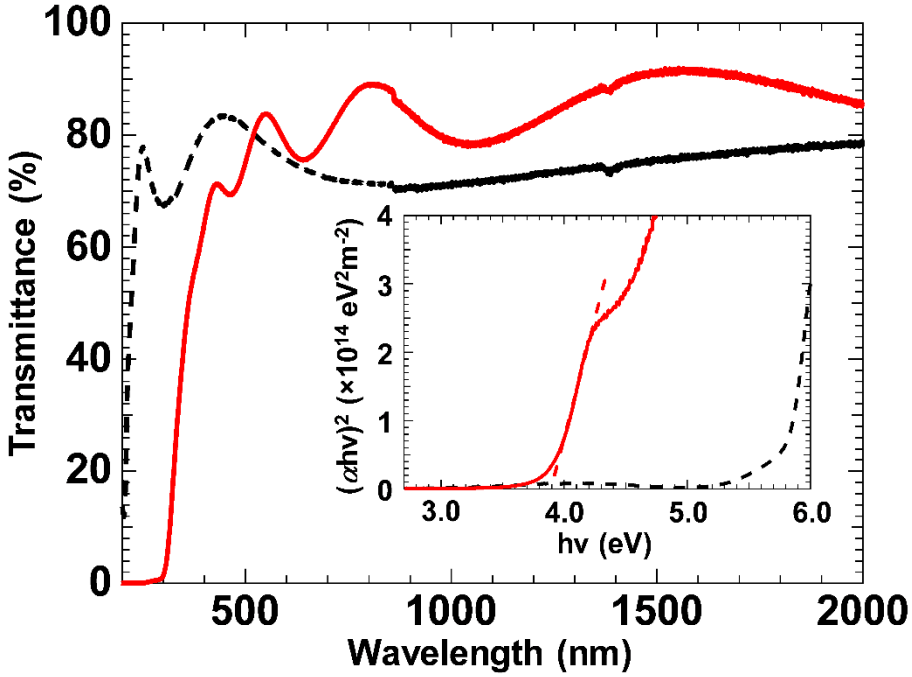

Fig. 7.6. Transmittance spectra of the phase-pure $Sn_5O_2(PO_4)_2/Y_2O_3$/glass (solid red line) and reference Y_2O_3/glass (dashed black line). (inset) Determination of optical bandgap of the $Sn_5O_2(PO_4)_2/Y_2O_3$/glass and reference Y_2O_3/glass estimated by assuming direct transition and linear extrapolation of $(\alpha h\nu)^2$, using $\alpha t = \ln(1/T)$. The thicknesses of the $Sn_5O_2(PO_4)_2$ and Y_2O_3 layers are 300 nm and 110 nm, respectively.

which was also confirmed by the previous study of a Y_2O_3 film [142]. Xu *et al.* have predicted that $Sn_5O_2(PO_4)_2$ exhibits a direct bandgap of 3.40 eV, using density functional theory (DFT) with a Tran-Blaha modified-Becke-Johnson (TB-mBJ) potential [74]. The calculated TB-mBJ bandgap showed ~10% underestimation compared to our experimentally obtained value. Such underestimation by using TB-mBJ potential has already been reported for other typical TCOs such as In_2O_3, ZnO, and SnO_2 [149]. Thus, the predicted bandgap from the DFT calculation agrees reasonably well with our experimental value for the optical bandgap of $Sn_5O_2(PO_4)_2$ assuming a direct transition.

Finally, we briefly discuss the electronic properties of the $Sn_5O_2(PO_4)_2/Y_2O_3$ films. The obtained $Sn_5O_2(PO_4)_2$ is an intrinsic semiconductor without intentional doping, which is perfect for the study of the fundamental physics of the material. Its resistivity is too high for reliable Seebeck and Hall measurement, as shown in Fig. 7.7. Such low conductivity can be explained by a very low concentration of shallow, electrically active defects or by strong compensation. A recent theoretical study revealed that intrinsic

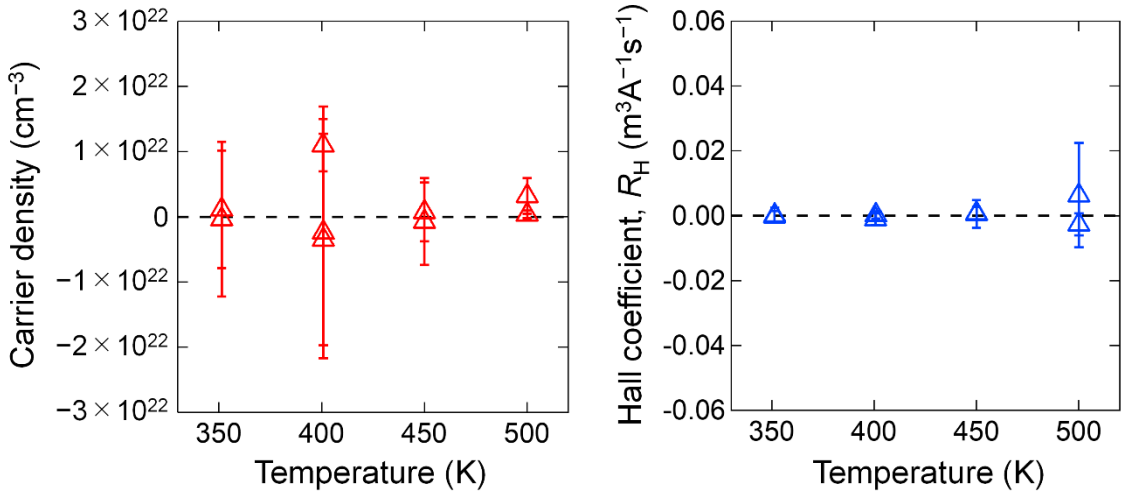

Fig. 7.7. Temperature dependence of carrier density and Hall coefficient (R_H) for the $Sn_5O_2(PO_4)_2$ film measured by Physical Property Measurement System. Negative carrier density and positive R_H indicate the existence of p-type carriers in the sample. The experimental errors were too large to determine the carrier type of the $Sn_5O_2(PO_4)_2$ film.

defects such as the tin vacancy V_{Sn} give a deep acceptor level in $Sn_5O_2(PO_4)_2$ [150].

The main way to reduce resistivity and realize *p*-type conductivity in this material is extrinsic doping with suitable impurities, which is widely utilized in transparent conductive oxides. We suggest aliovalent dopants to induce hole carriers in $Sn_5O_2(PO_4)_2$, i.e., Tl^+ at Sn^{2+} site [151], or N^{3-} at O^{2-} site.

7.4 Conclusion

In summary, I succeeded to fabricate phase-pure $Sn_5O_2(PO_4)_2$ films. High-quality $Sn_5O_2(PO_4)_2$ thin films were obtained on amorphous glass substrates with oriented Y_2O_3 buffer layers deposited using pulsed laser deposition. The problem of the formation of impurity phases was solved by an appropriate buffer layer as well as the control of the chemical composition through optimization of the substrate temperature. The $Sn_5O_2(PO_4)_2$ film obtained at 565 ºC on a Y_2O_3/glass template was found to have no impurity phases and being highly oriented with the *c*-axis in the out-of-plane direction. The (001)-orientation of the $Sn_5O_2(PO_4)_2$ layer is related to the lattice similarity between $Sn_5O_2(PO_4)_2$ (001) and Y_2O_3 (111); the in-plane epitaxial relationship cannot be verified at this moment using the oriented nature of the Y_2O_3 buffer layer. The composition of the obtained film was near-stoichiometric, indicating an almost intrinsic semiconductor. The $Sn_5O_2(PO_4)_2$ film exhibited high transparency in the visible and near-infrared spectral regions with a large bandgap of 3.87 eV. Thus, such phase-pure, stoichiometric thin films allow experimental investigation of the fundamental physics of $Sn_5O_2(PO_4)_2$ for the first time. Hole carriers are expected to be possibly induced by aliovalent dopants. These

results pave the way for exploring the novel promising *p*-type tin(II) phosphate TCO $Sn_5O_2(PO_4)_2$.

Chapter 8

Conclusions

In this thesis, I successfully developed thin films of Sn-based transparent conductive oxides with high carrier mobility by implementing the following three strategies: (1) combining spatially-extended cation *s*-orbitals and edge-sharing structure of the cations, resulting in the reduced carrier effective mass by direct overlap of vacant *s* orbitals between the neighboring cations, (2) suppressing the extrinsic carrier scattering which leads to the long average carrier scattering time, and (3) selecting the dopants which generate carriers without impairing CBM of the host material. In this chapter, I summarize the results of the previous chapters and describe future prospects.

8.1 Summary

High mobility approaching the intrinsic limit in Ta-doped SnO_2 films epitaxially grown on TiO_2 (001) substrates

TTO films were epitaxially grown on TiO_2 (001) substrates. The n_e values for the TTO films corresponded to the Ta concentration, indicating very high doping efficiency of Ta. At high n_e region ($n_e \geq 9 \times 10^{19}$ cm^{-3}), the μ_H values of the TTO films agreed well with the intrinsic limit of μ_H, assuming that only phonon and ionized impurities contributed to the carrier scattering. The negligible contribution of grain-

boundary scattering to μ_H might arise from a reduced density of CSPs. The TTO films with $n_e \sim 1 \times 10^{20}$ cm^{-3} showed a very high μ_H of 130 cm^{2}V^{-1}s^{-1}, which is the highest among SnO_2 films thus far reported.

Carrier generation mechanism in W-doped SnO_2 epitaxial films with high mobility

WTO films were epitaxially grown on TiO_2 (001) substrates. The n_e values for the WTO films monotonically increased as the W amount increased and agreed well with the ideal n_e values on the assumption of W^{5+}. The μ_H values of the WTO films with $n_e \geq 1.9 \times 10^{20}$ cm^{-3} were close to the intrinsic limit of μ_H assuming that only phonon and ionized impurities of W^{5+} contributed to the carrier scattering. The doped W atoms were homogeneously distributed in the WTO films, which was confirmed by STEM-EDX. XFH measurements revealed that the uniformly distributed W atoms were substituted for the Sn sites. These results clearly demonstrated that W behaves as an excellent dopant in SnO_2 thin film with high μ_H and controllable n_e.

Fabrication of P-doped SnO_2 thin films by pulsed laser deposition

PTO polycrystalline films on glass and epitaxial films on TiO_2 (001) were fabricated by PLD. The doping efficiency of the PTO films reached the maximum at T_s = 350 °C, while higher T_s resulted in the reduction of doping efficiency and P amount. This result indicated the existence of V_{Sn} induced by possible re-evaporation of P during the deposition, behaving as an acceptor-like defect. As x increased, the n_e values systematically increased and reached 1.6×10^{20} cm^{-3} at the heavily-doped region, demonstrating the carrier generation by P-doping. The film exhibited high transparency to visible light, indicating the potential of PTO thin films as a practical TCO.

Fabrication of textured SnO_2 transparent conductive films using self-assembled Sn nanospheres

I proposed a novel method of fabricating transparent conductive SnO_2 films with textured surfaces by processing substrates with a bottom-up technique. Substrate processing consists of three steps: deposition of precursor Sn films on glass substrates, the formation of self-assembled Sn nanospheres with reductive annealing, and conversion of Sn to SnO_2 with oxidative annealing. SnO_2 films conformally deposited on the templated substrates feature textured surfaces, resulting in enhanced haze values. In addition, the templates acted as seed layers and thus promoted grain growth, which contributed to increased conductivity in the TTO layers. These optoelectronic properties show promise for the use of the substrates as transparent electrodes in PVs. The proposed method could be highly productive and scalable provided that the method can be adapted to reactive sputtering with metallic targets.

Experimental evidence of wide bandgap in triclinic (001)-oriented $Sn_5O_2(PO_4)_2$ thin films on Y_2O_3 buffered glass substrates

Phase-pure (001)-oriented $Sn_5O_2(PO_4)_2$ films were fabricated on glass with the aid of (111)-oriented Y_2O_3 buffer layers by optimizing T_s. The (001)-orientation of the $Sn_5O_2(PO_4)_2$ layer is related to the lattice similarity between $Sn_5O_2(PO_4)_2$ (001) and Y_2O_3 (111). The composition of the obtained film was near-stoichiometric, indicating an almost intrinsic semiconductor. The $Sn_5O_2(PO_4)_2$ film showed high transparency in the visible and near-infrared spectral regions with a bandgap as large as 3.87 eV. Such phase-pure, stoichiometric thin films allow experimental investigation of the fundamental physics of $Sn_5O_2(PO_4)_2$ for the first time. Hole carriers are expected to be possibly induced by

aliovalent dopants.

8.2 Future prospects

(1) Doping *d*-block elements to other tin-based TCOs

This thesis focused on SnO_2 as a representative for *n*-type Sn-based TCOs. From the viewpoint of dopant, Ta and W were revealed as effective dopants of SnO_2 for realizing high μ_H approaching to the intrinsic limit with controlling n_e. The extremely-high μ_H was qualitatively rationalized by the reduced mixing orbitals between the host Sn *s*-states at the CBM and the dopant *d*-states, leading to the minimal hybridization between the CBM and the dopant states. These findings can be transferred to the other Sn-based oxides. Perovskite $BaSnO_3$, for instance, has recently been reported as a new promising *n*-type TCO, in which the CBM is primarily composed of Sn *s*-states [152]. Similar to SnO_2, each Sn atom in $BaSnO_3$ is surrounded by six oxygen atoms, forming an octahedron. Thus far, n_e of $BaSnO_3$ has mainly been controlled by the substitution of La^{3+} for Ba^{2+} site [153]. However, La^{3+} substitution suffers from low carrier activation, possibly resulting from the formation of neutral impurities that act as scattering centers. According to the findings in this study, the n_e values of $BaSnO_3$ might be further tuned by the substitution of Ta^{5+} or W^{5+} for Sn^{4+} with a high carrier activation ratio. Furthermore, the CBM of $BaSnO_3$ would not be impaired by substituting these d-block dopants, resulting in an increased μ_H in $BaSnO_3$. Future works on Ta- or W-doped $BaSnO_3$ or other Sn-based TCOs would elucidate the validity of the abovementioned hypothesis toward high μ_H.

(2) Stabilizing other triclinic thin films by buffer layer with a specific orientation

Although I focused on triclinic $Sn_5O_2(PO_4)_2$ as a promising *p*-type TCO, I believe that the fabrication technique of phase-pure (001)-oriented $Sn_5O_2(PO_4)_2$ thin films can be applied to the other triclinic oxides. In Chapter 7, the triclinic $Sn_5O_2(PO_4)_2$ films with (001)-orientation were stabilized by inserting (111)-oriented Y_2O_3 polycrystalline buffer layer. Interestingly, as stated in Chapter 7, phase-pure $Sn_5O_2(PO_4)_2$ films were not obtained when deposited on single-crystalline YSZ (111) substrates. I speculated that the presence of the (111)-oriented polycrystalline Y_2O_3 buffer layer is essential for the selective growth of triclinic $Sn_5O_2(PO_4)_2$. Stabilization of high-quality triclinic films by oriented buffer layers would allow fundamental researches and applications of thin films of triclinic material, e.g., ferroelectric triclinic $BiFeO_3$ [154]. Thus far, little attention has been paid to the fabrication of triclinic thin films, possibly due to the lack of suitable lattice-matched substrates. The concept proposed in this study would pave the way toward realizing new high-quality triclinic thin films with improved properties, including novel *p*-type TCOs.

Acknowledgment

I would like to show my appreciation to all those who have helped me conduct the research related to this thesis.

First of all, I would like to thank my supervisor, Prof. Tetsuya Hasegawa, for fully supporting me throughout my Ph.D. period. His deep insights and interests are always guiding me in the critical direction of the research. If it had not been for his kind support, I could not have conducted any research in such a comfortable environment. I am also grateful to Dr. Shoichiro Nakao and Prof. Yasushi Hirose, who have provided me vigorous support from the very first day I started the research life. Their advice has always shed light on the issues I faced during the research. It is very fortunate for me to have started my research with them. I also owe my doctoral thesis to Dr. Kei Shigematsu at Tokyo Institute of Technology, who also taught me the basis of experimental technique. I am really grateful to them.

I would like to express my appreciation to Prof. Marius Grundmann, Prof. Michael Lorenz, and Prof. Chang Yang for the support during my research life at Leipzig. Prof. Grundmann gave me an opportunity to conduct the research in his group. Prof. Michael Lorenz and Prof. Chang Yang provided me considerable support in every moment of the research in Leipzig. Their advice was full of fruitful inspirations.

I would also show my appreciation to Dr. Akira Chikamatsu, Dr. Hideyuki Kamisaka, and Dr. Tsukasa Katayama. They provided support through valuable comments in seminars, daily chatting, and technical assistance.

I would like to appreciate Mr. Takahiro Maruyama, Mr. Satoshi Fujiwara, and Mr. Toru Koizumi. They joined the Hasegawa laboratory together with me when we were bachelor students. They provided me considerable supports not only in the research but also in daily life. I feel fortunate to have spent my student life with them.

I would also like to show my gratitude to the “KAST” (now KISTEC) members of the Hasegawa laboratory, Dr. Atsushi Suzuki, Dr. Masahito Sano, Dr. Motaneeyachart Vitchaphol, Dr. Dai Kutsuzawa, Mr. Takanori Yamazaki, Mr. Naoki Kashiwa, Mr. Shunsuke Shibata, Ms. Zhu Yuting, and Mr. Shunya Tanaka. I would also like to express my thank to Hirose group members, Mr. Takuto Wakasugi, Mr. Masato Tsuchii, Mr. Jin Gou, Mr. Chen Zhen, Ms. Wang Yannan, Mr. Yusuke Sakagawa, Mr. Yo Nagashima, and Mr. Kazuya Okada.

With respect to the investigation of local atomic structures, I would like to acknowledge Dr. Daisuke Ogawa for transmission electron microscopy measurement, and Prof. Koichi Hayashi and Dr. Koji Kimura for X-ray fluorescence measurement. Some important experiments on determining the local structure of the film could be accomplished with their help on their state-of-the-art techniques.

I am grateful to other colleagues and former colleagues, Dr. Thantip S. Krasienapibal, Dr. Shungo Kojima, Dr. Ryosuke Sei, Dr. Mayuko Oka, Dr. Kenichi Kaminaga, Dr. Tomoya Onozuka, Mr. Yutaka Uchida, Mr. Keisuke Kawahara, Mr. Ryota Kantake, Mr. Fahd Khan Sikandar, Dr. Yuji Kurauchi, Mr. Saki Kawahara, Mr. Yusuke Suzuki, Mr. Naoaki Hashimoto, Mr. Keisuke Yamada, Mr. Ken Hayahara, Mr. Shishin Mo, Mr. Kuni Yamada, Mr. Ruocheng Han, Mr. Gu Ke, Mr. Ryosuke Ishigami, Mr. Kento Magara, Mr. Takuya Sahashi, Mr. Shi Tianrui, Mr. Jun Kasahara, Mr. Atori Miki, Mr. Takuma Nishimura, Mr. Yusuke Wakayama, Mr. Shota Fukuma, Mr. Hiroki Ogura, Mr.

Hayate Suzuki, and Ms. Miki Takahashi. I would also like to thank the secretaries of the Hasegawa laboratory, Mrs. Aya Imoji, Mrs. Mie Umino and Mrs. Miki Komazawa.

Lastly, I would like to thank my family and friends for their support. I want to express my thank, especially to my parents, for their considerable support, patience, and understanding. Without that, I could not carry out the research during my Ph.D. period.

Bibliography

[1] K. Bädeker, Ann. Physik **327**, 749 (1907).

[2] *Handbook of Transparent Conductors*, ed. D. S. Ginley (Springer, New York, 2010)

[3] K. Ellmer, Nat. Photonics **6**, 809 (2012).

[4] F. J. Arlinghaus, J. Phys. Chem. Solids **35**, 931 (1974).

[5] Ç. Kılıç and A. Zunger, Phys. Rev. Lett. **88**, 955011 (2002).

[6] C. Terrier, J. P. Chatelon, and J. A. Roger, Thin Solid Films **295**, 95 (1997).

[7] T. J. Coutts, D. L. Young, and X. Li, MRS Bull. **25,** 58 (2000).

[8] L. Hu, R. H. Wei, X. W. Tang, W. J. Lu, X. B. Zhu, and Y. P. Sun, J. Appl. Phys. **128**, 140902 (2020).

[9] L. Zhang, Y. Zhou, L. Guo, W. Zhao, A. Barnes, H.-T. Zhang, C. Eaton, Y. Zheng, M. Brahlek, H. F. Haneef, N. J. Podraza, M. H. W. Chan, V. Gopalan, K. M. Rabe, and R. Engel-Herbert, Nat. Mater. **15**, 204 (2016).

[10] Y. Park, J. Roth, D. Oka, Y. Hirose, T. Hasegawa, A. Paul, A. Pogrebnyakov, V. Gopalan, T. Birol, and R. Engel-Herbert, Commun. Phys. **3**, 1 (2020).

[11] G. Brunin, G.-M. Rignanese, and G. Hautier, Phys. Rev. Mater. **3**, 064602 (2019).

[12] L. Farrell, K. Fleischer, D. Caffrey, D. Mullarkey, E. Norton, and I. V. Shvets, Phys. Rev. B **91**, 125202 (2015).

[13] K. H. L. Zhang, Y. Du, A. Papadogianni, O. Bierwagen, S. Sallis, L. F. J. Piper,

M. E. Bowden, V. Shutthanandan, P. V. Sushko, and S. A. Chambers, Adv. Mater. **27**, 5191 (2015).

[14] H. Kawazoe, N. Ueda, H. Un'No, T. Omata, H. Hosono, and H. Tanoue, J. Appl. Phys. **76**, 7935 (1994).

[15] *Handbook of Electronic and Photonic Materials*, eds. S. Kasap, P. Capper (Springer International, 2017)

[16] Y. Furubayashi, T. Hitosugi, Y. Yamamoto, K. Inaba, G. Kinoda, Y. Hirose, T. Shimada, and T. Hasegawa, Appl. Phys. Lett. **86**, 252101 (2005).

[17] E. Conwell and V. F. Weisskopf, Phys. Rev. **77**, 388 (1950).

[18] R. B. Dingle, Philos. Mag. **46**, 831 (1955).

[19] D. J. Howarth and E. H. Sondheimer, Proc. R. Soc. Lond. A **219**, 53 (1953).

[20] C. Erginsoy, Phys. Rev. **79**, 1013 (1950).

[21] B. Pödör, Phys. Status Solidi **16**, K167 (1966).

[22] N. G. Weimann, L. F. Eastman, D. Doppalapudi, H. M. Ng, and T. D. Moustakas, J. Appl. Phys. **83**, 3656 (1998).

[23] B. Bansal, R. Ghosh, and V. Venkataraman, J. Appl. Phys. **113**, 163705 (2013).

[24] R. Jaszek, J. Mater. Sci. Mater. Electron. **12**, 1 (2001).

[25] S. K. Vasheghani Farahani, T. D. Veal, A. M. Sanchez, O. Bierwagen, M. E. White, S. Gorfman, P. A. Thomas, J. S. Speck, and C. F. McConville, Phys. Rev. B **86**, 245315 (2012).

[26] D. C. Look, H. Lu, W. J. Schaff, J. Jasinski, and Z. Liliental-Weber, Appl. Phys. Lett. **80**, 258 (2002).

[27] J. Y. W. Seto, J. Appl. Phys. **46**, 5247 (1975).

[28] T. Makino, Y. Segawa, A. Tsukazaki, A. Ohtomo, and M. Kawasaki, Appl. Phys.

Lett. **87**, 022101 (2005).

[29] N. Preissler, O. Bierwagen, A. T. Ramu, and J. S. Speck, Phys. Rev. B **88**, 085305 (2013).

[30] Y. Furubayashi, N. Yamada, Y. Hirose, Y. Yamamoto, M. Otani, T. Hitosugi, T. Shimada, and T. Hasegawa, J. Appl. Phys. **101**, 093705 (2007).

[31] T. Minami, MRS Bull. **25**, 38 (2000).

[32] A. Walsh, J. L. F. Da Silva, and S.-H. Wei, Phys. Rev. B **78**, 075211 (2008).

[33] J. E. N. Swallow, B. A. D. Williamson, S. Sathasivam, M. Birkett, T. J. Featherstone, P. A. E. Murgatroyd, H. J. Edwards, Z. W. Lebens-Higgins, D. A. Duncan, M. Farnworth, P. Warren, N. Peng, T.-L. Lee, L. F. J. Piper, A. Regoutz, C. J. Carmalt, I. P. Parkin, V. R. Dhanak, D. O. Scanlon, and T. D. Veal, Mater. Horiz. **7**, 236 (2020).

[34] M. Feneberg, C. Lidig, K. Lange, M. E. White, M. Y. Tsai, J. S. Speck, O. Bierwagen, and R. Goldhahn, Phys. Status Solidi A **211**, 82 (2014).

[35] X. Yu, T. J. Marks, and A. Facchetti, Nat. Mater. **15**, 383 (2016).

[36] C. Wei Shih, A. Chin, C. Fu Lu, and W. Fang Su, Sci. Rep. **6**, 19023 (2016).

[37] S. Das and V. Jayaraman, Prog. Mater. Sci. **66**, 112 (2014).

[38] S. Vallejos, S. Selina, F. E. Annanouch, I. Gràcia, E. Llobet, and C. Blackman, Sci. Rep. **6**, 28464 (2016).

[39] A. Palla Papavlu, T. Mattle, S. Temmel, U. Lehmann, A. Hintennach, A. Grisel, A. Wokaun, and T. Lippert, Sci. Rep. **6**, 25144 (2016).

[40] J. K. Yang, B. Liang, M. J. Zhao, Y. Gao, F. C. Zhang, and H. L. Zhao, Sci. Rep. **5**, 15001 (2015).

[41] S. Yu, L. Li, X. Lyu, and W. Zhang, Sci. Rep. **6**, 20399 (2016).

[42] M. Batzill and U. Diebold, Prog. Surf. Sci. **79**, 47 (2005).

[43] M. Behtash, P. H. Joo, S. Nazir, and K. Yang, J. Appl. Phys. **117**, 175101 (2015).

[44] K. Ellmer, J. Phys. D. Appl. Phys. **34**, 3097 (2001).

[45] C. G. Fonstad and R. H. Rediker, J. Appl. Phys. **42**, 2911 (1971).

[46] Z. Galazka, R. Uecker, D. Klimm, K. Irmscher, M. Pietsch, R. Schewski, M. Albrecht, A. Kwasniewski, S. Ganschow, D. Schulz, C. Guguschev, R. Bertram, M. Bickermann, and R. Fornari, Phys. Status Solidi A **211**, 66 (2014).

[47] D. F. Morgan and D. A. Wright, Br. J. Appl. Phys. **17**, 337 (1966).

[48] M. E. White, O. Bierwagen, M. Y. Tsai, and J. S. Speck, J. Appl. Phys. **106**, 093704 (2009).

[49] H. Mun, H. Yang, J. Park, C. Ju, and K. Char, APL Mater. **3**, 076107 (2015).

[50] S. Semancik and R. E. Cavicchi, Thin Solid Films **206**, 81 (1991).

[51] K. Rachut, C. Körber, J. Brötz, and A. Klein, Phys. Status Solidi A **211**, 1997 (2014).

[52] M. Okude, K. Ueno, S. Itoh, M. Kikuchi, A. Ohtomo, and M. Kawasaki, J. Phys. D: Appl. Phys. **41**, 125309 (2008).

[53] Y. Zhen, T. Ohsawa, Y. Adachi, I. Sakaguchi, B. Li, J. Li, R. Matsuoka, T. Nishimura, K. Matsumoto, H. Haneda, and N. Ohashi, J. Appl. Phys. **108**, 104901 (2010).

[54] J. E. Dominguez, L. Fu, and X. Q. Pan, Appl. Phys. Lett. **81**, 5168 (2002).

[55] Y.-W. Kim, S. W. Lee, and H. Chen, Thin Solid Films **405**, 256 (2002).

[56] X. Feng, J. Ma, F. Yang, F. Ji, F. Zong, C. Luan, and H. Ma, Appl. Surf. Sci. **254**, 6601 (2008).

[57] C. Luan, Z. Zhu, W. Mi, and J. Ma, J. Alloys Compd. **586**, 426 (2014).

[58] S. Nakao, N. Yamada, T. Hitosugi, Y. Hirose, T. Shimada, and T. Hasegawa, Appl. Phys. Express **3**, 031102 (2010).

[59] H. Toyosaki, M. Kawasaki, and Y. Tokura, Appl. Phys. Lett. **93**, 132109 (2008).

[60] N. Yamada, S. Nakao, T. Hitosugi, and T. Hasegawa, Jpn. J. Appl. Phys. **49**, 108002 (2010).

[61] S. Nakao, N. Yamada, T. Hitosugi, Y. Hirose, T. Shimada, and T. Hasegawa, Phys. Status Solidi C **8**, 543 (2011).

[62] Y. Huang, Q. Zhang, and G. Li, Semicond. Sci. Technol. **24**, 015003 (2009).

[63] B. A. D. Williamson, T. J. Featherstone, S. S. Sathasivam, J. E. N. Swallow, H. Shiel, L. A. H. Jones, M. J. Smiles, A. Regoutz, T.-L. Lee, X. Xia, C. Blackman, P. K. Thakur, C. J. Carmalt, I. P. Parkin, T. D. Veal, and D. O. Scanlon, Chem. Mater. **32**, 1964 (2020).

[64] H. Peng, J. D. Perkins, and S. Lany, Chem. Mater. **26**, 4876 (2014).

[65] Y.-S. Hsu and S. K. Ghandhi, J. Electrochem. Soc. **127**, 1595 (1980).

[66] J. P. Upadhyay, S. R. Vishwakarma, and H. C. Prasad, Thin Solid Films, **169**, 195 (1989).

[67] E. Fortunato, P. Barquinha, and R. Martins, Adv. Mater. **24**, 2945 (2012).

[68] K. H. L. Zhang, K. Xi, M. G. Blamire, and R. G. Egdell, J. Phys.: Condens. Matter **28**, 383002 (2016).

[69] H. Peng, A. Bikowski, A. Zakutayev, and S. Lany, APL Mater. **4**, 106103 (2016).

[70] V.-A. Ha, F. Ricci, G.-M. Rignanese, and G. Hautier, J. Mater. Chem. C **5**, 5772 (2017).

[71] V. V. Chernaya, A. S. Mitiaev, P. S. Chizhov, E. V. Dikarev, R. V. Shpanchenko, E. V. Antipov, M. V. Korolenko, and P. B. Fabritchnyi, Chem. Mater. **17**, 284

(2005).

[72] M. Mathew, L. W. Schroeder, and T. H. Jordan, Acta Crystallogr. B, **33**, 1812 (1977).

[73] L. Q. Fan, J. H. Wu, and Y. F. Huang, Z. Anorg. Allg. Chem. **634**, 534 (2008).

[74] Q. Xu, Y. Li, L. Zhang, W. Zheng, D. J. Singh, and Y. Ma, Chem. Mater. **29**, 2459 (2017).

[75] J. Schou, Appl. Surf. Sci. **255**, 5191 (2009).

[76] D. H. Lowndes, D. B. Geohegan, A. A. Puretzky, D. P. Norton, and C. M. Rouleau, Science **273**, 898 (1996).

[77] H. Ohta, H. Mizoguchi, M. Hirano, S. Narushima, T. Kamiya, and H. Hosono, Appl. Phys. Lett. **82**, 823 (2003).

[78] H. Ohta, K. Nomura, M. Orita, M. Hirano, K. Ueda, T. Suzuki, Y. Ikuhara, and H. Hosono, Adv. Funct. Mater. **13**, 139 (2003).

[79] J. E. Greene, J. Vac. Sci. Technol. A **35**, 05C204 (2017).

[80] K. Hayashi, N. Happo, S. Hosokawa, W. Hu, and T. Matsushita, J. Phys.: Condens. Matter **24**, 093201 (2012).

[81] K. Hayashi and P. Korecki, J. Phys. Soc. Japan **87**, 061003 (2018).

[82] K. Kimura, K. Hayashi, L. V. Yashina, N. Happo, T. Nishioka, Y. Yamamoto, Y. Ebisu, T. Ozaki, S. Hosokawa, T. Matsushita, and H. Tajiri, Surf. Interface Anal. **51**, 51 (2019).

[83] P. Bauer, E. Steinbauer, and J. P. Biersack, Nucl. Inst. Methods Phys. Res. B **79**, 443 (1993).

[84] A. Weber and H. Mommsen, Nucl. Inst. Methods **204**, 559 (1983).

[85] W. Eckstein and M. Mayer, Nucl. Inst. Methods Phys. Res. B **153**, 337 (1999).

[86] I. Harayama, K. Nagashima, Y. Hirose, H. Matsuzaki, and D. Sekiba, Nucl. Inst. Methods Phys. Res. B **384**, 61 (2016).

[87] M. E. White, M. Y. Tsai, F. Wu, and J. S. Speck, J. Vac. Sci. Technol. A **26**, 1300 (2008).

[88] M. Y. Tsai, M. E. White, and J. S. Speck, J. Cryst. Growth **310**, 4256 (2008).

[89] R. G. Palgrave, A. Bourlange, D. J. Payne, J. S. Foord, and R. G. Egdell, Cryst. Growth Des. **9**, 1793 (2009).

[90] J. Jia, N. Oka, M. Kusayanagi, S. Nakatomi, and Y. Shigesato, Appl. Phys. Express **7**, 105802 (2014).

[91] Y. Shigesato and D. C. Paine, Appl. Phys. Lett. **62**, 1268 (1993).

[92] M. Weidner, J. Brötz, and A. Klein, Thin Solid Films **555**, 173 (2014).

[93] R. Summitt, J. Appl. Phys. **39**, 3762 (1968).

[94] J. Bruneaux, H. Cachet, M. Froment, and A. Messad, Thin Solid Films **197**, 129 (1991).

[95] H. Wakabayashi, T. Suzuki, Y. Iwazaki, and M. Fujimoto, Jpn. J. Appl. Phys. **40**, 6081 (2001).

[96] L. A. Bursill and B. G. Hyde, Prog. Solid State Chem. **7**, 177 (1972).

[97] D. H. Kim, W.-S. Kim, S. B. Lee, and S.-H. Hong, Sens. Actuators B Chem. **147**, 653 (2010).

[98] D. H. Kim, J.-H. Kwon, M. Kim, and S.-H. Hong, J. Cryst. Growth **322**, 33 (2011).

[99] C. Agashe, J. Hüpkes, G. Schöpe, and M. Berginski, Sol. Energy Mater. Sol. Cells **93**, 1256 (2009).

[100] M. Isshiki, T. Ikeda, J. Okubo, T. Oyama, E. Shidoji, H. Odaka, P. Sichanugrist,

and M. Konagai, Jpn. J. Appl. Phys. **51**, 095801 (2012).

[101] J. J. Barton, Phys. Rev. Lett. **67**, 3106 (1991).

[102] S. Nakao, N. Yamada, T. Hitosugi, Y. Hirose, T. Shimada, and T. Hasegawa, Thin Solid Films **518**, 3093 (2010).

[103] K. Suzuki and M. Mizuhashi, Thin Solid Films **97**, 119 (1982).

[104] E. Korhonen, V. Prozheeva, F. Tuomisto, O. Bierwagen, J. S. Speck, M. E. White, Z. Galazka, H. Liu, N. Izyumskaya, V. Avrutin, Ü Özgür, and H. Morkoç, Semicond. Sci. Technol. **30**, 024011 (2015).

[105] R. Delahoy and S. Guo, in *Handbook of Photovoltaic Science and Engineering*, ed. A. Luque and S. Hegedus (Wiley, Hoboken, NJ, 2011) 2nd ed., Chap. 17.

[106] E. Fortunato, D. Ginley, H. Hosono, and D. C. Paine, MRS Bull. **32**, 242 (2007).

[107] M. Konagai, Jpn. J. Appl. Phys. **50**, 030001 (2011).

[108] F.-J. Haug and C. Ballif, Energy Environ. Sci. **8**, 824 (2015).

[109] M. L. Brongersma, Y. Cui, and S. Fan, Nat. Mater. **13**, 451 (2014).

[110] H. W. Deckman, C. R. Wronski, H. Witzke, and E. Yablonovitch, Appl. Phys. Lett. **42**, 968 (1983).

[111] H. Sai, T. Matsui, H. Kumagai, and K. Matsubara, Appl. Phys. Express **11**, 022301 (2018).

[112] L. Cojocaru, S. Uchida, P. V. V. Jayaweera, S. Kaneko, H. Wang, J. Nakazaki, T. Kubo, and H. Segawa, Energy Technol. **5**, 1762 (2017).

[113] R. Mishima, M. Hino, H. Uzu, T. Meguro, and K. Yamamoto, Appl. Phys. Express **10**, 062301 (2017).

[114] H. Iida, N. Shiba, T. Mishuku, H. Karasawa, A. Ito, M. Yamanaka, and Y. Hayashi, IEEE Electron Device Lett. **4**, 157 (1983).

[115] M. Mizuhashi, Y. Gotoh, and K. Adachi, Jpn. J. Appl. Phys. **27**, 2053 (1988).

[116] T. Oyama, M. Kambe, N. Taneda, and K. Masumo, MRS Proc. **1101**, 1101-KK02-01(2008).

[117] W. W. Wenas, A. Yamada, M. Konagai, and K. Takahashi, Jpn. J. Appl. Phys. **30**, L441 (1991).

[118] S. Faÿ, J. Steinhauser, S. Nicolay, and C. Ballif, Thin Solid Films **518**, 2961 (2010).

[119] Y. B. Kim, B. H. Choi, J. H. Lee, and J. H. Kim, Jpn. J. Appl. Phys. **50**, 06GG09 (2011).

[120] O. Kluth, G. Schöpe, J. Hüpkes, C. Agashe, J. Müller, and B. Rech, Thin Solid Films **442**, 80 (2003).

[121] M. Berginski, J. Hüpkes, M. Schulte, G. Schöpe, H. Stiebig, B. Rech, and M. Wuttig, J. Appl. Phys. **101**, 074903 (2007).

[122] T. Minami, T. Miyata, R. Uozaki, H. Sai, and T. Koida, Thin Solid Films **614**, 56 (2016).

[123] A. Hongsingthong, T. Krajangsang, I. A. Yunaz, S. Miyajima, and M. Konagai, Appl. Phys. Express **3**, 051102 (2010).

[124] C. Battaglia, J. Escarré, K. Söderström, M. Charrière, M. Despeisse, F.-J. Haug, and C. Ballif, Nat. Photonics **5**, 535 (2011).

[125] M. Boccard, C. Battaglia, S. Hänni, K. Söderström, J. Escarré, S. Nicolay, F. Meillaud, M. Despeisse, and C. Ballif, Nano Lett. **12**, 1344 (2012).

[126] C. Niikura, A. Chowdhury, B. Janthong, P. Sichanugrist, and M. Konagai, Appl. Phys. Express **9**, 042301 (2016).

[127] A. G. Aberle and P. I. Widenborg, in *Handbook of Photovoltaic Science and*

Engineering, ed. A. Luque and S. Hegedus (Wiley, Hoboken, NJ, 2011) 2nd ed., Chap. 11.

[128] S.-H. Yu, P.-C. Ho, C.-L. Lee, C.-C. Bi, C.-H. Yeh, and C.-Y. Chang, Appl. Phys. Express **6**, 022301 (2013).

[129] J. Li, Y. Lu, J. Huang, E. Moulin, F.-J. Haug, C. Ballif, and W. Song, Sol. Energy **115**, 518 (2015).

[130] R. Otsuka, T. Endo, T. Takano, S. Takemura, R. Murakami, R. Muramoto, J. Madarász, and M. Okuya, Jpn. J. Appl. Phys. **54**, 08KF03 (2015).

[131] S.-T. Zhang, M. Foldyna, H. Roussel, V. Consonni, E. Pernot, L. Schmidt-Mende, L. Rapenne, C. Jiménez, J.-L. Deschanvres, D. Muñoz-Rojas, and D. Bellet, J. Mater. Chem. C **5**, 91 (2017).

[132] J. Li, Y. Qiu, Z. Wei, Q. Lin, Q. Zhang, K. Yan, H. Chen, S. Xiao, Z. Fan, and S. Yang, Energy Environ. Sci. **7**, 3651 (2014).

[133] J. Kim, A. J. Hong, J.-W. Nah, B. Shin, F. M. Ross, and D. K. Sadana, ACS Nano **6** 265 (2012).

[134] A. P. Kryshtal, Appl. Surf. Sci. **321**, 548 (2014).

[135] S. Jeong, M. T. McDowell, and Y. Cui, ACS Nano **5**, 5800 (2011).

[136] Y. Muto, S. Nakatomi, N. Oka, Y. Iwabuchi, H. Kotsubo, and Y. Shigesato, Thin Solid Films **520**, 3746 (2012).

[137] Y. Muto, N. Oka, N. Tsukamoto, Y. Iwabuchi, H. Kotsubo, and Y. Shigesato, Thin Solid Films **520**, 1178 (2011).

[138] D. G. Schlom, L.-Q. Chen, X. Pan, A. Schmehl, and M. A. Zurbuchen, J. Am. Ceram. Soc. **91**, 2429 (2008).

[139] M. Lorenz, *Pulsed Laser Deposition, Digital Encyclopedia of Applied Physics*

Eap810, Wiley-VCH Verlag GmbH & Co. KGaA, Weinheim, 2019.

[140] T. Yamashita and P. Hayes, Appl. Surf. Sci. **254**, 2441 (2008).

[141] R. Hesse, see last access date: 2020-05-07, www.uni-leipzig.de/Bunifit/.

[142] S. Zhang and R. Xiao, J. Appl. Phys. **83**, 3842 (1998).

[143] K. Momma and F. Izumi, J. Appl. Crystallogr. **44**, 1272 (2011).

[144] H. Amano, N. Sawaki, I. Akasaki, and Y. Toyoda, Appl. Phys. Lett. **48**, 353 (1986).

[145] S. C. Su, H. Y. Zhang, L. Z. Zhao, M. He, and C. C. Ling, J. Phys. D Appl. Phys. **47**, 215102 (2014).

[146] W. Xia, H. Wang, X. Zeng, J. Han, J. Zhu, M. Zhou, and S. Wu, CrystEngComm **16**, 6841 (2014).

[147] Y. Wang, Y. Deng, L. Fan, Y. Zhao, B. Shen, D. Wu, Y. Zhou, C. Dong, M. Xing, and J. Zhang, RSC Adv. **7**, 24064 (2017).

[148] K. S. Siow, L. Britcher, S. Kumar, and H. J. Griesser, Sains Malays. **47**, 1913 (2018).

[149] H. Dixit, R. Saniz, S. Cottenier, D. Lamoen, and B. Partoens, J. Phys.: Condens. Matter **24**, 205503 (2012).

[150] T. Li, Y. Li, M. Faizan, H. Peng, and L. Zhang, Phys. Rev. B **3,** 124606 (2019).

[151] A. Walsh, D. J. Payne, R. G. Egdell, and G. W. Watson, Chem. Soc. Rev. **40**, 4455 (2011).

[152] H.-R. Liu, J.-H. Yang, H. J. Xiang, X. G. Gong, and S.-H. Wei, Appl. Phys. Lett. **102**, 112109 (2013).

[153] H. J. Kim, U. Kim, H. M. Kim, T. H. Kim, H. S. Mun, B.-G. Jeon, K. T. Hong, W.-J. Lee, C. Ju, K. H. Kim, and K. Char, Appl. Phys. Express **5**, 066102 (2012).

[154] L. Yan, H. Cao, and D. Viehland, Appl. Phys. Lett **94**, 132901 (2009).